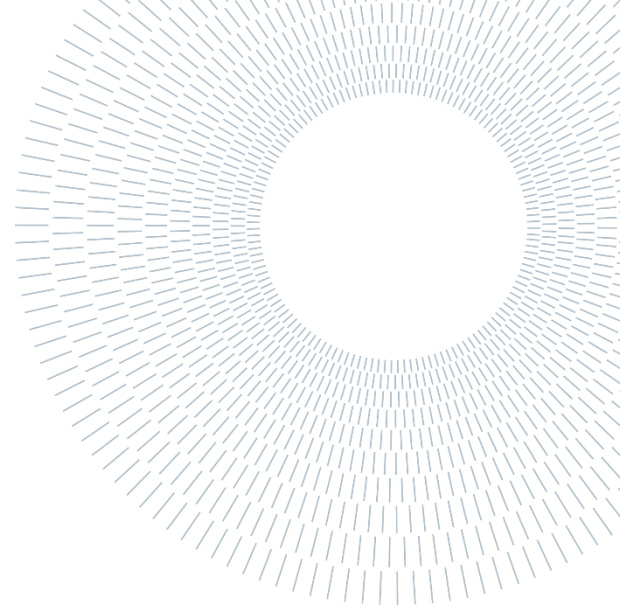




POLITECNICO
MILANO 1863

SCUOLA DI INGEGNERIA INDUSTRIALE
E DELL'INFORMAZIONE



EXECUTIVE SUMMARY OF THE THESIS

Aluminium Metal Matrix Composites reinforced with TiB_2 Particles for Laser Power Bed Fusion

MASTER OF SCIENCE DEGREE IN MATERIALS AND NANOTECHNOLOGY ENGINEERING

AUTHOR: ANDREA MISTRINI

ADVISOR: PROF. RICCARDO CASATI

CO-ADVISOR: ING. GIORGIA LUPI

ACADEMIC YEAR: 2022-2023

1. Introduction

Additive Manufacturing (AM) has exponentially grown during recent years in several industrial sectors due to its extreme versatility: it can be applied to various materials, and it allows to obtain complex shape products.

Aluminium alloys are widely used in Laser Powder Bed Fusion (LPBF) processes, since they are characterized by a low specific weight. A solution to increase mechanical properties and to reduce the hot tearing susceptibility of these types of alloys is the realization of Metal Matrix Composites (MMCs) through LPBF [1], [2].

In this work, Aluminium 2618 MMCs reinforced with micro-sized TiB_2 dispersed particles have been obtained through LPBF. TiB_2 ceramic particles were selected to avoid the formation of hot cracks and to improve the mechanical properties of the alloy. The goal of the work is to obtain powder feedstocks with high percentage of reinforcements (up to 7wt%). To reach this objective, novel methods to obtain the powder feedstocks were studied. Four different methods to create composite powder feedstocks were selected: low and high energy mechanical mixing, plasma

assisted deposition and pre-alloying by gas atomization. As a result, powders can be classified into two categories: powder particles with external or internal reinforcements.

Bulk samples have been produced through LPBF and several analyses have been performed to establish which is the feedstock that can ensure the finest grain microstructure and best material properties, like density and hardness.

2. Experimental procedure

2.1. Materials

The base material chosen for this project is Al 2618 alloy, showed in Figure 1, and with a chemical composition reported in Table 1. Al powder particles are characterised by a spherical shape and by a Particle Size Distribution (PSD) parameters D_{10} , D_{50} , and D_{90} equal to $31.6\mu m$, $52.2\mu m$ and $83.9\mu m$, respectively.

Chemical Composition (wt%)						
Element	Al	Cu	Mg	Fe	Ni	Si
	Balance	2.3	1.6	1.2	1	0.17

Table 1: Al 2618 chemical composition.

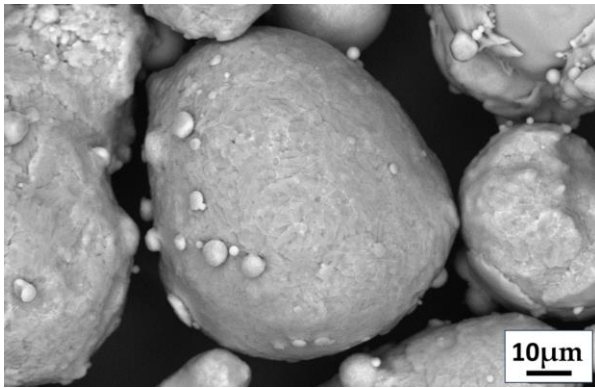


Figure 1: Scanning Electron Microscope (SEM) image of Al 2618 particles.

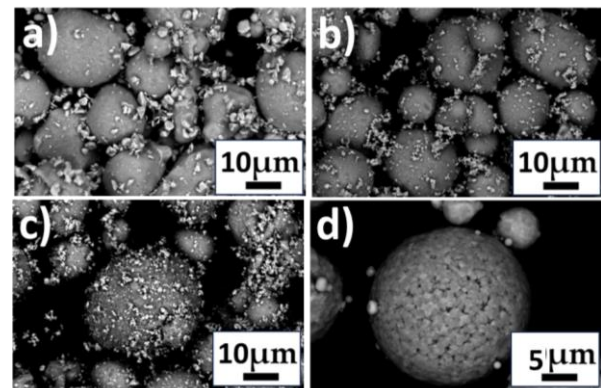


Figure 2: SEM image of low (a) and high (b) energy mixing, plasma deposition (c) and pre-alloyed (d) feedstock.

Chemical composition					
Element [wt%]	Acceptance limits	Low energy mixing	High energy mixing	Plasma deposition	Pre-alloying
Cu	1.9 – 2.7	1.96	1.76	1.7	2.1
Fe	0.9 – 1.3	0.93	1	1	1
Mg	1.3 – 1.8	1.2	1.3	1.2	1.3
Ni	0.9 – 1.2	0.93	0.99	0.9	1
B	2.0 – 2.4	1.8	1.75	2.3	0.8
Ti	5.0 – 6.0	3.8	4.04	5.3	4.1
Al		Balance			

Table 2: Acceptance limits and chemical composition of the four powder feedstocks.

2.1.1 Low energy mechanical mixing powder

The first feedstock consists of a blend of Al 2618 and TiB₂ powders mixed at 40rpm for 2 hours in a laboratory drum mixer. The process was performed under inert gas conditions (argon) and at room temperature. As a result of the mixing, the reinforcements remained attached to the surface of the Al powder particles without changing their shape and dimension. However, some reinforcements remain dispersed in the powder batch without adhering to Aluminium, as shown in Figure 2(a). The evaluation of the PSD of the mixed feedstock reports values for D10, D50, and D90 equal to 27.2 μm, 49.8 μm and 83.0 μm, respectively. Aluminium particles have a spherical shape, while borides are characterised by an irregular polygonal shape and by an average diameter of 4 μm. TiB₂ size was extrapolated from PSD curves, for all the four powder batches.

The overall chemical composition of the composite powder is reported in Table 2. The acceptance limit reported in the table consists in the target concentration of each alloying element that the powder suppliers are required to reach. The

analysis shows that all the alloying elements were within the acceptance limits except for B and Ti which were present in a lower amount than expected. As a consequence, the target amount of TiB₂ was not achieved, since just a 5.6wt% was reached.

2.1.2 High energy mechanical mixing powder

The second batch under investigation consists of a composite powder where the addition of reinforcements was achieved by high energy mechanical mixing under protective atmosphere (Nitrogen) and at room temperature. It is a dry mixing process that generate enough energy input to provide the required surface impact for the TiB₂ to adhere to the base Aluminium particles, without deforming them. From Figure 2(b), it can be noticed that reinforcements remain attached to 2618 powder thank to the collision that occur during the mixing, with the difference that the impacts in this last case are more energetic. D10, D50 and D90 values are equal to 18.5 μm, 39.8 μm and 74.4 μm, while borides are characterized by an average diameter of 2 μm.

The chemical composition is reported in Table 2. Also in this case, the target concentration of B and Ti is not satisfied. Indeed, a TiB₂ content of 5.8wt% was reached.

2.1.2 Plasma assisted deposition powder

For the production of the third feedstock powder a low-pressure plasma assisted deposition process was used.

This process consists in injecting a mixture of metal powder and ceramic in a cold plasma discharge. The energy of the plasma activates the surface of both types of particles and induce the preferential attraction between them (smallest on largest). After this treatment, the unreacted ceramic/metal particles are evacuated, while the functionalized powder is collected.

In Figure 2(c) is reported a SEM photo of the powder batch. From a visual inspection, it is possible to see a homogeneous distribution of the TiB₂ coating, characterized by smaller reinforcement particles with respect to the two powder batches obtained through low and high energy mixing. D10, D50 and D90 values are equal to 19.85 μm 39.73 μm 71.03 μm , respectively. The Al particles show a spherical shape, while the borides are characterised by an irregular morphology and an average dimension of 2 μm .

From the analysis of the chemical composition reported in Table 2 it is possible to observe that the content of Copper and Magnesium is slightly lower with respect to the acceptance limits; on the other hand, the concentration of Ti and B is compliant to the request. Indeed a 7.4wt% TiB₂ concentration was achieved, which satisfies the target composition.

2.1.4 Pre-alloyed powder

The fourth feedstock powder under investigation consists of a 2618 Al alloy modified by the addition of Ti and B, produced through gas atomization. The aim of this feedstock is to form TiB₂ reinforcing particles inside powder particles: Titanium and Boron can react giving borides, that remain dispersed within Al matrix.

Figure 2(d) reports a SEM image of a powder particle. It can be seen how it is characterized by the absence of external TiB₂ particles. For what concerns powder morphology, the values of D10, D50 and D90 are 30.3 μm , 44.8 μm , and 65.5 μm , respectively.

The chemical composition reported in Table 2 shows that the concentration of alloying elements

such as Cu, Fe, Mg, Ni, Si are within the acceptance limits defined for this project; on the contrary, both Titanium and Boron are present in an amount significantly lower than that requested.

In Figure 3 a powder particle section is reported, which shows tiny TiB₂ particles (<1 μm), indicated by the blue arrows, dispersed in the matrix. Borides content is the lowest within the four feedstocks, a 2.6wt% concentration was achieved.

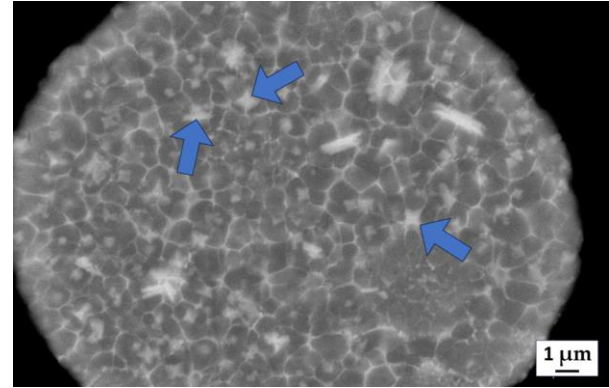


Figure 3: SEM image of a pre-alloyed powder particle section.

2.1.5 Effect of sieving on reinforcement dispersion

Sieve the residual powder from a LPBF process is fundamental in order to remove splatters and to eliminate those particles that do not satisfy anymore the dimension requirement of the printing process. However, dealing with composite powder batches, sieving can lead to the detachment of the reinforcements from the Al particles. A mechanical sieve – with a 63 μm mesh - was used to study the effect of sieving on the three feedstocks decorated with external TiB₂ (i.e., low and high energy mixing and plasma deposition). On SEM images of the three batches reported in Figure 4, analyses made with ImageJ software were performed in order to quantify the changes in the TiB₂ amount during sieving. The results are showed in Table 3.

TiB ₂ concentration [%]		
Feedstock	Before sieving	After sieving
Low energy mixing	7.6 \pm 1.0	2.7 \pm 0.1
High energy mixing	6.0 \pm 1.0	6.8 \pm 1.0
Plasma method	6.3 \pm 0.5	6.9 \pm 0.8

Table 3: TiB₂ concentration before and after sieving.

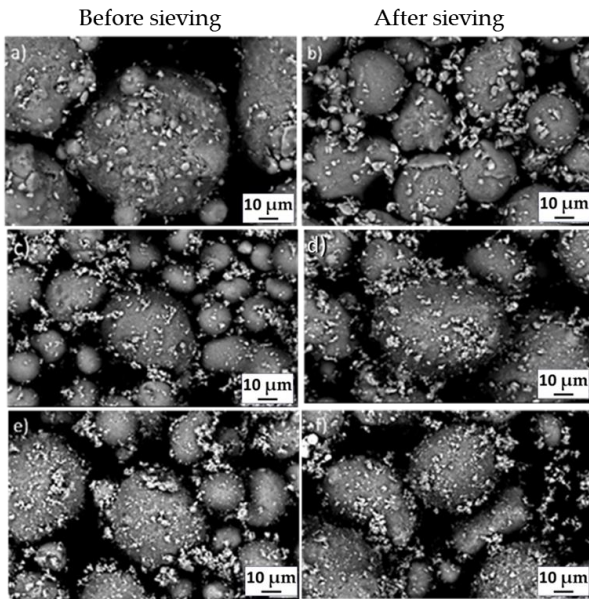


Figure 4: SEM images of low energy mixing feedstock before and after sieving (a, b), high energy mixing before and after sieving (c, d), plasma deposition before and after sieving (e, f).

Sieving process does not affect significantly the amount of reinforcements attached to the powder surface for the plasma method and the high energy mixed feedstocks, meaning that borides are well adherent to the Al powder. As a result, they can be reused without the need to re-process the powder. On the other hand, low energy mixing feedstock suffered from a strong reduction in borides content. This means that the collision between TiB_2 and Al particles are not sufficiently energetic to ensure a good adhesion. As a result, this feedstock should be re-mixed to ensure a homogeneous dispersion of the reinforcement particles after sieving.

2.1.6 Powder flowability tests

A FT4 Powder rheometer (Freeman Technology Ltd) was used to analyse the powder feedstock flowability. The FT4 employs a precision blade that is rotated and moved downwards through the powder to establish a precise flow pattern. This causes many particles to interact, or flow relative to one another, and the resistance experienced by the blade represents the difficulty of this relative particle movement.

A good powder flowability is fundamental to avoid any problems during the powder spreading phase of LPBF procedure. Three different indexes – e.g., basic flowability energy (BFE), specific energy (SE) and conditioned bulk density (CBD) – were collected. To ensure a good flowability of the

feedstock, BFE and SE indexes should be minimized, while CBD index should be the highest possible [3]. The measured values for the four feedstocks are showed in Figure 5.

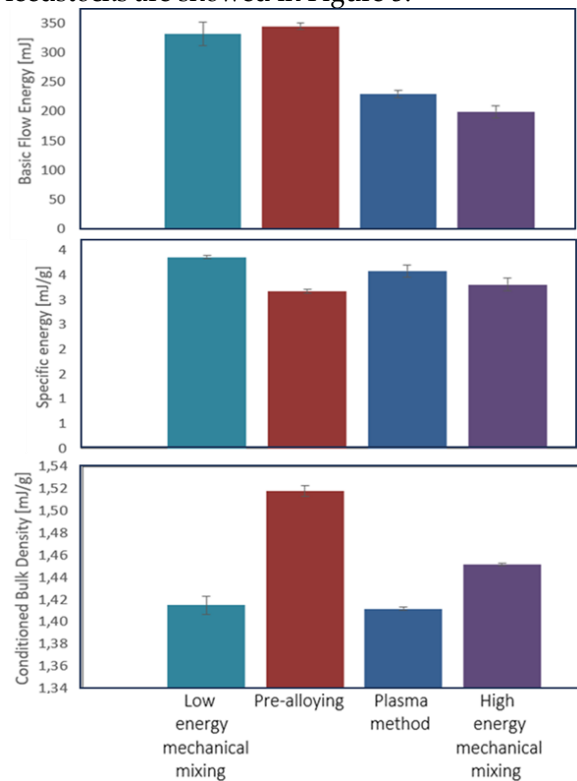


Figure 5: BFE, SE and CBD flowability indexes.

Considering SE and CBD indexes, the pre-alloyed powder appears to be the feedstock with better flow properties, immediately followed by the high energy mechanical mixed powder. However, pre-alloyed powder showed the highest BFE index, that means a poor flowability. A possible explanation is that there is an extensive flowing zone around the blade in which shearing occurs. Regarding ex-situ reinforced feedstocks, the presence of external TiB_2 particles is likely to increase the friction coefficient, generating a resisting force opposed to the sliding and shearing of adjacent particles.

To conclude, according to the results, the pre-alloyed powder had the best. Among the powder feedstocks with external TiB_2 particles, the high energy mechanical mixed one showed the best flow properties.

2.2. Bulk samples production

For each powder feedstock, $8 \times 8 \times 8$ mm³ cubic samples were printed through LPBF using the Reduced Build Volume (RBV) system of Renishaw AM250. Laser power, time of exposure and layer

thickness were kept constant at, respectively, 200W 140 μ m and 25 μ m. Different combinations of hatch distance (0.08, 0.10, and 0.12 mm) and point distance (0.06, 0.08, and 0.10 mm) have been exploited. Samples were then cut along a plane perpendicular to the printing direction. Bulk samples for metallography were prepared following common grinding and polishing procedures.

3. Result and discussion

3.1. Bulk Porosity

Porosity analyses were conducted on Light Optical Microscope (LOM) images (Figure 6) of bulk samples using the software ImageJ. Porosity levels were calculated for every printed sample and the average values are reported in Table 4. The relative density levels are always higher than 99%.

Feedstock	Average porosity [%]
Low energy mixing	0.55 \pm 0.15
High energy mixing	0.39 \pm 0.10
Plasma deposition	0.40 \pm 0.14
Pre-alloying	0.55 \pm 0.14

Table 4: Bulk samples average porosity.

The presence of the reinforcement particles successfully avoided the formation of hot cracks, which instead are generally present in LPBF printed standard Al 2618 alloy [4]. Solidification cracks are mainly formed during final stages of solidification, when the thermal shrinkage promotes the build-up of tensile stresses in the semi-solid alloy. As the alloy tensile strength is overcome, the nucleation and consequent propagation of cracks along grain boundaries occur. However, TiB₂ present in the melt pools acted as heterogeneous nucleation sites for α -Al grains. The resulting fine equiaxed grain structures were able to accommodate higher shrinkage stresses and to prevent crack formation [5].

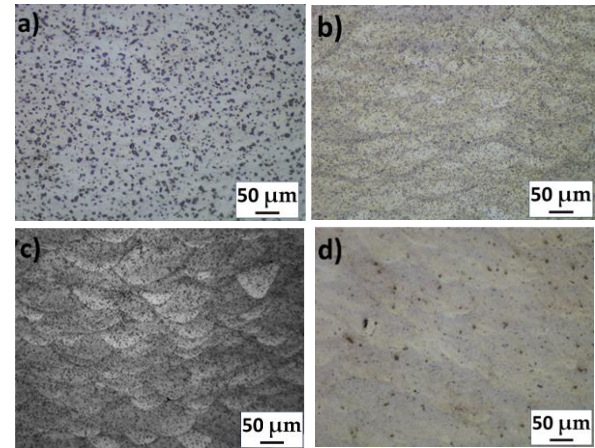


Figure 6: LOM images of low and high energy mixing (a, b), plasma deposition (c) and pre-alloyed (d) bulk samples.

3.2. TiB₂ distribution

A homogeneous reinforcements distribution in the bulk material is essential to obtain a final product with high and isotropic mechanical properties. In order to verify the spatial dispersion of borides and their quantity, analyses have been performed on bulk sample SEM images (Figure 7). In Table 5 information regarding TiB₂ percentage in bulk samples and their average dimensions are reported.

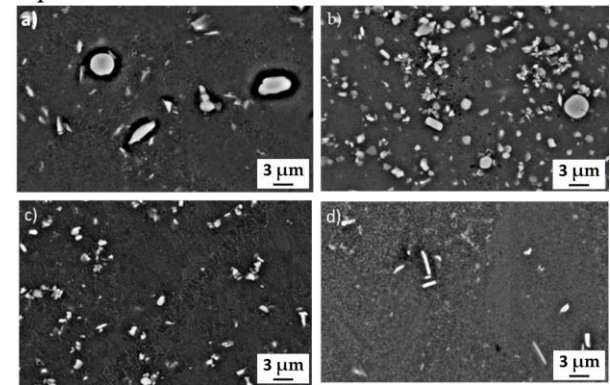


Figure 7: SEM images of bulk samples: low energy mixing (a); high energy mixing (b); plasma deposition (c); pre-alloying (d).

Feedstock	TiB ₂ percentage [%]	TiB ₂ average dimension [μ m]
Low energy mixing	7.1 \pm 0.9	1.8 \pm 0.3
High energy mixing	6.8 \pm 0.8	1.0 \pm 0.1
Plasma deposition	5.9 \pm 0.4	0.8 \pm 0.02
Pre-alloying	0.87 \pm 0.17	0.36 \pm 0.3

Table 5: TiB₂ percentage and average dimensions in bulk samples.

Reinforcing particles are homogeneously dispersed within the metal matrix and their diameter and content are reduced moving from the first to the last feedstock (see Table 5). However, these values are measured when the samples are cut along a plane perpendicular to the scanning direction. As a result, the effective measures reported are an evaluation of the borides section, not the of whole particle. The same is valid also for the TiB_2 percentage, which is not a volume or weight concentration, but an evaluation of borides content on the section surface.

According to Table 5, the highest TiB_2 content was achieved by the two mixing strategies, followed by the plasma deposition. For what concerns the pre-alloyed powder, reinforcements particles are present in a lower quantity since Ti and B target compositions were not achieved. Moreover, borides are so small that they cannot be detected also at the highest magnification achievable by the Scanning Electron Microscope. However, Sub-micrometric reinforcements are beneficial since they provide better strengthening effect than bigger particles [6].

3.3. Grain morphology

Electron Backscatter Diffraction maps (EBSD) have been used to study the grains of the bulk samples, in particular their size and orientation. In Figure 8 are reported the Inverse Polar Figure (IPF) of the bulk samples obtained from the four powder feedstocks.

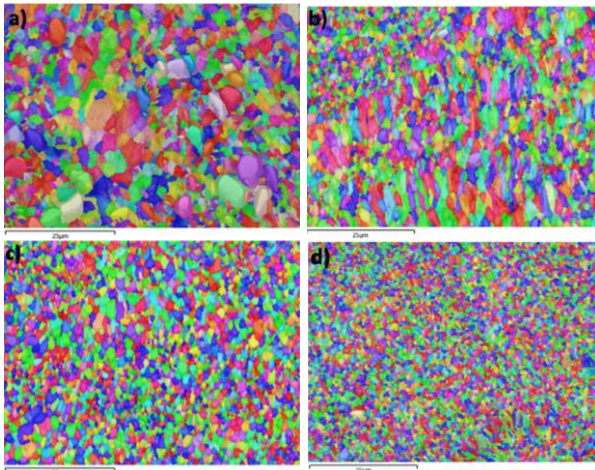


Figure 8: Bulk samples IPF maps: low (a) and high (b) mechanical mixing, plasma deposition (c) and pre-alloying (d).

In Table 6, are showed the average diameters and areas of the grains.

Feedstock	Average grain area [μm^2]	Average grain diameter [μm]
Low energy mixing	2.3	1.5
High energy mixing	1.6	1.3
Plasma deposition	1.1	1.1
Pre-alloying	0.6	0.8

Table 6: Grain average areas and diameters in bulk samples.

From Figure 8, it is possible to appreciate the grain refinement thanks to the presence of TiB_2 particles. Furthermore, a reduction in grain size moving from low energy mixing to pre-alloyed case was observed. TiB_2 particles act as heterogeneous nucleation sites for the primary α -Al phase, leading to a fine equiaxed grain structure [5]. The grains of plasma deposition bulk sample are smaller than low and high energy mixing ones, since the reinforcements size is smaller, although the borides concentration is quite similar (see Table 5). This means that there are more heterogeneous nucleation sites for α -Al phase and, as a result, a finer grain structure is obtained. The finest grain structure was found in the sample obtained from pre-alloyed powder even if this the feedstock was characterized by the lowest amount of TiB_2 . Indeed, this type of powder is pre-alloyed with an excess of Titanium, which has a double function: the first one is to react with Boron to form TiB_2 particles, the second is to enhance the formation of Al_3Ti intermetallic. This latter compound has the ability to refine α -Aluminium grain, since during the solidification of the alloy Al_3Ti particles are formed and they act as heterogeneous nucleation sites for new grains [5]. Consequently, the alloy grains resulted further refined.

3.4. Hardness

Hardness tests have been performed on all the bulk samples. The average values for each feedstock are schematized in Table 7.

Feedstock	Average hardness [HV]
Low energy mixing	137 ± 4
High energy mixing	128 ± 5
Plasma deposition	123 ± 4
Pre-alloying	157 ± 4

Table 7: Bulk samples average hardness.

The presence of TiB₂ reinforcements played a fundamental role in enhancing the mechanical properties of the composite material. Indeed, all the average hardness values reported in Table 7 are higher if compared to the hardness (104.0 HV) of standard Al 2618 as-build samples obtained by Casati et. al [7].

The pre-alloyed powder showed the highest hardness values. In this case the borides particles dimension was much smaller if compared to the other three powders and the lowest grain dimension was found in these samples. As a result, the strengthening effect given by in-situ sub-micrometric TiB₂ was more effective, leading to higher material hardness [6].

4. Conclusions

In this work, composite Al 2618-TiB₂ feedstocks with a high fraction of reinforcement (6-7wt%) were successfully produced by low energy mixing, high energy mixing and plasma assisted deposition. For the pre-alloyed batch, instead, a maximum of ~3wt% of TiB₂ was obtained. The composition of the externally reinforced feedstocks can be easily modified by adding further borides in the drum mixer. For what concerns the pre-alloyed feedstock, according to the supplying company, it is not possible to increase the TiB₂ content since the maximum B concentration was already achieved during the gas atomization process.

Powder flowability was studied. Analyses revealed that the addition of ex-situ ceramic particles can have a detrimental effect on flowability. For this reason, the pre-alloyed feedstock showed the overall best flowability. Instead, among the ex-situ reinforced feedstocks, the high energy mixed powder is characterized by the best flowing behaviour.

Bulk samples were produced by LPBF processes to investigate how the choice of the starting powder could affect the microstructure and the mechanical properties of the bulk products. High levels of relative density (>99%) were achieved with all the powder batches. Moreover, the ceramic compounds were able to refine the microstructure and avoid cracks formation. As a result, the hot cracking susceptibility and low processability of the standard Al 2618 alloy was overcome. Reinforcement particles present in MMC bulk samples were able to increase the hardness with respect to standard Al 2618 alloy. The highest bulk hardness was achieved with pre-alloyed powder,

since it showed the finest grain structure and TiB₂ dimension, though it contains the lowest amount of TiB₂. This occurred due to the small size of reinforcement particles and to the refined grain structure.

A possible solution to overcome the limitations in TiB₂ quantity of pre-alloying by gas atomization is to combine different powder functionalization methods. In this scenario, the surface of pre-alloyed powder can be decorated with ceramic particles with one of the ex-situ methods proposed in this work.

References

- [1] J. H. Martin, B. D. Yahata, J. M. Hundley, J. A. Mayer, T. A. Schaedler, and T. M. Pollock, "3D printing of high-strength aluminium alloys," *Nature*, vol. 549, no. 7672, pp. 365–369, Sep. 2017, doi: 10.1038/nature23894.
- [2] R. Nandhakumar and K. Venkatesan, "A process parameters review on selective laser melting-based additive manufacturing of single and multi-material: Microstructure, physical properties, tribological, and surface roughness," *Mater Today Commun*, vol. 35, p. 105538, Jun. 2023, doi: 10.1016/j.mtcomm.2023.105538.
- [3] R. Freeman, "Measuring the flow properties of consolidated, conditioned and aerated powders – A comparative study using a powder rheometer and a rotational shear cell," *Powder Technol*, vol. 174, no. 1–2, pp. 25–33, May 2007, doi: 10.1016/j.POWTEC.2006.10.016.
- [4] D. Koutny *et al.*, "Influence of Scanning Strategies on Processing of Aluminum Alloy EN AW 2618 Using Selective Laser Melting," *Materials*, vol. 11, no. 2, p. 298, Feb. 2018, doi: 10.3390/ma11020298.
- [5] F. Belevi, R. Casati, F. Larini, M. Riccio, and M. Vedani, "Investigation on two Ti–B-reinforced Al alloys for Laser Powder Bed Fusion," *Materials Science and Engineering: A*, vol. 808, p. 140944, Mar. 2021, doi: 10.1016/j.msea.2021.140944.
- [6] R. Casati and M. Vedani, "Metal Matrix Composites Reinforced by Nano-Particles—A Review," *Metals (Basel)*, vol. 4, no. 1, pp. 65–83, Mar. 2014, doi: 10.3390/met4010065.
- [7] R. Casati, J. N. Lemke, A. Z. Alarcon, and M. Vedani, "Aging Behavior of High-Strength Al Alloy 2618 Produced by Selective Laser Melting," *Metallurgical and Materials Transactions A*, vol. 48, no. 2, pp. 575–579, Feb. 2017, doi: 10.1007/s11661-016-3883-y.



POLITECNICO
MILANO 1863

SCUOLA DI INGEGNERIA INDUSTRIALE
E DELL'INFORMAZIONE

ALUMINIUM METAL MATRIX COMPOSITES REINFORCED WITH TiB_2 PARTICLES FOR LASER POWDER BED FUSION

MASTER OF SCIENCE DEGREE IN
MATERIALS AND NANOTECHNOLOGY ENGINEERING

Author: **ANDREA MISTRINI**

Student ID: 10628466

Advisor: Prof. Riccardo Casati

Co-advisor: Ing. Giorgia Lupi

Academic Year: 2022-23

Abstract

Additive Manufacturing (AM) has exponentially grown during recent years in several industrial sectors, including aerospace, automotive and electronics, due to its extreme versatility: it can be applied to various materials like metals, polymers and ceramics and it allows to obtain complex shape products, which cannot be manufactured through conventional methods.

Aluminium alloys are widely used in AM with techniques such as Laser Powder Bed Fusion (LPBF) since they are characterized by a low specific weight. A solution to increase mechanical properties and to reduce the hot tearing susceptibility of these types of alloys is the realization of Metal Matrix Composites (MMCs) through LPBF.

In this work, Aluminium 2618 MMCs reinforced with micro-sized TiB₂ dispersed particles have been obtained through LPBF. TiB₂ ceramic particles were selected to avoid the formation of hot cracks and to improve the mechanical properties of the alloy. The goal of the work is to obtain powder feedstocks with high percentage of reinforcements (up to 7 wt%). To reach this objective, novel methods to obtain the powder feedstocks were studied. Four different methods to create composite powder feedstocks were selected: low and high energy mechanical mixing, plasma assisted deposition and pre-alloying by gas atomization. As a result, powders can be classified into two categories: powder particles with external or internal reinforcements. The functionalization of the powder feedstocks allowed to reach the goal of 7wt% of reinforcement particles with all the powder feedstocks, except for the pre-alloyed where a maximum of ~3wt% was obtained.

The pre-alloyed powder showed the highest flowability since it is not affected by external TiB₂ attached to Al micro-sized particles, that hinder the powder flow. Pre-alloyed, high energy mechanical mixing and plasma assisted powders are also not altered by sieving (necessary operation to perform to reuse the powder feedstock before a further printing process). Low energy mechanical mixing feedstock, instead, showed a crucial borides reinforcements reduction after sieving and for this reason it must be re-mixed before being reused.

Cubic bulk samples were produced by pulsed laser LPBF varying hatch distance and point distance values, in order to achieve high material density. Bulk densities higher than 99% were obtained. The ceramic compounds were able to refine the microstructure and avoid cracks formation. The type of feedstock and the dimension

of TiB₂ particles strongly affects the microhardness of the bulk material and the size, orientation and distribution of the grains. Specifically, the pre-alloyed powder showed the best results regarding hardness ($\sim 157 \pm 4$ HV) and the lowest average grain diameter (0.8 μm).

Keywords: Additive Manufacturing (AM), Powder Laser Bed Fusion (LPBF), Metal Matrix Composites (MMCs), Aluminium alloys, TiB₂.

Abstract in italiano

La manifattura additiva (AM) è cresciuta esponenzialmente negli ultimi anni in diversi settori industriali, tra cui l'aerospaziale, l'automobilistico e l'elettronica. Grazie alla sua estrema versatilità può essere applicata a diversi materiali come metalli, polimeri e ceramici e consente di ottenere prodotti di forma complessa, che non potrebbero essere fabbricati con metodi convenzionali.

Le leghe di alluminio sono ampiamente utilizzate nell'AM con tecniche come la fusione laser a letto di polvere (LPBF), poiché sono caratterizzate da un basso peso specifico. Una soluzione per incrementare le proprietà meccaniche di queste leghe e ridurre la loro suscettibilità alla formazione di cricche a caldo è la realizzazione di materiali compositi a matrice metallica (MMC) mediante LPBF.

Nello specifico, in questo lavoro, tramite LPBF, sono stati ottenuti compositi in lega di alluminio 2618 rinforzati con una dispersione di microparticelle di TiB_2 . La scelta è ricaduta sulle particelle di ceramico in modo tale da evitare la formazione di cricche a caldo e da stabilizzare le proprietà meccaniche della lega ad alte temperature. L'obiettivo di questo progetto è di ottenere polveri composite ad alte concentrazioni di rinforzi – fino al 7% in peso – rispetto alla matrice metallica. In particolare, quattro diversi metodi di produzione di polveri composite sono stati studiati: miscelazione meccanica a bassa e ad alta, deposizione al plasma e pre-alligazione tramite atomizzazione a gas. Le polveri possono quindi essere distinte in due differenti categorie: polveri rafforzate da particelle interne oppure esterne. La funzionalizzazione delle polveri ha permesso di ottenere il 7% in peso di rinforzi con tutti i metodi eccetto per la polvere pre-alligata, con cui solo il 3% in peso è stato raggiunto.

La polvere ottenuta per pre-alligazione è caratterizzata da una migliore fluidità, a causa dell'assenza di particelle di rinforzo esterne che ne limitano lo scorrimento. Inoltre, la polvere pre-alligata e quelle ottenute tramite miscelazione ad alta energia e deposizione assistita da plasma non vengono alterate dalla setacciatura (operazione necessaria per pulire la polvere residua prima di un ulteriore processo di stampa. Quella ottenuta tramite miscelazione meccanica a bassa energia, invece, mostra una netta riduzione nel numero di rinforzi a valle della setacciatura, e per questo un'ulteriore miscelazione è necessaria.

Campioni cubici sono stati prodotti variando la hatch distance e la point distance durante la fase di stampa, in modo tale da poter ottenere la densità più alta possibile. Sono stati ottenuti campioni con densità maggiori del 99%. I rinforzi ceramici sono stati in grado di affinare la microstruttura dei grani ed evitare la formazione di cricche. La tipologia di polvere e la dimensione delle particelle dei boruri influenzano la durezza del composito e la dimensione, orientamento e distribuzione dei grani cristallini. In particolare, la polvere ottenuta per pre-alligazione ha mostrato il miglior risultato per quanto riguarda la durezza ($\sim 157 \pm 4$ HV) e il diametro medio dei grani ($0,8 \mu\text{m}$).

Parole chiave: Manifattura additiva (AM), Fusione laser a letto di polvere (LPBF), Compositi a matrice metallica (MMCs), Leghe di alluminio, TiB_2 .

Contents

Abstract	i
Abstract in italiano	iii
Contents	v
1 State of the art	1
1.1. Metal matrix composites	1
1.1.1. Strengthening mechanisms	2
1.1.2. Yield strength prediction models	5
1.1.3. Effect of strengthening contributions	7
1.2. LPBF	9
1.2.1. LPBF parameters.....	11
1.2.2. Effect of parameters on material properties	13
1.2.3. Powder	18
1.2.4. Defects in LPBF products	21
2 Aim of the thesis	25
3 Materials and methods	26
3.1. Materials	26
3.1.1. Low energy mechanical mixing powder.....	26
3.1.2. High energy mechanical mixing powder	27
3.1.3. Plasma assisted deposition powder.....	27
3.1.4. Pre-alloyed powder	28
3.2. Process and characterization equipment	28
3.2.1. LPBF sample production	28
3.2.2. Optical microscope and ImageJ.....	30
3.2.3. SEM.....	31
3.2.4. XRD.....	31
3.2.5. Microhardness tests.....	31
3.2.6. Mechanical mixer.....	32
3.2.7. Sieve.....	32
3.2.8. Powder rheometer	32
3.2.9. Particle Size Analyser.....	33
3.3. Metallographic preparation.....	33
4 Results	34
4.1. Powder analysis.....	34

4.1.1.	SEM and Chemical analyses	34
4.1.2.	Effect of sieving on particles dispersion.....	47
4.1.3.	Powder flowability tests	54
4.2.	Bulk analysis	56
4.2.1.	Porosity	57
4.2.2.	TiB ₂ distribution in bulk samples	60
4.2.3.	Grain morphology	66
4.2.4.	Bulk hardness	72
5	Conclusions	75
	Bibliography	77
	List of Figures	83
	List if Tables	85

1 State of the art

1.1. Metal matrix composites

Metal matrix composites (MMCs) consist of a metal matrix reinforced with nano or micro particles, characterized by mechanical properties different from those of the matrix. The reinforcements can be particles, whiskers and continuous or discontinuous fibres. Particle-reinforced composites are preferable on the fibre-reinforced composites due to their low cost and automatic processing. Thanks to the particle dispersion it is possible to enhance yield strength, ultimate tensile strength, hardness and Young modulus of the unreinforced metal [1]–[3].

Aluminium matrix composites (AMCs) have been receiving considerable attention as promising materials for various applications due to their excellent physical and mechanical properties. The incorporation of reinforcement material into the aluminium matrix composite (AMC) results in enhanced mechanical properties such as increased strength, stiffness, and wear resistance [4]. Meanwhile, the aluminium matrix itself exhibits favourable characteristics for machining and welding processes. AMCs can be tailored to meet the specific requirements of a particular application by varying the type, size, and volume fraction of the reinforcement material.

The reinforcements employed in advanced AMCs can be classified into three primary categories, namely ceramic, metallic, and organic. Ceramic reinforcements are favoured owing to their elevated strength, stiffness, and thermal stability [4]–[6]. Additionally, they exhibit resistance to both corrosion and wear. Silicon carbide (SiC), aluminium oxide (Al_2O_3), and boron carbide (B_4C) are among the frequently employed ceramic reinforcements in the fabrication of advanced metal matrix composites. Ceramic reinforcements are frequently utilised in scenarios that require elevated levels of strength and stiffness, such as in aerospace and automotive applications. Structural applications often necessitate the utilisation of metallic reinforcements due to their desirable machinability and weldability properties. Organic reinforcements are frequently employed in scenarios that require toughness and impact resistance, such as marine applications and sporting goods [7], [8].

To further develop new MMC materials, strengthening mechanisms must be understood and constitutive relationships must be developed, in order to predict the

mechanical properties of the composites as a function of particles size, shape and volume fraction.

1.1.1. Strengthening mechanisms

Matrix mechanical properties can be enhanced thanks to several particle strengthening mechanism such as load transfer effect, Hall-Petch strengthening, Orowan strengthening, Coefficient of Thermal Expansion (CTE) and Elastic Modulus (EM) mismatch.

Load transfer strengthening mechanism

The hard particles, characterized by a higher stiffness than the metal matrix, are able to bear a major portion of the load applied thanks to the mechanism of interfacial shear load transfer. This reveals the existence of strong bonding at particle-matrix interface, which improves the composite material resistance to externally applied loads [1], [9].

A modified Shear Lag model, shown in Equation 1 and proposed by Nardone and Prewo [1], is commonly used to predict this type of strengthening contribution.

$$\Delta\sigma_{LT} = V_p \sigma_m \left[\frac{(l+t)A}{4l} \right] \quad \text{Equation 1}$$

Where V_p is the volume fraction of the particles in the MMC, σ_m is the yield strength of the unreinforced matrix, l and t are, respectively, the size of the particle parallel and perpendicular to the loading direction and A is the particles section area. In case of equiaxed particles, the Equation 1 is reduced to Equation 2:

$$\Delta\sigma_{LT} = \frac{1}{2} V_p \sigma_m \quad \text{Equation 2}$$

Hall-Petch strengthening

The grain size plays a fundamental role on metal strength since the presence of the grain boundaries can hinder dislocation movement. This phenomenon is due to the different orientation of adjacent grains and the high atomic disorder that characterize these particular surfaces, that distort the slip plane, increasing the resolved shear stress needed to obtain dislocation glide. As a result, decreasing the grain size, more grain boundary surfaces are introduced and the yield strength of the material is increased, according to the Hall-Petch model [1], [9], [10], shown in Equation 3:

$$\Delta\sigma_{HP} = \frac{k_y}{\sqrt{d}} \quad \text{Equation 3}$$

Where K_y is a strengthening coefficient (different for each material) and d is the average grain diameter. The introduction of strengthening particles in the metal matrix

is able to decrease the grain growth susceptibility since they act as pinning point hindering the grain boundaries migration.

Tuning the particle concentration and average size, we can modify the diameter of the grains, according to Zener model [1], as shown in Equation 4:

$$d_{grain} = \frac{4\alpha d_p}{3V_p} \quad \text{Equation 4}$$

Where α is a proportional constant, d_p is the particle diameter and V_p is the particle volume fraction. By introducing into the original metal matrix a very dense dispersion of fine particles it is possible to obtain a finer grain structure with higher mechanical properties. It can be understood that the Equation 4 cannot be applied when the volume fraction or size of reinforcing particles approaches zero, and therefore it has some limitations.

Orowan strengthening

Presence of fine secondary phase particles in the microstructure affects this dislocation movement induced by plastic deformation. In MMNCs reinforced with fine particles, when the strengthening phase is encountered by a moving dislocation, the particles restrict the movement by pinning the dislocations around them [1], [9]–[12]. The dislocations first bend (Orowan bowing) and then form a dislocation loop around the particles (Orowan looping), as shown in Figure 1.

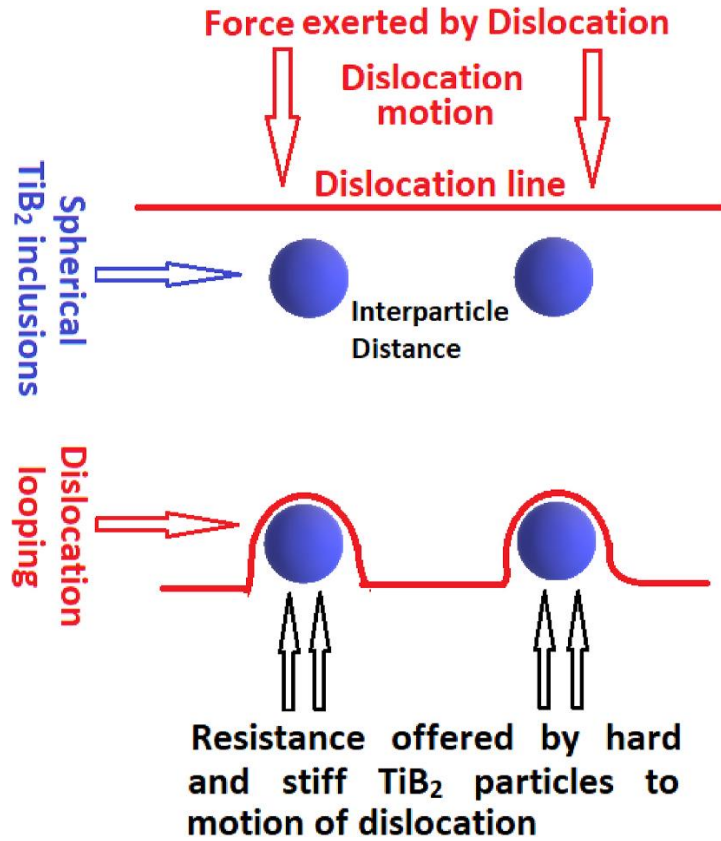


Figure 1: Orowan loop formation around TiB₂ particles [9]

This phenomenon increases the stress needed to further dislocation movement and, as a result, the dislocation propagation is reduced and the mechanical properties enhanced. The increase regarding the stress is described Equation 5 [1]:

$$\Delta\sigma_{OR} = \frac{0.13Gb}{d_p \left(\sqrt[3]{\frac{1}{2}V_p} - 1 \right)} \ln \frac{d_p}{2b} \quad \text{Equation 5}$$

Where b is the dislocation Burger vector and G is the shear elastic modulus.

It is widely acknowledged, however, that Orowan strengthening is not significant in the micro sized particulate-reinforced MMCs, because the reinforcement particles are coarse and the interparticle spacing is large.

CTE and EM mismatch

When MMCs are cooled from high temperature or when are heated, different values of coefficient of thermal expansion (CTE) and elastic modulus (EM) between the particles and the matrix can induce thermal misfit strains. These thermal misfits induce a stress state in the material, leading to the formation of geometrical necessary

dislocations (GNDs) at the particle-matrix interface [1], [9], [10]. As a result, the matrix undergoes strain hardening and its strength is enhanced.

GNDs density due to CTE and EM mismatch can be evaluated according to Equation 6 and Equation 7 [1]:

$$\rho^{CTE} = \frac{A\Delta\alpha\Delta T V_p}{bd_p(1-V_p)} \quad \text{Equation 6}$$

$$\rho^{EM} = \frac{6V_p}{\pi d_p^3} \epsilon \quad \text{Equation 7}$$

Where A is a geometric constant, $\Delta\alpha$ is the difference between the CTE of matrix and particles, ΔT the temperature gradient of the cooling or heating process, b is the dislocation Burger vector.

The general equation (Equation 8) to describe the effect of both the two mismatches is the Taylor relationship [1], [10]:

$$\Delta\alpha_{CTE+EM} = \sqrt{3}\beta Gb(\rho^{CTE} + \rho^{EM}) \quad \text{Equation 8}$$

Where β is a constant and G is the shear elastic modulus of the unreinforced matrix. From these relationships, it can be understood that increasing the CTE mismatch, more dislocations are introduced, the matrix results strain hardened and therefore the mechanical strength is enhanced.

1.1.2. Yield strength prediction models

Different analytical models are present in literature to predict the final mechanical strength of the MMC materials. Various models based on continuum mechanics and micromechanics approaches are available and some of them are summarized in the following section.

For each strengthening mechanism can be associated an improvement factor. This factor expresses how relevant is the mechanism involved on the final mechanical strength of the material. All the different improvement factors are listed in the following relationships (from Equation 9 to Equation 12) [9]:

$$f_{LT} = \frac{1}{2} V_p \quad \text{Equation 9}$$

$$f_{HP} = \frac{\Delta\sigma_{HP}}{\sigma_{y,m}} \quad \text{Equation 10}$$

$$f_{OR} = \frac{\Delta\sigma_{OR}}{\sigma_{y,m}} \quad \text{Equation 11}$$

$$f_{CTE+EM} = \frac{\Delta\sigma_{CTE+EM}}{\sigma_{y,m}} \quad \text{Equation 12}$$

Where $\sigma_{y,m}$ is the yielding strength of the unreinforced matrix.

Sum of contributions

The simplest approach consists in the summation of all the contributions given by the strengthening mechanism [1], [9], as illustrated in Equation 13.

$$\sigma_{c,y} = \sigma_{m,y} + \Delta\sigma_{LT} + \Delta\sigma_{HP} + \Delta\sigma_{OR} + \Delta\sigma_{CTE+EM} \quad \text{Equation 13}$$

Where $\sigma_{c,y}$ is the final yielding strength of the MMC. The main issue related to this approach is that it does not consider interaction among the mechanisms and it assumes all the mechanisms as independent to each other.

Modified Clyne model

In the modified Clyne model [1], [9], contributions of the different mechanisms are added by the root sum square method, as illustrated in the Equation 14:

$$\sigma_{c,y} = \sigma_{m,y} + \sqrt{\Delta\sigma_{LT}^2 + \Delta\sigma_{HP}^2 + \Delta\sigma_{OR}^2 + \Delta\sigma_{CTE+EM}^2} \quad \text{Equation 14}$$

Ramakrishnan model

In this model both additive and synergic effect of load transfer and enhanced dislocation density mechanism due to CTE and EM mismatch are considered. Mechanisms are, from this moment, no more considered as independent. Ramakrishnan approach [9] is described by Equation 15:

$$\sigma_{c,y} = \sigma_{m,y}(1 + f_{LT})(1 + f_{CTE+EM}) \quad \text{Equation 15}$$

Modified shear lag model

Zhang and Chen [9] modified the initial shear lag model proposed by Nardone and Prewo [1] utilizing the Ramakrishnan approach and adding also the Orowan strengthening contribution. The final model is described by the following Equation 16:

$$\sigma_{c,y} = \sigma_{m,y}(1 + f_{LT})(1 + f_{CTE+EM})(1 + f_{OR}) \quad \text{Equation 16}$$

However, this model does not consider the effect of reinforcements on matrix grain size. This effect of increased grain density will significantly contribute to the strengthening of the composite through direct strengthening of matrix material.

Mirza and Chen model

Mirza and Chen modified the previous model by introducing the beneficial effects given by the grain refinement and the adverse effects given by the presence of a certain

level of porosity in the material [9]. The new relations are shown in the following equations:

$$\sigma_{c,y} = \sigma_{m,y}(1 + f_{LT(p)})(1 + f_{CTE+EM})(1 + f_{OR})(1 + f_{HP})(1 - f_p) \quad \text{Equation 17}$$

$$f_{LT(p)} = \frac{1}{2}V_p - P \quad \text{Equation 18}$$

$$f_p = 1 - e^{-nP} \quad \text{Equation 19}$$

Where $f_{LT(p)}$ is the improvement factor associated to load transfer in presence of a certain porosity percentage (P), f_p is the deterioration factor associated to the porosity and n is an empirical constant.

Sahoo et al. model

The model proposed by the authors of the article [9] and shown in Equation 20 takes into account all the possible strengthening mechanisms depicted above and also the detrimental effect of porosity:

$$\sigma_{c,y} = \sigma_{m,y}(1 + f_{LT(p)})(1 + f_{CTE+EM})(1 + f_{OR})(1 - f_p) + \Delta\sigma_{HP} \quad \text{Equation 20}$$

1.1.3. Effect of strengthening contributions

In literature there are several explanations regarding how single strengthening mechanism has different effect on the matrix mechanical properties depending on different parameter, like the particle size and volume fraction.

As showed in Figure 2, in a metal matrix nano-composite (MMNC) material, the contribution of each different strengthening mechanism is heavily dependent on the particle size.

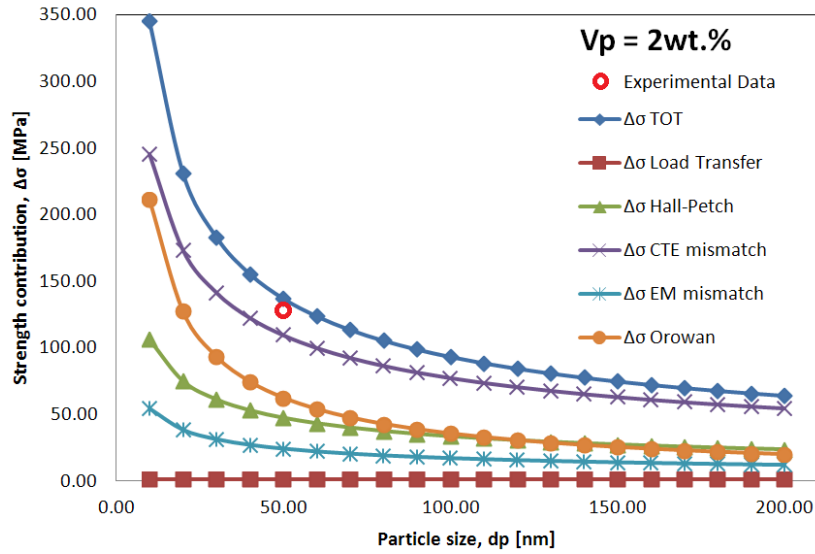


Figure 2: Effect of strengthening contributions and total resulting strengthening increment for a 2 wt.% Al_2O_3 reinforced Al matrix composite, calculated using the modified Clyne model [1].

In particular, the most important contribution is given by the CTE mismatch and the Orowan effect, especially when the particle size is lower than 50nm [1]. In that precise case, it is also clear how the load bearing effect is practically negligible compared to other mechanisms, since the particles are too small.

On the other hand, considering MMC, the particle dimension is in the range of μm and as a result the Orowan strengthening effect become negligible, since the interparticle distance increases affecting the particle capability to distort and block the dislocation line while moving [11], [12]. This remarkable difference in strengthening effectiveness is clearly showed in the following Figure 3.

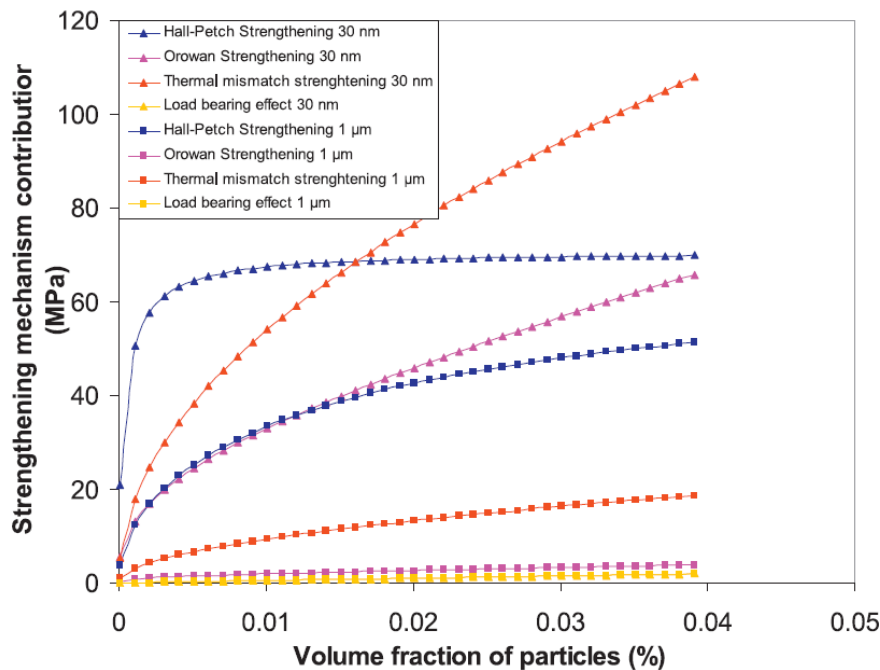


Figure 3: Strengthening mechanism contributions as a function of volume fraction for the particle sizes 30 nm and 1 μm [10].

Figure 3 shows a graph of strengthening mechanism contribution as a function of volume fraction for two different particle sizes on the nanometer and micrometer scale. For the nanometer size, the strengthening mechanism contributions are more significant than those with the micrometer particle size [10]. This is even more evident for Orowan strengthening, as the values calculated for a 1 μm particle size are near the load-bearing effect values and can be neglected. It is noteworthy that the effect of Hall–Petch is still significant even for microscale particle size. In the case of MMC indeed grain refinement is the most effective mechanism, it depends more on the volume fraction of the particles and is less sensitive to particle size [10].

1.2. LPBF

A wide range of MMCs have been successfully produced and are now employed in a large range of traditional and new engineering applications. However, MMCs suffer from drawbacks in terms of low machinability, formability, and weldability. Moreover, there are still problems in process control to achieve uniform distribution of particles, or poor machinability [13], [14]. Additive Manufacturing can be considered as a suitable tool to overcome these issues. Indeed, AM processes allow producing near-net shape parts, thus significantly reducing the post-processing

operations. Taking advantage of a layer-by-layer deposition strategy, AM processes open new opportunities to produce parts with unprecedented complex shape, even including lattice or topologically optimized structures. Thus, the combination of lightweight structures with high specific strength MMCs can open new scenarios for the design of parts and structures for aerospace applications with enhanced performance.

AM is a technology initially originated by Charles Hull in 1986 from stereolithography (SLA) to produce prototype parts [14]. AM technology was subsequently expanded, Selective Laser Sintering (SLS) was introduced by Carl Deckard, Fusion Deposition Modelling (FDM) by Scott crump in 1989, Laminated Object Manufacturing (LOM) by Michael Feygin in 1991, Binder Jet by Emanuel Sachs in 1993, Selective laser melting (SLM) by Fraunhofer Institute, Germany, in 1995 and 4D printing by Skylar Tibbits in 2014 [14]. AM process received the input from the Computer-Aided Design (CAD) geometric model to create 3-Dimensional components by fusing the material layer after layer using a heat source (e.g. laser, electron beam or electric arc) and feedstock (e.g. metal powder or wire). The so-called layer-by-layer additive manufacturing is opposed to the subtractive process as it involves the removal of material to produce final components. AM is applied to produce components that are impossible to produce through conventional manufacturing methods [14], [15]. It is widely applied to fabricate complex shape components due to less material wastage, time, and cost from design to the production cycle. It is applied to various materials, including biochemical, polymers, ceramics, metals, composites, and biodegradable materials, to various manufacturing fields, including aerospace, automotive, biomedical, architecture, electronics and the medical sector. The basic steps involved in all AM techniques are the following: firstly, the creation of 3D CAD model data that is transferred to the machine, prototype building, post-processing and inspection of the final 3D product [14], [16].

Among AM processes, Laser Powder Bed Fusion (LPBF) is the most concrete AM technique to manufacture parts by consolidating powder particles using a laser beam [15]. LPBF is so widely studied because not only complicated geometries and dense parts with a high precision can be fabricated by this technique, but also components with finer grains can be acquired because of an extremely high cooling rate (more or less 105°C/s) [15], [17].

The schematic diagram of the LPBF process is shown in Figure 4. Regarding the LPBF technique, the position of heat source is controlled by scanning mirrors, and powder spread on base plate or previous solidified layers can be selectively melted by a high

energy laser beam based on the profile of each layer. Subsequently, building platform is lowered by one-layer thickness, and then new powder is spread by a recoater. An entire part can be acquired by the layer-by-layer melting and solidification of metallic powder [17].

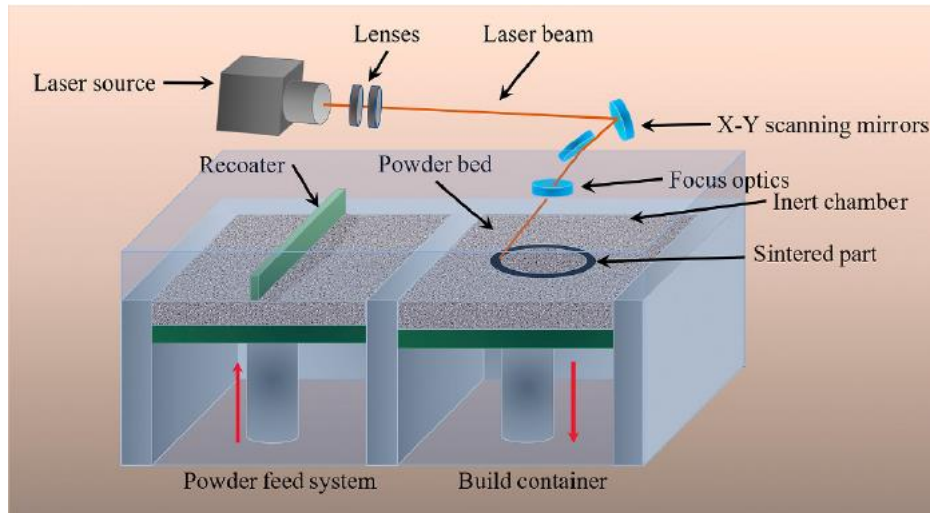


Figure 4: the schematic diagram of the LPBF process [17].

1.2.1. LPBF parameters

The final products are strictly influenced by the LPBF parameters and printing strategies. In the subsequent chapter they will be presented.

The Volumetric Energy density (VED) is a critical manufacturing characteristic for melting powder materials. This parameter reflects the laser beam's energy transmitted to a volumetric unit of powder material and correlates with several relevant laser and scan parameters [14], [18]. The empirical formula of VED is reported in Equation 21:

$$VED = \frac{P}{V * H * t} \quad \text{Equation 21}$$

VED is typically composed of four process parameters that are independently controlled and shown in Figure 5:

1. Laser power P [W]: it is the energy intensity of the laser beam;
2. Scanning speed V [mm/s]: it is the traverse speed of the laser beam;
3. Hatch distance H [mm]: it is the gap between two head-to-head scan pathways;
4. Layer thickness t [mm]: it is the thickness of a layer that equals one incremental amount of the powder bed.

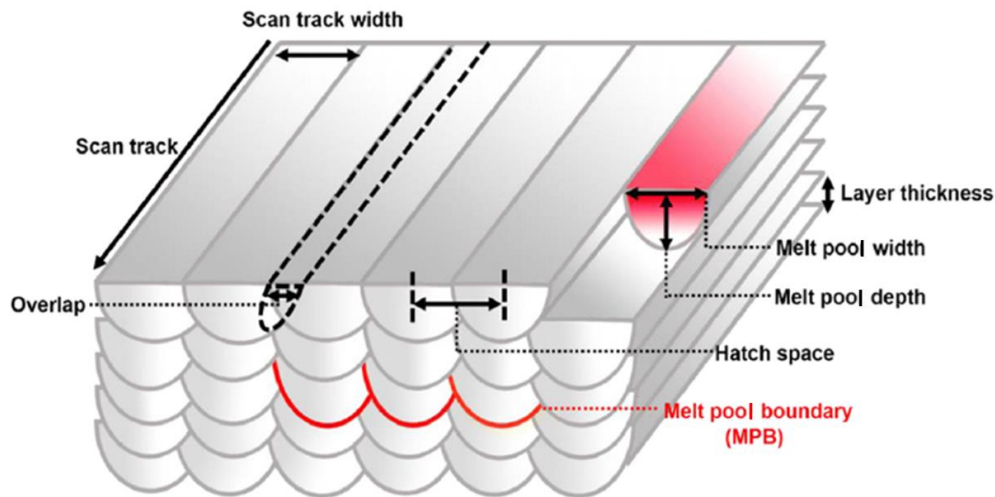


Figure 5: graphical representation of LPBF parameters [18].

An identical energy density value with different LPBF process parameters results in different material properties and these effects will be shown in the following chapter. In addition, the value of energy density differs from material to material, and the value greater than the materials specific energy density range leads to a wider and deeper melt pool.

The laser beam movement pattern influences the mechanical properties, microstructure and induced residual stresses on the printed parts. Most scholars have agreed that the use of shorter scan vector lengths minimizes the residual stresses on the printed part [15], [18]. Varieties of scanning strategy techniques are presented in Figure 6 to control the printed part's textures and densities. Island (chessboard), unidirectional and bidirectional are the most common scanning strategies in the LPBF process. The scanning strategy for a chessboard comprises of dividing the region into tiny cells [15], [18]. Unidirectional scanning is the most basic technique, and it usually results in the least amount of densification and the firmest texture, but other variations have superior densification behaviour. Scanning strategies depend on the type of materials and the required response study of microstructure and mechanical properties. When the number of melting cycles is increased, the cooling rate also increases, which improves the microstructure, mechanical property, hardness, and reduces porosity [15]. However, all the track melting methods highly depends on the energy density process parameters.

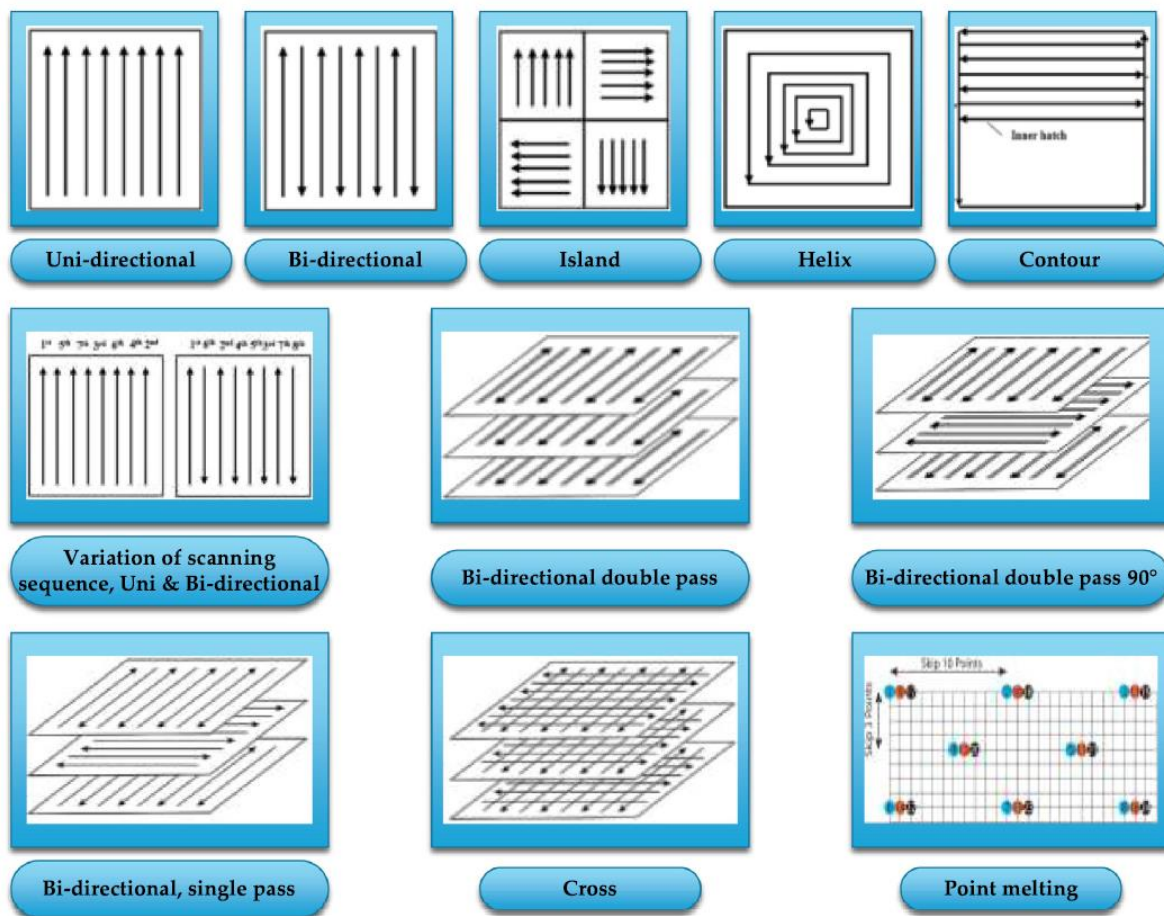


Figure 6: Common scanning strategies [18].

1.2.2. Effect of parameters on material properties

The process parameters in Laser Powder Bed Fusion play a vital role and influence the fabricated samples mechanical properties, e.g. hardness and tensile strength, and defects like pores and cracks. In the following section, the influence of parameters on LPBF products will be analysed.

Porosity

The amount of void volume in a solid substance is known as porosity, it is expressed as a percentage of the volume of voids to the total volume of the component [14]. LPBF alloy with high-density exhibits better tensile properties, impact energy, and reduced microstructure pores [15]. Therefore, understanding the factors affecting the relative density is essential. In LPBF components, there are three sorts of pores, including shrinkage pores, gas pores, and fusion errors. The fusion errors are caused by inadequate remelting of the last solidified layer and a weak metallurgical bond. These irregularly formed pores are observed at layer interfaces and brought on by gas

trapped between the powder particles. As the laser scanning process continues, the gas escapes, creating unstable scanning paths. The primary source of shrinkage porosity is a deficiency in the supply of liquid metal during the solidification process. Methods to reduce porosity can be adjusting the process parameters, preheating the substrate and remelting the solidified metal. The gas between the powder particles may dissolve in the molten pool if the packing density of the metal powder is low. Because of the rapid cooling rate during the solidification process, the dissolved gas cannot escape the molten pool's surface before it solidifies, and a gas pore is created [14].

The selection of process parameters plays a vital role in achieving desired properties with less defects. The most important parameter is the energy density. A too low energy density is not sufficient to completely melt the powders, leading to partial melting of powder particles. Partial melting results in more porosity and reduce the relative density of the built part [15]. However, other side, keyhole formation defects occur due to turbulence, spatter, and pores formations in molten pools at the high energy density [15], [19]. In particular, gas bubbles are produced by the surface vaporization of feedstock particles, and they gradually evolve to pores during solidification phase [17].

Hyer et al. [20] examined the relative density of LPBF AlSi₁₀Mg manufactured by independently varying processing. Figure 7 shows the nature of relative density at varying laser power, hatch space and layer thickness.

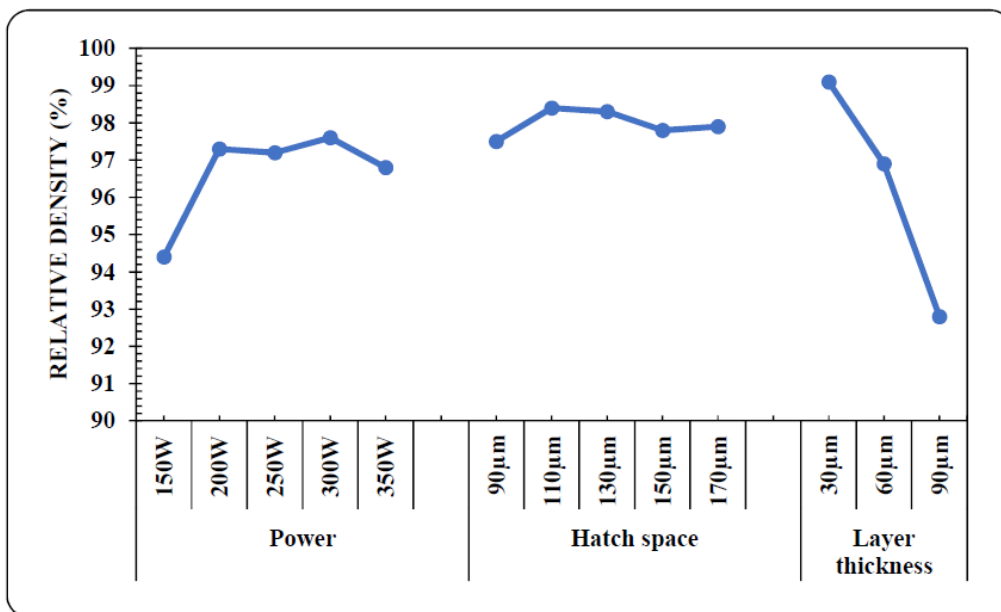


Figure 7: Relative density at varying laser power, hatch space and layer thickness [20].

Hardness

The hardness allows a part to resist plastic deformation, penetration, indentation, and scratching. It is an important part of the quality requirement. Consequently, a high hardness value increases resistance to wear from friction or erosion [14]. Laser Powder Bed Fusion parts exhibited a higher average hardness value compared to parts manufactured by conventional casting methods [15].

The impact of process parameters on the hardness was studied and the order of process parameters influencing hardness was found. As a general indication, the sample's microhardness gradually increases as VED is raised in response to a higher cooling rate [14]. The scan speed appeared to have the most impact on the hardness, followed by hatch distance, and laser power had the most negligible impact [15]. Figure 8 shows the graph between hardness at varying laser power, scan speed and hatch space. It decreases with the increment in laser power and decrement in scan speed and hatch distance in a given range.

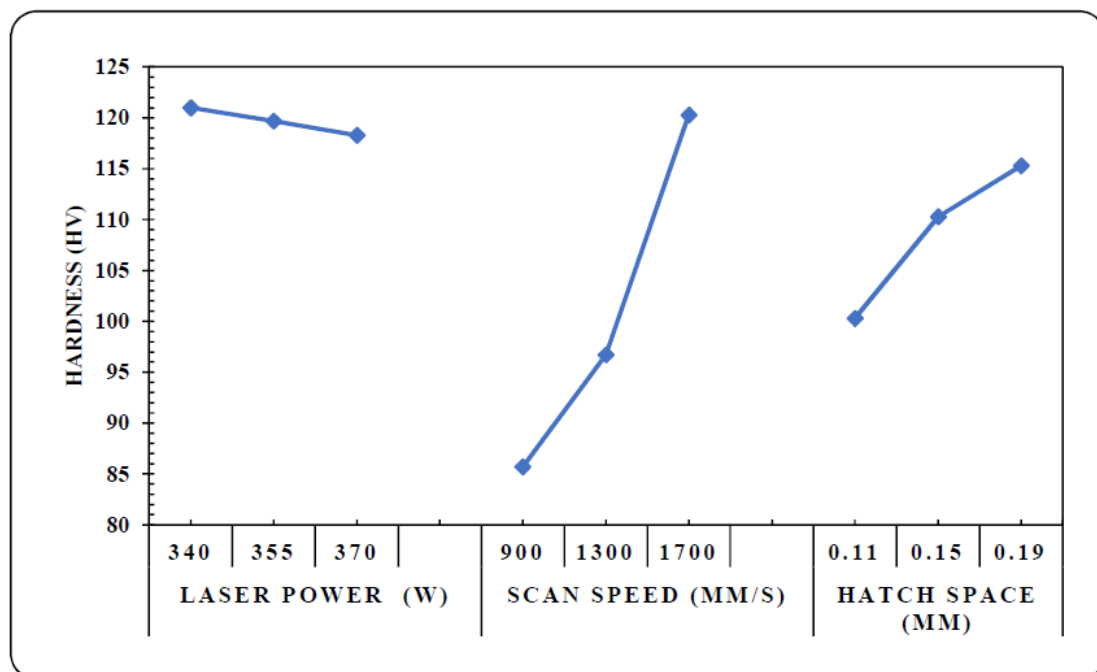


Figure 8: AlSi₁₀Mg LPBF produced samples hardness at varying laser power, scan speed and hatch space [21].

Surface roughness

The process type and parameters, particle size, layer thickness, the geometry of the part, and the orientation of the surface concerning the build direction all affect surface roughness (Ra). Ra is a crucial characteristic: when specimens are subjected to fatigue

cycles, it is widely acknowledged that it profoundly affects the material's strength. In addition, the ability to fabricate objects with minimal surface roughness is particularly desirable, as it can eliminate the need for extra production procedures [14], [15].

There are two significant causes of surface roughness. The first one is called balling phenomenon, which is sticking of unmelted solid powder particles on the surface due to insufficient energy. The second one is the Staircase effect, which depends on build angle and layer thickness, and which is attributed to the formation of layers of curved and inclined surfaces [15], [17].

Understanding the interaction between the various process parameters and changes in surface topology is crucial: laser power, powder feed rate, and traversal speed affect surface topology. An increment in energy density produced high roughness because of the balling phenomenon. The laser power revealed the same influencing trend on roughness. A better surface roughness can be provided at low scan speed because of improved molten layer solidification rate. However, too low scanning speed increases the liquid volume in the melt pool, which causes the melt pool to expand, generating thermal differences in the melt pool and resulting in a larger variance in surface tensions, which induces the balling phenomenon. Layer thickness is one of the most critical process parameters for dimensional accuracy and Ra. Decreasing layer thickness enhances dimensional accuracy and surface smoothness by minimizing the stair-case effect [14], [15].

Residual stresses

Stresses that remain inside a material when it is stable and in equilibrium with its environment are known as residual stress (RS). They are generated due to highly localized temperatures and quick temperature cycles brought on the material during the LPBF process.

A thermal stress is created by the laser's uneven heating and the resulting variances in thermal contraction and expansion between the areas close to and far from the molten pool or even between the metal matrix and the reinforcement particles. As a result, the material will incur volume expansions and contractions due to the numerous distinct volumes of phases that lead to structural stresses. Thermal stress is the most frequent cause of fracture initiation in LPBF [14]. Because melting and solidification are involved in laser-based AM, the significant temperature gradients caused by localized heating are the principal cause of RS. The high RS produced alters the mechanical properties, particularly the fatigue properties. Increasing the laser power and

decreasing the scanning speed result in a reduction in residual stress on the top surface.

Microstructure

The microstructure of the LPBF products can be tuned by optimizing in-process and post-process operations. Two parameters such as solidification speed and temperature gradient, heavily control the solidified structure, which is influenced by laser power, traverse speed, laser beam diameter, focusing geometry and powder characteristics [14]. The duration of interaction between the powder and laser beam determines the nature of the microstructure formed when parameters are adjusted.

Tensile strength

Tensile strength is one of the essential mechanical properties of any build component. It is substantially affected by the fabrication parameters such as laser power, hatch space, scan speed, built direction, baseplate preheating temperature and built environment.

Figure 9 represents the effect of scan speed on UTS and Elongation of an AlSi₁₀Mg sample obtained through LPBF. With an increase in scan speed, tensile strength first increases and then decreases, while elongation increased with the increase in scan speed [2,8]. The apex point in UTS curve can be explained with the appearance of internal defects in the material. Increasing the scanning speed, internal pores appear, lowering the tensile strength [15]. The other key factor affecting the tensile properties is the build orientation of the sample. The tensile properties are not identical when built along different directions hence exhibiting anisotropy behaviour. So, the choice of the correct scanning strategy is relevant [15].

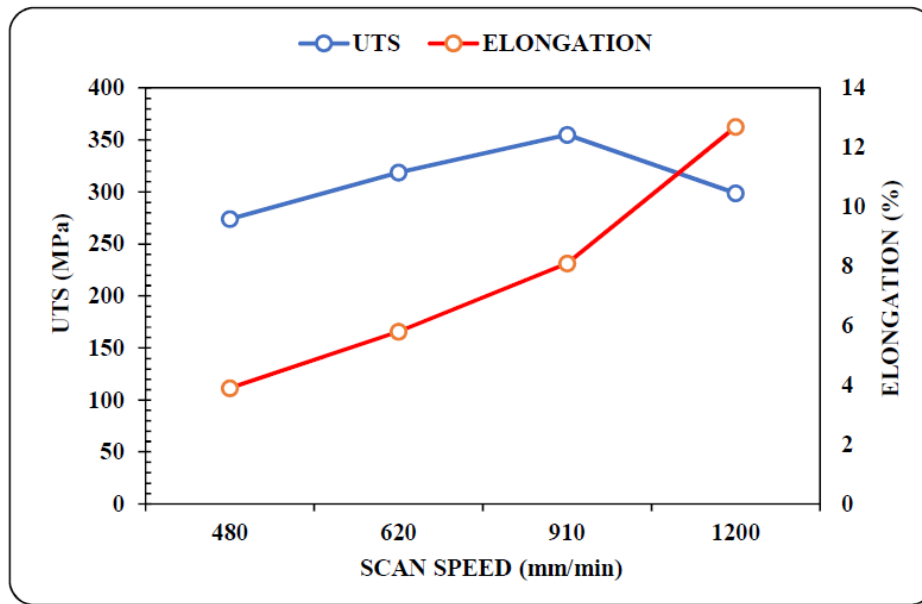


Figure 9: Effect of varying speed on UTS and Elongation of AlSi10Mg [22].

1.2.3. Powder

The fundamental ingredient in a LPBF process is the powder feedstock. Nowadays, the mechanical properties of the virgin metal alloys are no more sufficient to satisfy the commercial requirement. So, the aim is to obtain a metal matrix composite (MMC) material through LPBF with a high percentage of reinforcements particles, in order to enhance the characteristics of the metal matrix. The main difficulty is related to the achievement of a sufficient reinforcement composition, which is not always satisfied by traditional powder production methods like gas atomization.

Although AM, nowadays, is a well-known and concrete technique, the application of the LPBF to fabricate MMCs still encounters some challenges. One of the major challenges is the preparation of suitable composite powder particles [13], [23], [24]. The feedstock powder mixture of MMCs is composed of metal powder and reinforcement particles. In order to avoid detrimental defects in the bulk MMC, the material, size, and shape of the metallic powder should be appropriately chosen. In this section the selection about the shape and the size of the particles and the production methods will be discussed.

Influence of powder shape and size

In order to ensure the quality of LPBF-processed parts, the dimension and shape of feedstock powder is an important factor, because it can significantly affect the laser

absorption capability of powder as well as the geometric accuracy of parts. For the feedstock powder used in LPBF, the most ideal material should be spherical powder characterized by good flowability and spreading property [17]. Not only the shape but also the size of the particles plays a very important role in LPBF process. The particle size distribution (PSD) is usually between 20 and 63 μm : a so large distribution is needed in order to guarantee the filling of voids between the biggest powder particles. A too low PSD, however, is generally unwanted due to a resulting low flowability and high tendency to make clusters. On the other hand, also a too high distribution must be discarded to avoid low dimensional precision and bad surface finishing.

Powder production methods

In the sequent paragraph and in Figure 10, five different procedures to produce LPBF powder mixture to produce MMCs will be presented.

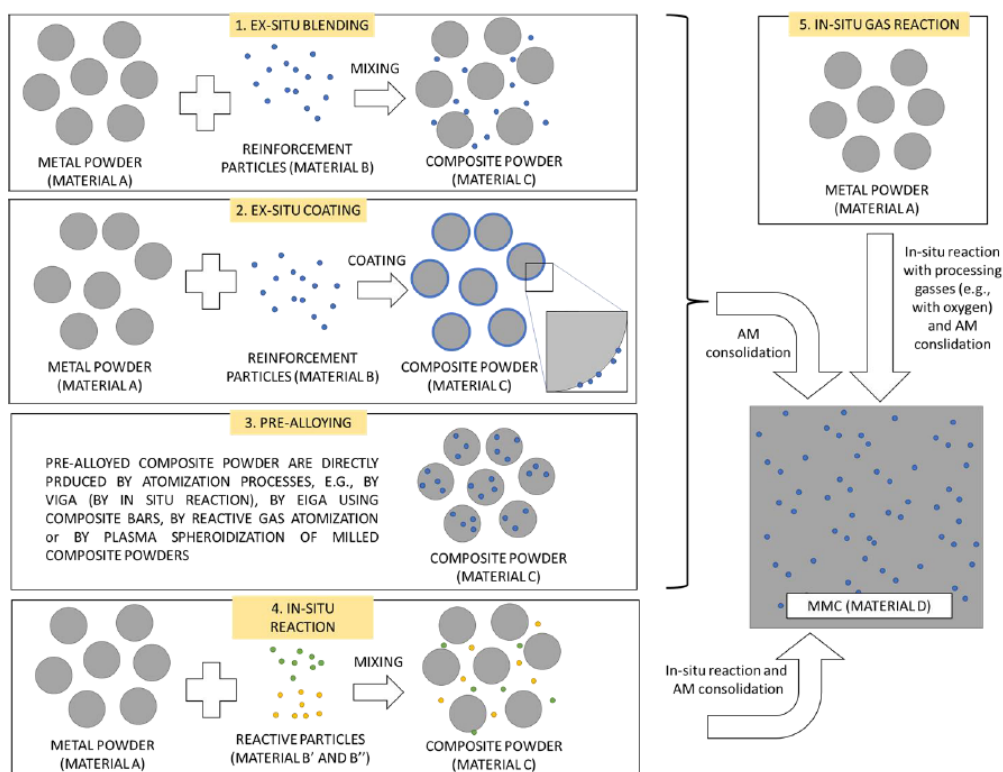


Figure 10: a schematic representation of the five routes to produce powder for MMC by LPBF.

Ex-situ blending

In ex-situ blending, the reinforcement particles are simply added to the metallic powder and blended, then the composite powder is processed by LPBF [25]. During the melting and solidification phase, no reaction between the powder and the particles is supposed to occur. One of the most common mixing strategy is ball milling, which

works on the principle of impact and attrition: powder particles are mixed and reduced in size by impacting with the surface of the mill and with the balls. The grinding balls are usually made of steel, ceramic materials or rubber [26], [27].

The advantages of this technique are the simplicity of powder mixing and the fact that it does not require an expensive equipment. In addition, ball milling technique can guarantee an effective reinforcements distribution [28]. On the other hand, ball milling leads to a change in powder morphology, in particular, powder particles are no more spherical after the milling process.

Another possibility to blend the powder is by mechanical mixing, where the powders are simply mixed at lower rotational speeds without grinding balls. This means that the impacts will be less energetic, so particles size reduction will not occur, and reinforcement particles will remain attached to the external surface of the bigger particles.

Ex-situ coating

This technique consists in applying a coating of reinforcement material on the metallic powder particles surface. Several methods, including plasma or electrostatic processes can be used to coat the surface of the metal powder particles with an external shell of reinforcing particles [17], [29]. In this way, it is possible to obtain a homogeneous distribution of reinforcement avoiding sedimentation or separation – phenomenon that can happen during powder sieving – of the feedstock material. In addition, sub-micron or nano-sized reinforcement particles can be used, leading to a more effective strengthening. However, this method is expensive, thus it is not suitable for very large scale production of feedstocks.

Gas atomization

Trough gas atomization it is possible to obtain a pre-alloyed metallic powder with embedded reinforcement particles, with an average dimension that can go from the micro to the nano scale, which can be directly used as feedstock materials for LPBF [17].

The gas atomization process, showed also in Figure 11, starts with molten metal alloy pouring from a tundish through a nozzle. The stream of molten metal is then hit by jets of inert gas such as nitrogen or argon and atomized into very small droplets that cool down and solidify when falling inside the atomization tower. Powders are then collected, sieved, and separated according to size ranges. This process is the most common process to produce spherical metal powders for additive manufacturing with

a homogeneous distribution of reinforcements. However, it is not suitable to produce feedstock powder with a high percentage of reinforcements.

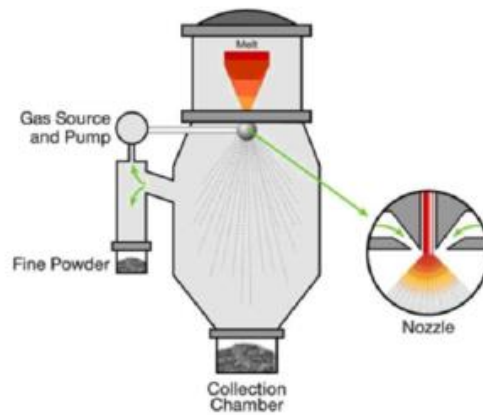


Figure 11: Representation of the gas atomization process.

In-situ reaction

In in-situ reaction method, the metallic powder is blended or coated with specific reactant particles that are able to combine together or with the alloying elements present in the metal powder to create reinforcing particles inside the metal matrix during the LPBF process. However, this strategy can show some difficulties in reaching a homogeneous distribution of the reinforcing particles and residues of the reacting particles can be found in the final bulk material [30].

In-situ gas reaction

The last production methods is the in-situ gas reaction, which implies a reaction between the metallic powder and the processing gas during LPBF process, to form a composite material. So, no mixing or deposition processes are required and there is not risk of sedimentation or separation of the reinforcement from the matrix powder [31]. The limits of this process are related to the nature of the possible reinforcement that we can obtain (generally only oxides particles) and to the difficulties in regulating the reinforcements quantity that we can obtain in the final feedstock.

1.2.4. Defects in LPBF products

The aim of introducing reinforcing particles in a metal matrix is to improve the performances of composite material. However, properties of LPBF-produced MMCs can be affected by some defects that can arise during the printing process. In the following section, a brief description of the possible defects is reported.

The formation of pores is a critical issue that can impose a significantly negative effect on properties of parts. In the LPBF of particulate reinforced Aluminium MMCs, the formation of pores was mainly caused by entrapped gas, lack of fusion, and keyholing [32], [33]. These three possible scenarios were already described in section 1.2.2.

Another common defects in LPBF are cracks. In particular, three distinct types of cracks can be found [32], [33]:

1. Hot crack (solidification crack): solidification cracks are mainly formed during the solidification shrinkage and the thermal contraction of the material, leading to the production of tensile stress in new solidified melt. If the strength of new solidified melt is lower than tensile stress, cracks will be produced.
2. Cold crack: it is mainly caused by the formation of residual stress, resulting from a temperature gradient mechanism and the shrinkage of melt top because of thermal contraction.
3. Delamination crack: delamination refers to the separation between adjacent solidified layers. This kind of crack is produced when the residual stress formed between consecutive solidified layers surpasses the yield strength of materials.

During LPBF process remarkably high temperature can be involved, leading to the loss of alloying elements due to vaporization. Some elements are easier to be vaporized because they have a higher equilibrium vapor pressure, which can affect the microstructure and properties of parts. In order to reduce the vaporization of alloying elements during the LPBF of particulate-reinforced MMCs, the use of a too high laser power or a too low scanning speed should be avoided.

The surface roughness of parts is also a vital feature, and this defect can be evaluated by the average surface roughness (R_a), which can be described by Equation 22.

$$R_a = \frac{1}{N} \sum_{n=1}^N |f_n| \quad \text{Equation 22}$$

Where f_n is the height of a peak or the depth of a valley on the surface of parts, and N is the number of testing points [17], [34]. The formation mechanism of poor surface roughness mainly includes two types. First, the existence of “stair step effect” can increase R_a , which is attributed to the formation of layers of curved and inclined surfaces. Second, the insufficient melting of powder and defects of pores and balling can increase R_a .

The formation of balling is also an important problem for the surface appearance of Al LPBF-processed parts. Fundamentally, balling is mainly controlled by wettability [35].

During printing process, ellipsoidal balls are formed due to the poor wettability of the molten metal on the substrate or previous layers.

2 Aim of the thesis

This thesis is aimed at studying different methods to produce 2618-7wt%TiB₂ metal matrix composite (MMC) feedstocks with high Laser Powder Bed Fusion (LPBF) processability. 2618 is a common Al alloy for high temperature applications. The addition of TiB₂ particles is supposed to increase the microstructure stability at high temperature, the strength, and the stiffness of the alloy. Moreover, 2618 has a high tendency to form hot cracks. TiB₂ proved to be an effective grain refiner able to reduce the alloy hot crack sensitivity. This work is mainly focused on the development and characterization of the composite feedstock and on the effect of the different powder configurations on the final material properties. Four different methods were used to produce composite powders: 1) low and 2) high energy mechanical mixing, 3) plasma assisted coating and 4) pre-alloying by gas atomization. The four processes led to four different powder configurations with TiB₂ particles attached to the powder surface (1,2,3) or embedded in the Al matrix (4). The powders were fully characterized by Scanning Electron Microscope (SEM), powder rheometer and mechanical sieve. Bulk samples were manufactured by LPBF using the four powder batches. Process parameters were varied according to a DoE approach in order to obtain the highest material density. The samples were analysed by SEM to observe the grains microstructure and the borides distribution, and material hardness was tested.

3 Materials and methods

3.1. Materials

In this section, the feedstock powders and their relative production methods are presented. The basic metallic alloy is an Aluminium 2618 alloy with a nominal composition listed in Table 1.

Element	Al	Cu	Si	Fe	Mg	Ti	Ni	Other
Composition range (wt%)	Balance	1.9-2.7	0.10-0.25	0.9-1.3	1.3-1.8	0.04-0.1	0.9-1.2	0.05

Table 1: Aluminium 2618 alloy composition.

Different feedstock production methods were employed in this study to produce 2618/7wt%TiB₂ MMCs:

- Low energy mechanical mixing
- High energy mechanical mixing
- Plasma assisted deposition method
- Pre-alloying by gas atomization

3.1.1. Low energy mechanical mixing powder

The first powder feedstock was produced in Politecnico di Milano laboratories by mixing for 2, 4 and 8 hours at maximum speed of 40rpm a mixture of Al 2618 powder and of TiB₂ powder (7% in weight) using a drum mixer. As a result of the mixing, the reinforcement particles of TiB₂ remained attached to the surface of the Al 2618 powder particles. A composite feedstock was obtained. The 2618 alloy was produced by Kymera International GmbH company, while the TiB₂ powder was produced by Höganäs SA. In Table 2 the alloy acceptance limit and the nominal chemical composition of the four different composite powders are reported.

Chemical composition (wt%)							
Element	Al	Cu	Mg	Fe	Ni	B	Ti
Acceptance Limit		1.9-2.7	1.3-1.8	0.9-1.3	0.9-1.2	2.0-2.4	5.0-6.0
Low energy mixing	Balance	1.96	1.2	0.93	0.93	1.8	3.8
High energy mixing		1.76	1.3	1.0	0.99	1.75	4.04
Plasma deposition		1.7	1.2	1.0	0.9	2.3	5.3
Pre-alloying		2.1	1.3	1.0	1.0	0.8	4.1

Table 2: feedstocks chemical compositions and acceptance limit.

For what concerns low energy mechanical mixing strategy, all the alloying elements of the composite powder were within the acceptance limits, except for B and Ti which were present in a lower amount than expected.

3.1.2. High energy mechanical mixing powder

The second batch under investigation consists of a MMC alloy where the addition of reinforcement was achieved by high energy mechanical mixing under protective atmosphere (Nitrogen) and at room temperature, performed by IMR GmbH. The dry mechanical mixing process generates enough energy input to provide the required surface impact for the additives on the base Aluminium alloy powder particles, without deforming them. Further specification regarding the production method cannot be added since they were not disclosed by the producer.

The chemical composition of the feedstock provided by IMR GmbH is reported in Table 2. Also in this case, Ti and B content was lower than expected.

3.1.3. Plasma assisted deposition powder

For the production of the third feedstock powder a low-pressure plasma coating process was performed by AM4AM S.r.l. This process consists in injecting a mixture of metal powder and ceramic in a cold plasma discharge. The energy of the plasma

activates the surface of both types of particles and induce the preferential attraction between them (smallest on largest).

The chemical composition declared by the producing company is reported in Table 2. It is possible to observe that the content of copper and magnesium is slightly lower with respect to the acceptance limits; on the other hand, the concentration of Ti and B is compliant to the request.

3.1.4. Pre-alloyed powder

The fourth feedstock powder under investigation was a pre-alloyed gas atomized powder produced by Kymera International GmbH and consisted of 2618 alloy modified by the addition of 5.5wt% of Ti and 2.2wt% B. However, the production method showed some limitation, especially regarding the concentration of B which is much lower than that expected. The actual chemical composition of gas atomized powder provided by Kymera company is reported in Table 2.

3.2. Process and characterization equipment

3.2.1. LPBF sample production

For each powder, nine different cubic samples, with dimensions equal to 8x8x8mm³, were printed through LPBF using the Reduced Build Volume (RBV) system of Renishaw AM250 (Figure 12). The main characteristic of this instrument is that the laser beam is pulsed, not continuous, so it will remain on the same portion of material for a certain amount of time, called time of exposure. As a result, many consecutive melt pools will be generated with a certain distance (point distance) along the same scanning line, as shown in Figure 13 [36].

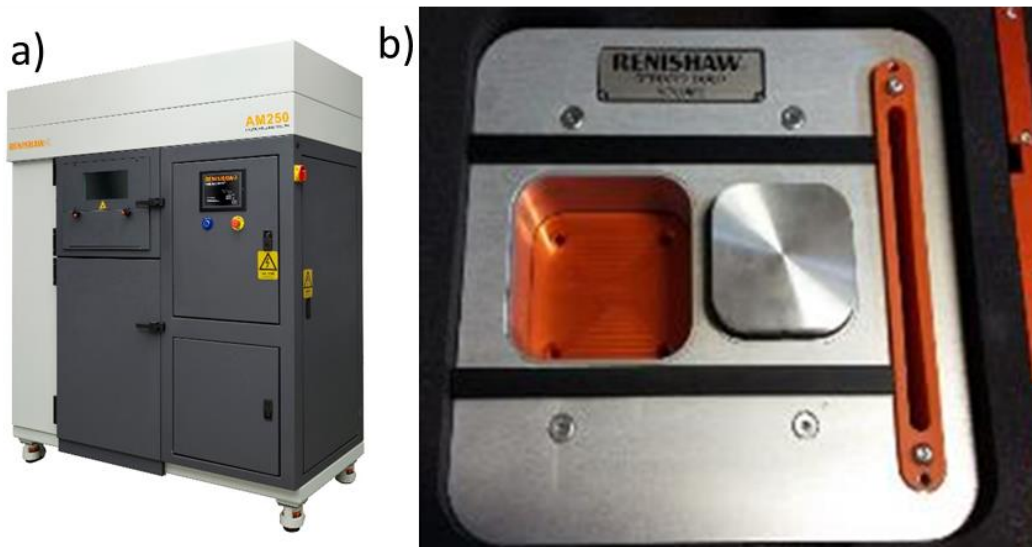


Figure 12: Renishaw AM250 printer (a) and RBV system (b).

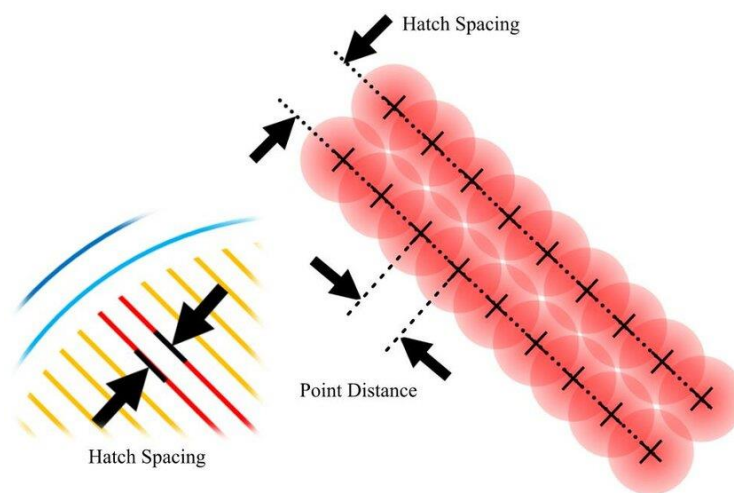


Figure 13: Illustration of the difference between hatch distance and point distance [36].

The parameters used for the Design of Experiment (DOE) are reported below in Table 3 and Table 4.

Fixed parameters	
Laser Power	200 W
Time of exposure	140 μ s
Layer thickness	25 μ m

Table 3: fixed printing parameters.

Varying parameters		Hatch distance [mm]		
		0.08	0.1	0.12
Point distance [mm]	0.06	A	B	C
	0.08	D	E	F
	0.10	G	H	I

Table 4: varying printing parameters.

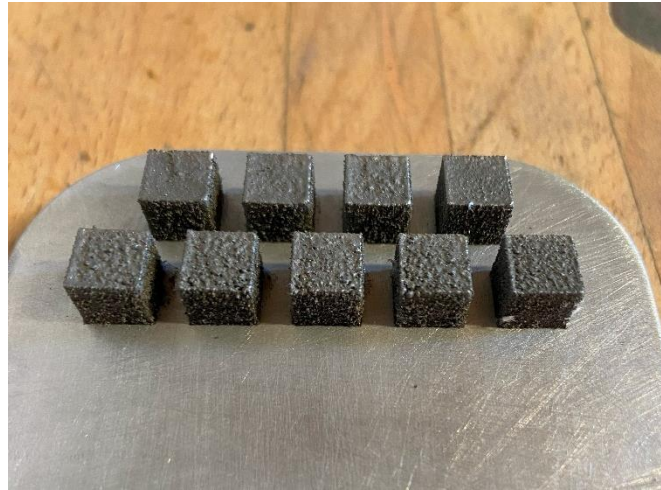


Figure 14: Representative image of cubic samples.

As the cubic samples, shown in Figure 14, have been obtained, they are cut on a plane perpendicular to the plane identified by the scanning directions and moulded into a polymeric resin, to facilitate the polishing steps and further analyses.

3.2.2. Optical microscope and ImageJ

Light optical microscope Eclipse LV150NL was used to analyse geometrical features, porosity and microstructure of LPBF parts. Eclipse LV150NL is a manual, nosepiece type microscope which is equipped with lenses from 25X to 1000X magnification.

ImageJ software was used in order to analyse and quantify the porosity of the samples. Images taken from the optical microscope were transformed in 8-bit colour format and then, choosing a suitable colour threshold, the average size of the material pores and the percentage of porosity could be evaluated. This process is shown in Figure 15.

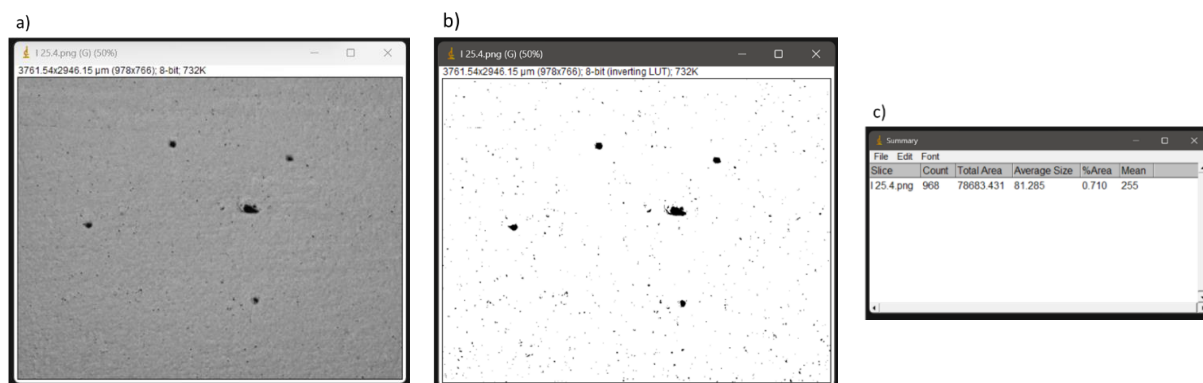


Figure 15: a) an 8-bit colour image taken from the optical microscope; b) the same image after the threshold is set; c) final analysis: the material in the example image has an overall porosity equal to 0.71% and an average pore size of 81.285 μm .

3.2.3. SEM

A field emission scanning electron microscope (FE-SEM) was used for microstructural analyses. The model used was a Zeiss Sigma 500, equipped with energy dispersive X-ray analysis (EDS) Oxford Instruments Ultim Max model and electron backscatter diffraction (EBSD) detector mod. Oxford Instruments C-Nano.

SEM was used for the study of powders and AM materials in order to investigate microstructure and chemical composition. It was also used for the realization of the Inverse Polar Figure (ICP) and phase maps, in order to analyse the dimension and distribution of the grains and borides content.

3.2.4. XRD

In order to quantify the amount of TiB_2 presents before and after sieving, a Rigaku SmartLab diffractometer employing $\text{Cu K}\alpha$ radiation was used. The data were obtained in the diffraction angle range $20^\circ \leq 2\theta \leq 80^\circ$, with a step width of 0.02° and a velocity of $1^\circ/\text{min}$.

3.2.5. Microhardness tests

Leica VMHT 30 was used to perform microhardness testing. It is provided with a standard pyramidal Vickers indenter and it offers different levels of load force.

For the testing of the samples a load of 200g and dwell time of 10s was used in order to evaluate the hardness of LPBF samples.

3.2.6. Mechanical mixer

The powder feedstock (2618 + TiB₂) was mixed with the laboratory drum mixer Adler Mixer-T0, in order to let the TiB₂ reinforcement particles to remain superficially attached to the bigger Al 2618 powder particles.

3.2.7. Sieve

A vibrating mechanical sieve – with a 63 µm mesh – was used to filter and remove contaminants from the unmelted powder after the LPBF process.

3.2.8. Powder rheometer

A FT4 Powder rheometer (Freeman Technology Ltd) was used to analyse the powder feedstock flowability. The FT4 employs a precision blade that is rotated and moved downwards through the powder to establish a precise flow pattern. This causes many thousands of particles to interact, or flow relative to one another, and the resistance experienced by the blade represents the difficulty of this relative particle movement.

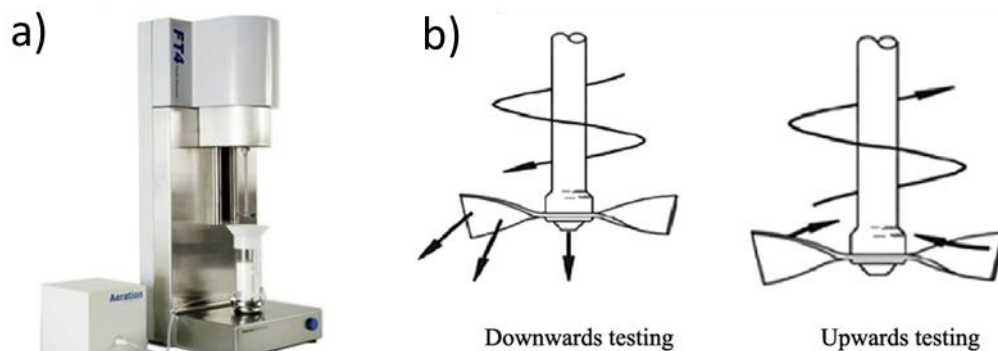


Figure 16: FT4 powder rheometer (a) and blade allowed movements (b).

The tests were performed three times for each powder. This procedure results in the following output parameters [37]–[39]:

- Basic flowability energy (BFE): it is a dynamic powder property measured during a downward traverse of the blade that forces the powder against the confining base of the test vessel. BFE quantifies confined or forced flow behaviour under low to moderate stress conditions. A higher value indicates increased mechanical interlocking and friction, leading to poor flowability.
- Specific energy (SE): it is measured during an upward traverse of the blade and quantifies the unconfined, or gravity-dominated, flow properties of a powder in a low stress state. A higher SE is indicative of increased mechanical

interlocking and friction that can contribute to blockages and other flow problems.

- Conditioned bulk density (CBD): it is the bulk density measured after a specific conditioning phase. The dynamic capability of the FT4 allows for the powder to be conditioned to establish a low stress, homogeneous packing state. As this process is automated, it is independent of the operator and results in a very reproducible packing state.

3.2.9. Particle Size Analyser

Particle size distributions (PSD) of the four powder batches were determined using a Laser Diffraction Particle Size Analyser Mastersizer 3000, Malvern Panalytical. The D10, D50, and D90 values are considered. Those parameters indicate the percentage (10%, 50% and 90%) of analysed particles characterized by a diameter lower than a certain value.

3.3. Metallographic preparation

Bitech C100 precision cutter was used to cut the bulk cubic sample in half along a plane perpendicular to the scanning direction.

The mounting press EP 50 made by Hitech Europe was used for the hot mounting of specimens to facilitate polishing operations. A polymeric resin in form of powder was used.

Forcipol 1V was used for polishing samples with manual operations. It works with abrasive papers ranging from 60P up to 2500P. Once that a perfect polished surface was obtained with the 2500P paper, the automatic polishing Tegramin by Struers was used for the last steps, involving silica nanoparticles suspension.

Chemical and electrolytic etching were performed using Keller's reagent.

4 Results

4.1. Powder analysis

4.1.1. SEM and Chemical analyses

In the following sections, the results of the SEM analyses performed on the four different powder feedstocks are showed. In addition, EDS and ICP analyses are reported.

Low energy mechanical mixing powder

In Figure 17 a SEM image of low energy mechanical mixed powder is shown, while in Table 5 the relative EDS analyses on the selected areas and spots present in Figure 17 are reported.

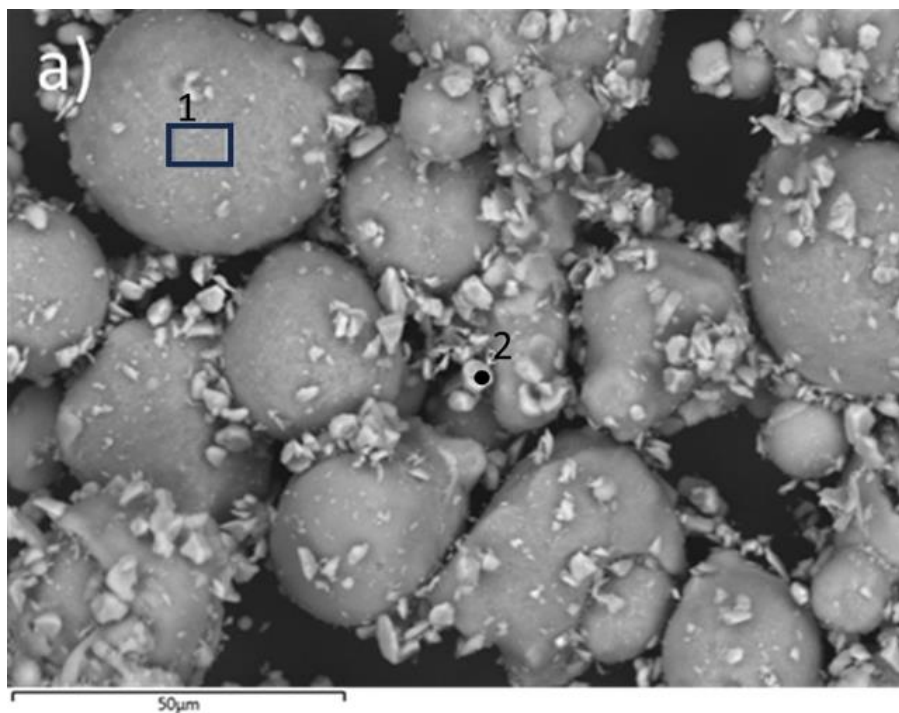


Figure 17: low energy mechanical mixed powder batch SEM analysis.

Element	Area 1		Spot 2	
	Weight concentration (wt%)	Standard deviation	Weight concentration (wt%)	Standard deviation
Al	92.1	0.3	-	-
Cu	2.2	0.2	-	-
Mg	1.5	0.1	-	-
O	1.4	0.2	-	-
Fe	1.2	0.1	-	-
Ni	0.9	0.1	-	-
Ti	0.6	0.1	82.3	0.7
B	-	-	17.7	0.7

Table 5: EDS analysis composition of selected areas – low energy mechanical mixing powder.

This feedstock is obtained by mixing two different powders: Al 2618 and TiB₂. Aluminium particles are characterized by a spherical shape and the D10, D50, and D90 values were 31.6µm, 52.2µm and 83.9µm respectively. According to the technical datasheet, TiB₂ particles contain 30,3wt% of B, traces of C, N and O. The supplier also provided the following PSD for the TiB₂ batch: D10=0.8 µm, D50=3.2 µm and D90=5.6 µm.

As it is possible to see from the SEM images reported in Figure 17, during the low energy mechanical mixing process, a great amount of TiB₂ particles remain physically attached to the Al 2618 alloy powder particles, without changing their shape and dimension. However, some reinforcements remain dispersed in the powder batch without adhering to Aluminium powder surface.

The evaluation of the PSD of the mixed feedstock reports values for D10, D50, and D90 equal to 27.2 µm, 49.8 µm and 83.0 µm respectively. These values are comparable with those previously reported for the standard 2618, except for the D10 value which is

slightly lower due to the presence of the small ceramic reinforcement phase. The Particle Size Distribution (red curve in Figure 18) shows a bimodal distribution where the main symmetric peak corresponds to pure 2618 particles, and the smaller peak is mainly due to the presence of ceramic reinforcement that has a main equivalent diameter of 4 μm .

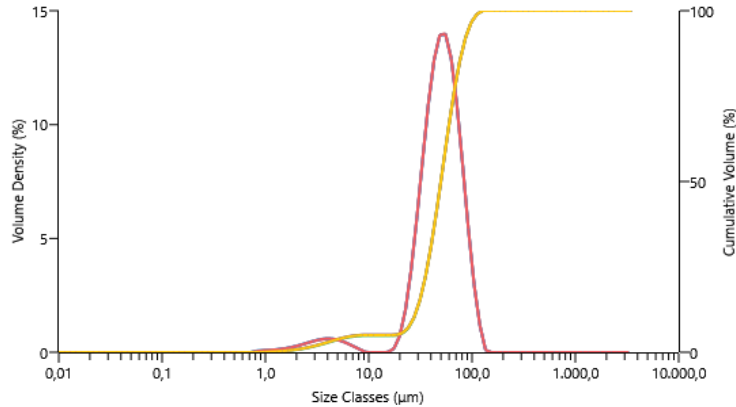


Figure 18: Particle size distribution of low energy mixed feedstock.

The chemical composition of the low energy mechanical mixed batch, obtained by Inductively Coupled Plasma Optical Emission Spectrometry (ICP-OES) technique (Table 6), shows that all the alloying elements were within the acceptance limits except for B and Ti which were present in a lower amount than expected. It has to be noted that since the TiB_2 were added ex situ the expected atomic ratio between B and Ti is 2. However, by performing the calculation of the atomic ratio with data obtained from ICP measurements, a value of 1.5 is obtained. This result shows some limitations in the ICP-OES measurements of light elements such B. In particular, in the ICP-OES method, the Boron concentration is detected on the basis of the value of the electromagnetic radiation emitted by excited B atoms. Typically monitored wavelengths characteristic for Boron are 182.52, 249.678 and 249.773 nm. However, some interferences can arise during the analysis. The most common interferences with boron determination are with Iron and Chromium [40]. Since Fe is present in Al 2618 alloy, it is reasonable to suppose that the estimation of Boron content is distorted by Iron interference.

Chemical composition (wt%)								
Element	Al	Cu	Mg	Fe	Ni	Si	Ti	B
Acceptance Limit	Balance	1.9-2.7	1.3-1.8	0.9-1.3	0.9-1.2	0.10-0.25	5.0-6.0	2.0-2.4
ICP Low energy mixing		2.3	1.55	1.1	0.9	0.21	3.8	1.3
ICP High energy mixing		1.8	1.3	1	0.9	0.19	3.8	1.24
ICP Plasma deposition		1.7	1.2	1	0.9	0.2	5.1	2.3
ICP Pre-alloying		1.9	1.6	1.1	1.1	0.25	3.3	0.3

Table 6: Acceptance limit composition and experimental ICP-OES composition of the four feedstocks.

Different mixing times were actuated in order to establish the best route that allows to obtain a homogeneous distribution of reinforcements. The rotation velocity of the drum mixer was maintained constant, while three mixing durations were chosen: 2, 4, and 8 hours. In Figure 19, SEM images of the three different batches mixed for different times are reported.

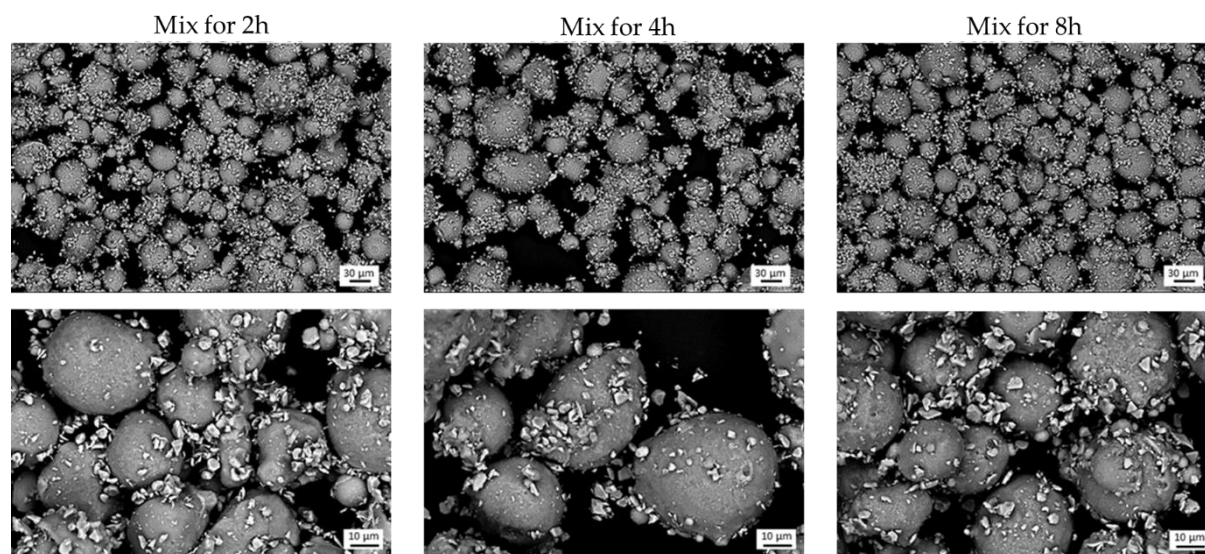


Figure 19: SEM images of low energy mechanical mixed powder mixed for 2, 4 and 8 hours.

Regardless of the mixing time, it was noted that TiB_2 particles were well dispersed in the powder batches, they were attached onto the surface of the 2618 powder, and no significant clustering of ceramic particles was noticeable. The results of the mixing strategy show that 2 hours are enough to achieve a homogeneous distribution of the particles.

High energy mechanical mixing powder

In Figure 20, the SEM image of the high energy mechanical mixed feedstock is reported, while Table 7 shows the results of the EDS analyses.

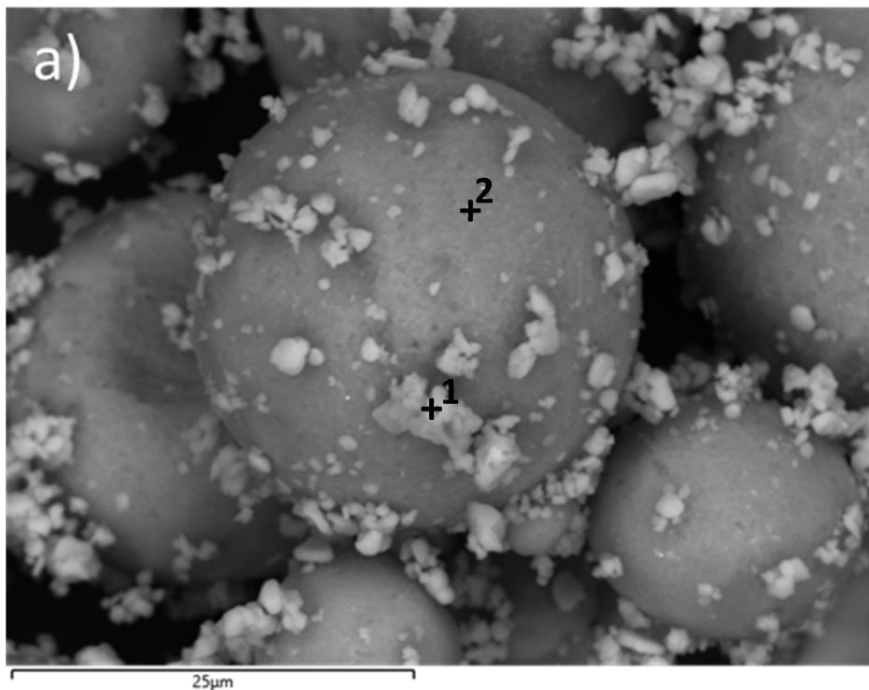


Figure 20: SEM image of high energy mechanical mixed powder batch.

Element	Spot 1		Spot 2	
	Weight concentration (wt%)	Standard deviation	Weight concentration (wt%)	Standard deviation
Al	15.5	0.3	94.5	0.2
Cu	0.4	0.1	1.8	0.2
Mg	0.2	0	1.4	0.1
Fe	-	-	1.0	0.1
Ni	-	-	0.8	0.1
Ti	40.8	0.7	0.5	0.1
B	43.1	0.9	-	-

Table 7: EDS analysis composition of selected spots – high energy mechanical mixing powder.

For what concern the second powder batch, similar considerations can be made regarding the mechanism of TiB_2 adhesion on Aluminium particles. Reinforcements remain attached to 2618 powder thank to the collision that occur during the mixing, with the difference that the collision in this last case are more energetic. As a result, from a visual inspection, it can be noticed that all the reinforcements are attached to the Al particles.

Figure 21 shows a bimodal particle size distribution; similarly, to what observed for the previous powder batch, the first weak peak can be attributed to the presence of the reinforcement: in fact, SEM image (Figure 20) confirm the micrometric dimension of these particles, whose size varies between 1 and 4 μm . The second peak is related to Al bigger particles. The values of D10, D50 and D90 of the whole feedstock were 18.5 μm , 39.8 μm and 74.4 μm , respectively.

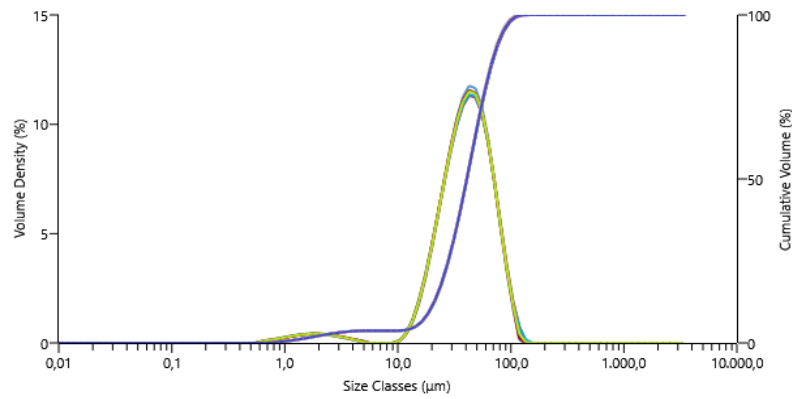


Figure 21: Particle size distribution of high energy mixed feedstock.

The ICP-OES analysis of the powder (Table 6) evidenced that copper is the only alloying element with a concentration which was slightly lower than that expected; on the other hand, the quantification of Ti and B reveals a low content of both these elements. However, as reported in the previous powder batch description, ICP-OES measurements show some limitations dealing with light elements, such as B.

Plasma assisted deposition powder

Figure 22 represents the SEM image of the composite powder particle obtained by the plasma assisted deposition process. In Table 8 the EDS analyses are reported.

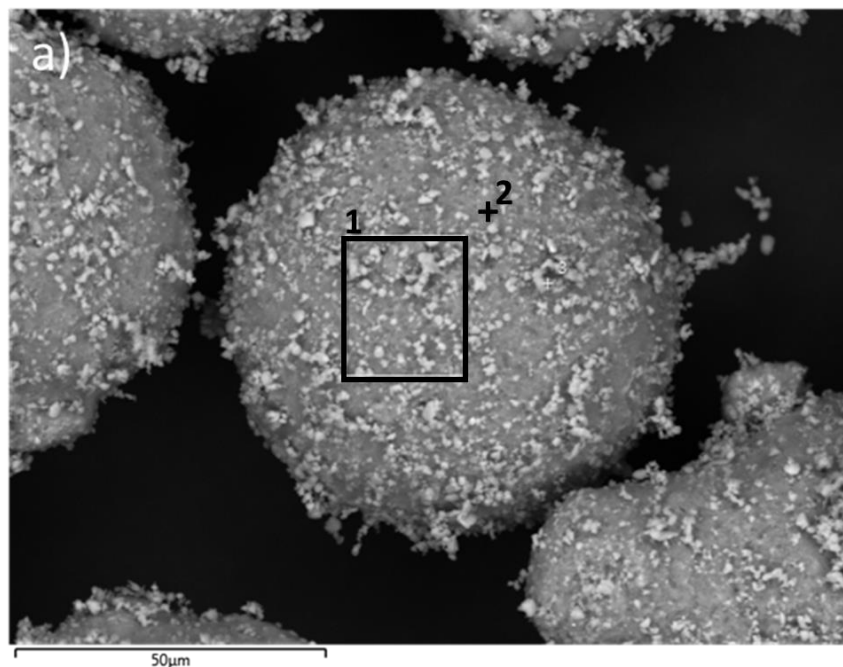


Figure 22: SEM image of plasma deposition powder.

Element	Area 1		Spot 2	
	Weight concentration (wt%)	Standard deviation	Weight concentration (wt%)	Standard deviation
Al	64.8	0.6	78.9	0.8
B	15.0	0.8	0.6	0.9
Ti	14.9	0.2	7.6	0.2
Cu	1.9	0.2	1.6	0.2
Ni	1.1	0.1	0.7	0.1
Fe	1.0	0.1	0.7	0.1
Mg	0.8	0	0.9	0.1

Table 8: EDS analysis composition of selected area and spot – plasma deposition powder.

The particle size distribution of the feedstock obtained through plasma assisted deposition is reported in Figure 23. Also in this case a bimodal distribution is noticeable: the first peak, centred at approximately 2 μm , can be attributed to the TiB_2 particles. This size agrees with that observed by the analysis on SEM image reported in Figure 22, i.e., between 1 and 3 μm . The values of D10, D50 and D90 were determined as 19.85 μm 39.73 μm 71.03 μm , respectively.

From a visual inspection of SEM image, it is possible to see a homogeneous distribution of the TiB_2 particles decorating the surface of the powder particles. This case is characterized by much smaller reinforcements with respect to the two powder batches obtained through low and high energy mixing.

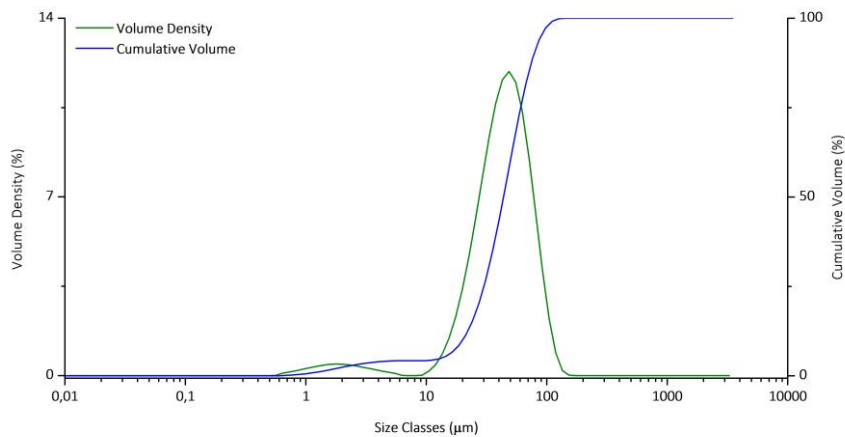


Figure 23: Particle size distribution of plasma deposition feedstock.

From ICP-OES composition reported in Table 6, it is possible to observe that the content of copper and magnesium is slightly lower with respect to the acceptance limits; on the other hand, the concentration of Ti and B is compliant to the request.

Pre-alloying powder

The pre-alloyed powder is represented in Figure 24, while its EDS composition is reported in Table 9.

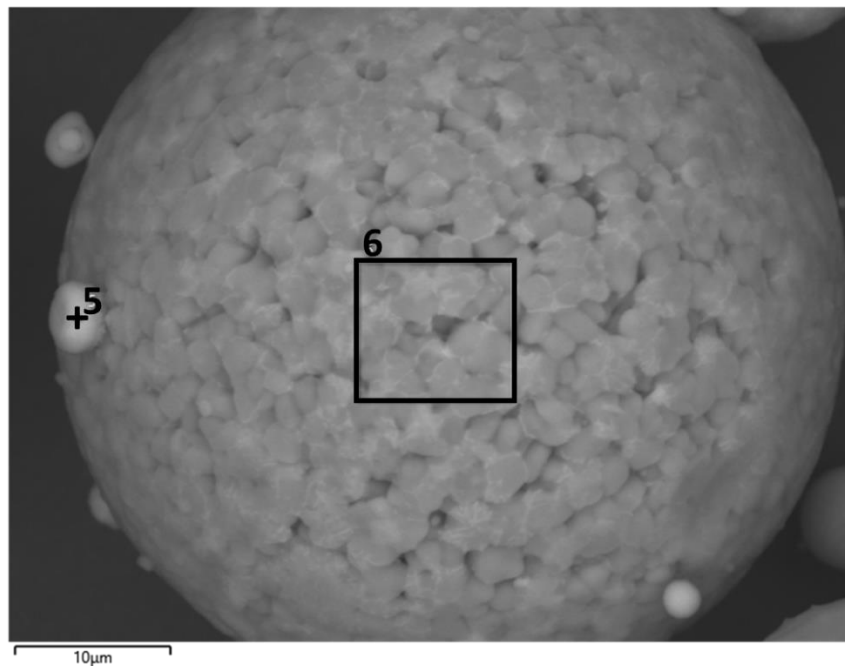


Figure 24: SEM image of pre-alloyed powder.

Element	Spot 5		Area 6	
	Weight concentration (wt%)	Standard deviation	Weight concentration (wt%)	Standard deviation
Al	84.7	0.3	91.6	0.2
Cu	5.0	0.2	2.0	0.2
Ti	4.9	0.1	3.2	0.1
Fe	2.7	0.2	1.2	0.1
Ni	2.7	0.2	1.0	0.1
Mg	-	-	1.2	0.1

Table 9: EDS analysis composition of selected area and spot – pre-alloyed powder.

The PSD of the pre-alloyed powder, reported in Figure 25, shows a curve with a narrow Gaussian shape. The determined values of D10, D50 and D90 were 30.3 μm , 44.8 μm , and 65.5 μm , respectively.

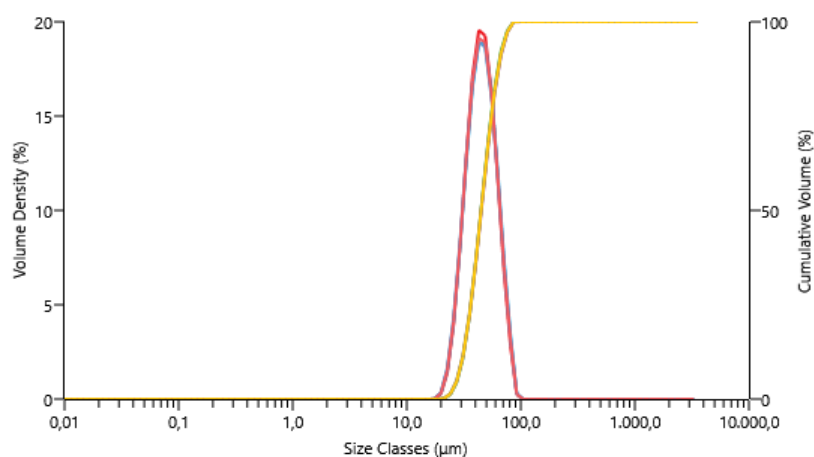


Figure 25: Particle size distribution of gas atomized feedstock.

The analyses, performed by ICP-OES technique reported in Table 6, show that the concentration of alloying elements such as Cu, Fe, Mg, Ni, Si are within the acceptance limits defined for this project; on the contrary, both titanium and boron are present in an amount significantly lower than that requested, around 3% wt.

Reinforcements are produced in situ, during the atomization process. In Figure 26, a powder particle section is reported, which shows tiny TiB_2 particles ($<1\mu\text{m}$), indicated by the blue arrows, dispersed in the matrix.

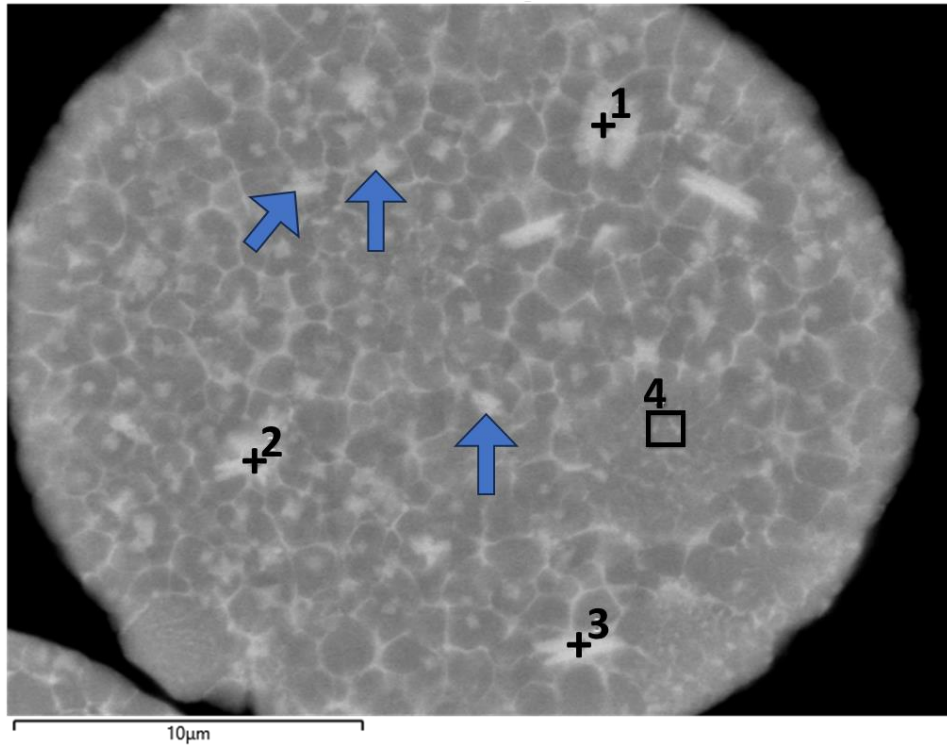


Figure 26: SEM image of a section of a pre-alloyed powder particle.

In Table 10, the EDS analyses on the selected area and spots of the powder section SEM image (Figure 26) are reported.

Element	Spot 1		Spot 2	
	Weight concentration (wt%)	Standard deviation	Weight concentration (wt%)	Standard deviation
Al	82.5	0.3	80.4	0.2
Ti	10.8	0.1	14.4	0.2
Cu	2.3	0.2	1.8	0.2
Fe	1.3	0.1	1.0	0.1
Mg	1.3	0.1	1.0	0.1
Ni	1.3	0.1	1.0	0.1
Si	0.6	0.1	0.4	0.1
	Spot 3		Area 4	
Al	80.5	0.2	92.0	0.2
Ti	13.6	0.2	2.9	0.1
Cu	2.0	0.2	1.8	0.2
Fe	1.1	0.1	1.0	0.1
Mg	1.1	0.1	1.1	0.1
Ni	1.2	0.1	1.1	0.1
Si	0.5	0.1	-	-

Table 10: EDS analysis of selected area and spot – section of the pre-alloyed powder.

Powders comparison

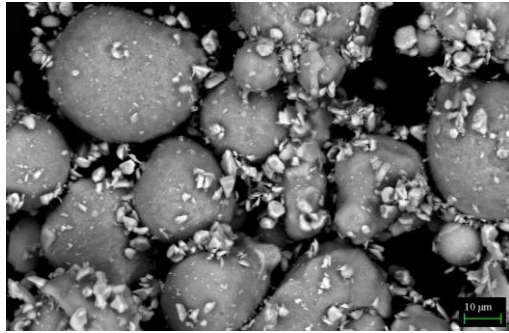
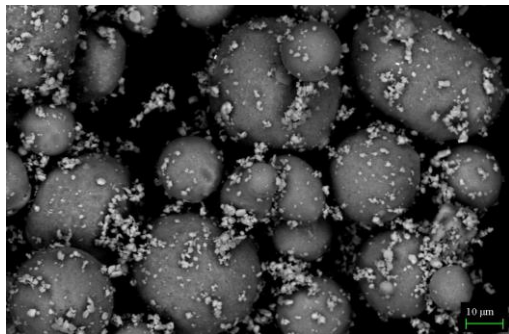
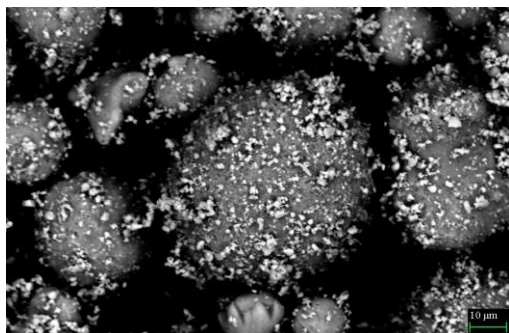
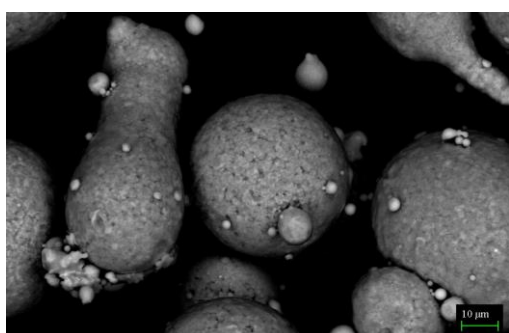
Powder	Images	Particle Size Dispersion [μm]	TiB ₂ average diameter [μm]	TiB ₂ content (% wt.)
Low energy mixing		D10=27.2 D50=49.8 D90=83.0	4	5.6
High energy mixing		D10=18.5 D50=39.8 D90=74.4	2	5.8
Plasma deposition		D10=19.85 D50=39.73 D90=71.03	2	7.4
Pre-alloying		D10=30.3 D50=44.8 D90=65.5	<1 (in-situ particles)	2.6

Table 11: Aluminium powder and reinforcements comparison.

In Table 11 a comparison between the four powder feedstocks is reported. For mechanical mixed and plasma produced feedstocks, TiB₂ average diameter values have been obtained from a graphical extrapolation starting from the smaller peak of PSD curves. An example of the procedure is shown in Figure 27. The first peak of the PSD curve (red curve) was considered to evaluate the borides dimension (in the example 4 μm).

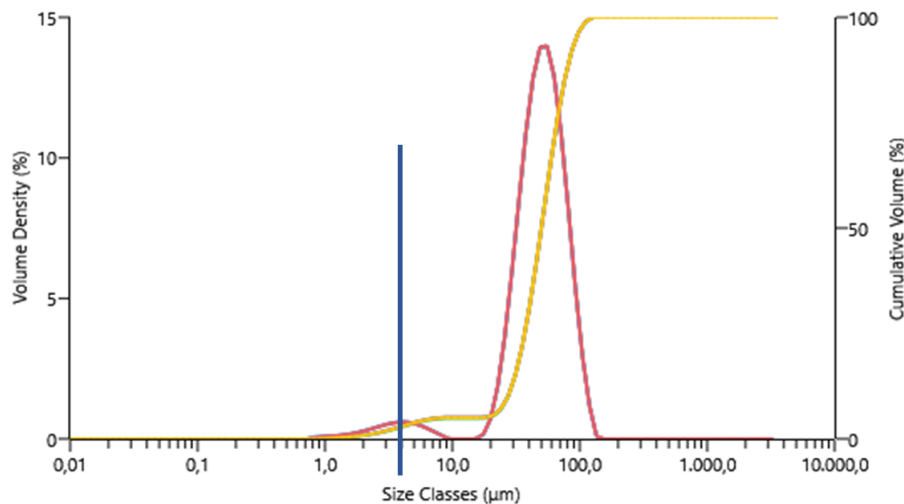


Figure 27: procedure of the graphical extrapolation used to evaluate TiB₂ dimensions.

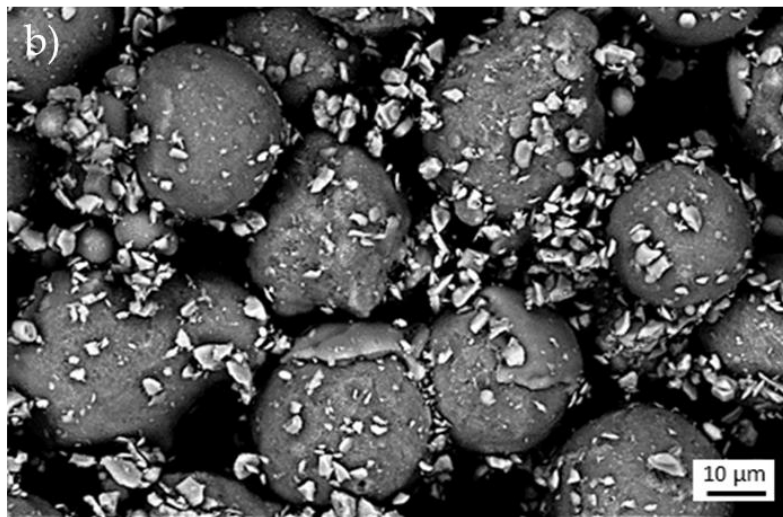
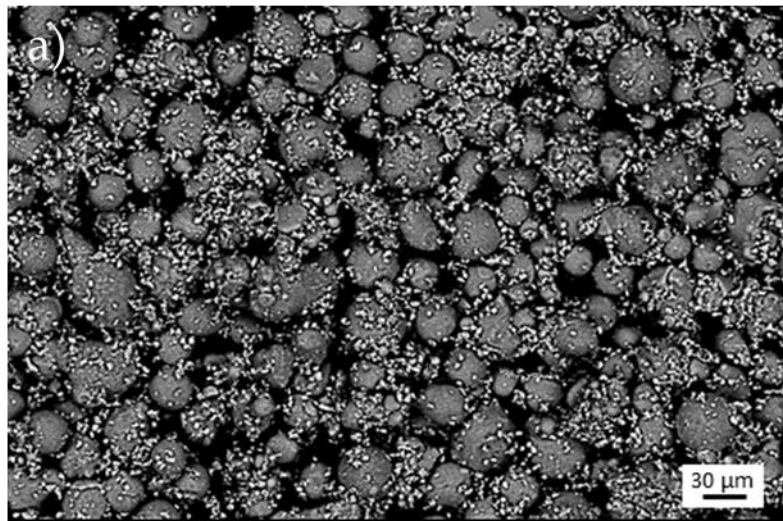
While for the pre-alloyed powder, TiB₂ dimensions were calculated using ImageJ software on SEM images.

4.1.2. Effect of sieving on particles dispersion

Sieve the residual powder from a LPBF procedure can be economically and environmentally useful since the unmelted powder particles can be collected and used for sequent productions. However, dealing with composite powder batches, sieving can lead to the detachment of the reinforcement particles from the aluminium powder surface. For this reason, the effect of sieving on the three powder feedstocks decorated with external TiB₂ particles (i.e., low and high energy mixing and plasma deposited feedstocks) was investigated using SEM images. Powder samples were collected and inspected before and after the sieving process.

The images of low energy mixing batch are shown in Figure 28. By comparing the pictures, it is possible to appreciate a reduction in the quantity of TiB₂ particles onto the surface of the Al powder particles after the sieving process. Such difference is attributed to the different density of the metal powder and ceramic particles, which

results in sedimentation due to vibrations induced by sieving, leading to inhomogeneity in the MMC powder feedstock.



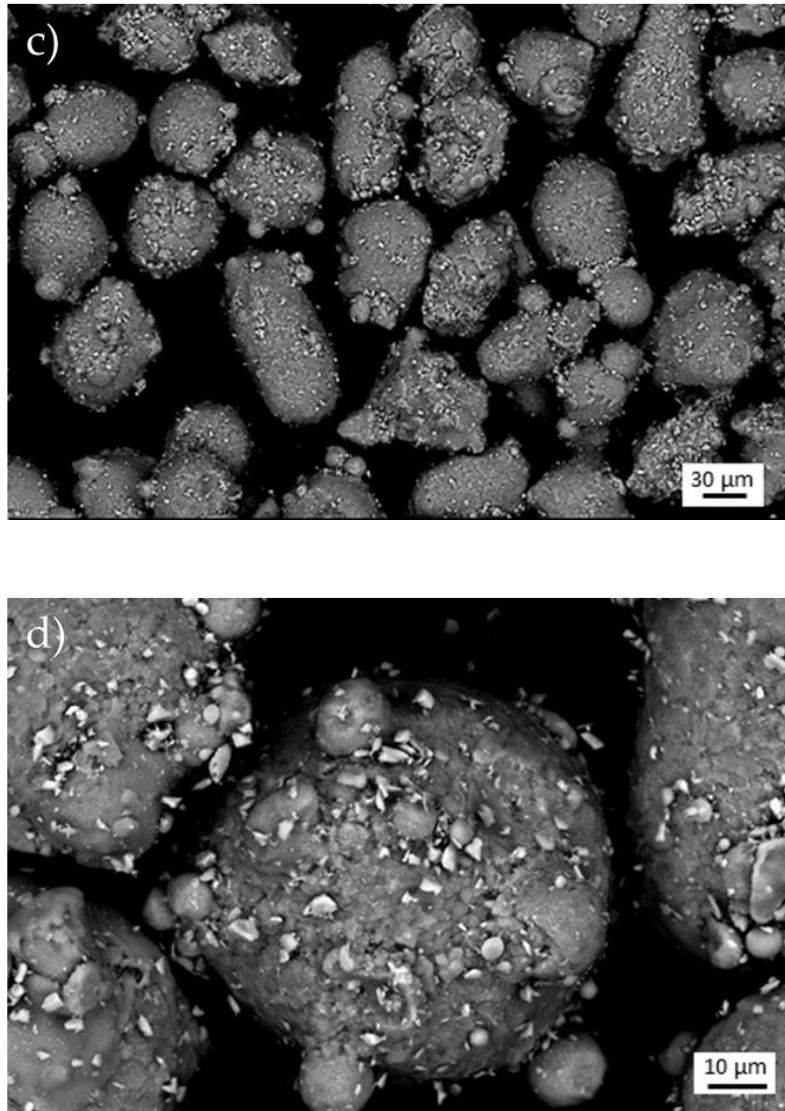


Figure 28: SEM images of the 2618+TiB₂ low energy mechanical mixing powder feedstock before (a, b) and after (c, d) sieving.

To quantify the changes in the TiB₂ amount during sieving, a XRD analysis was also performed on this feedstock. Diffraction patterns of the mixed and sieved powder were collected using a Rigaku SmartLab diffractometer and they are reported in Figure 29.

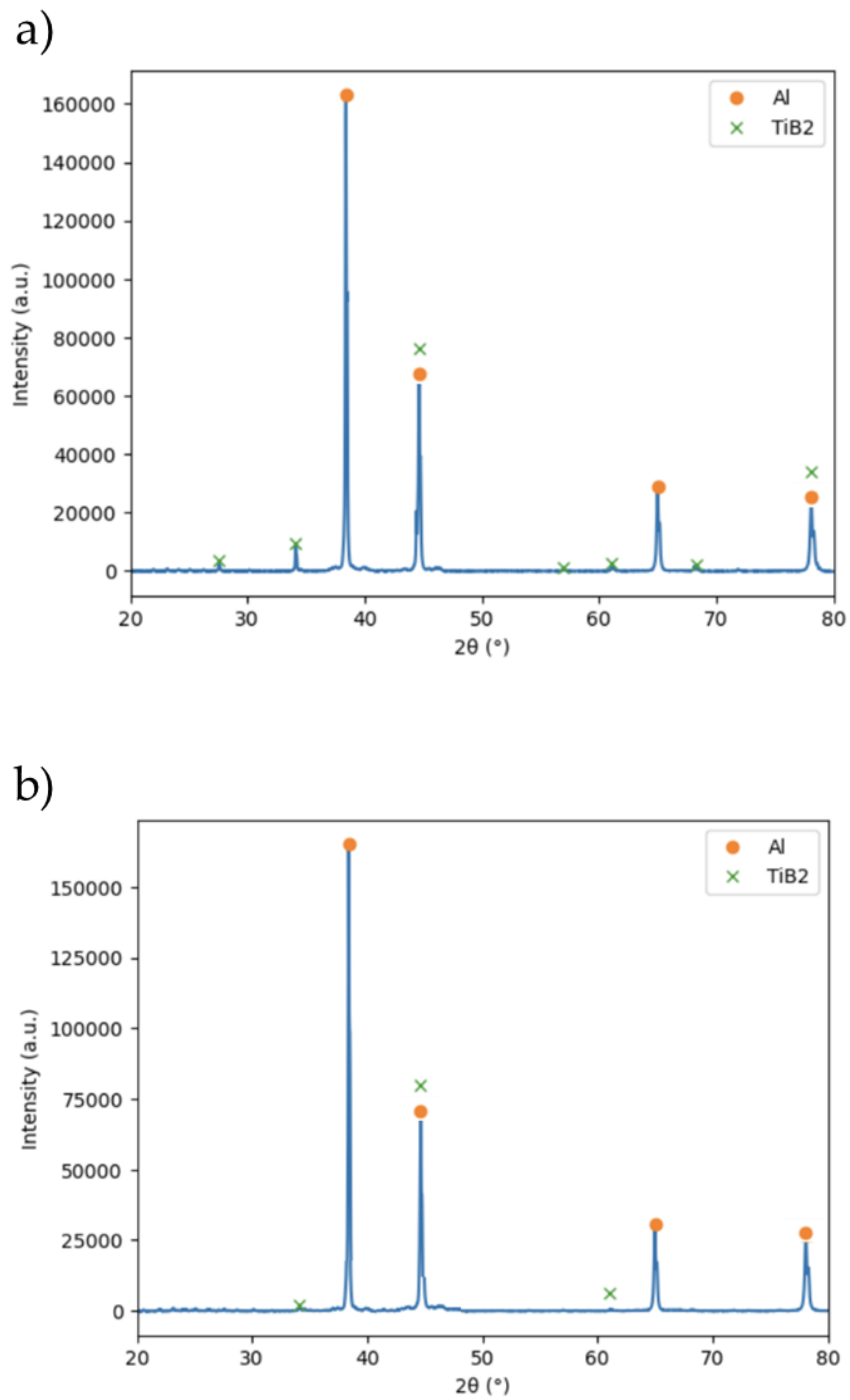


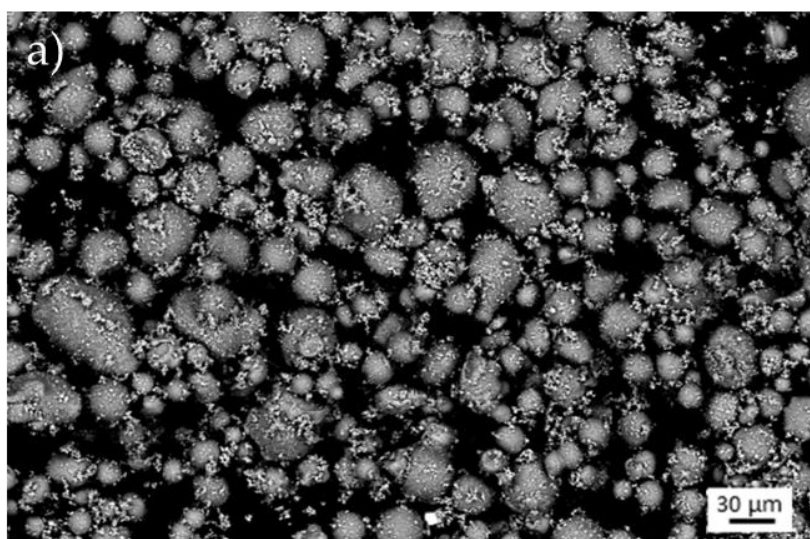
Figure 29: XRD pattern of 8h mixed powder before (a) and after sieving (b).

The results of both ImageJ and XRD analyses are reported in Table 12. The number of ceramic particles significantly decreased at end of the sieving process.

Low energy mixing feedstock	TiB ₂ (wt%) XRD	TiB ₂ (wt%) ImageJ
Before sieving	7.8 ± 0.2	7.6 ± 0.1
After sieving	2.1 ± 0.1	2.7 ± 0.1

Table 12: Concentrations of TiB₂ obtained from XRD patterns and by image analysis of the SEM picture.

As for low energy mixing batch, also plasma assisted deposition and high energy mixing powder feedstocks were collected and analysed using SEM before and after sieving. XRD analyses were not performed on these two batches since, as seen from the previous case, XRD and ImageJ results were in accordance, so, for simplicity, only ImageJ analyses were performed. Representative SEM images are shown in Figure 30 and Figure 31.



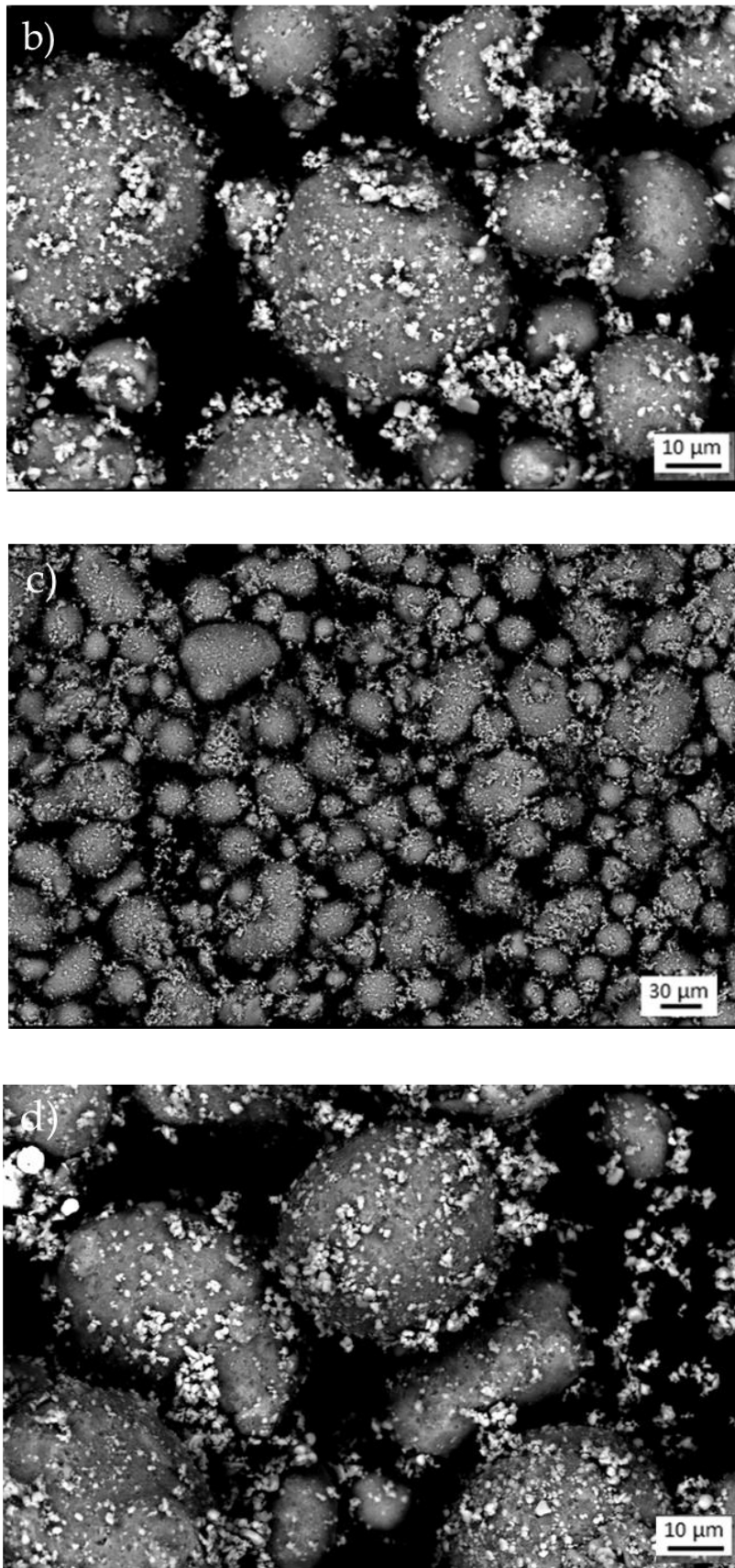
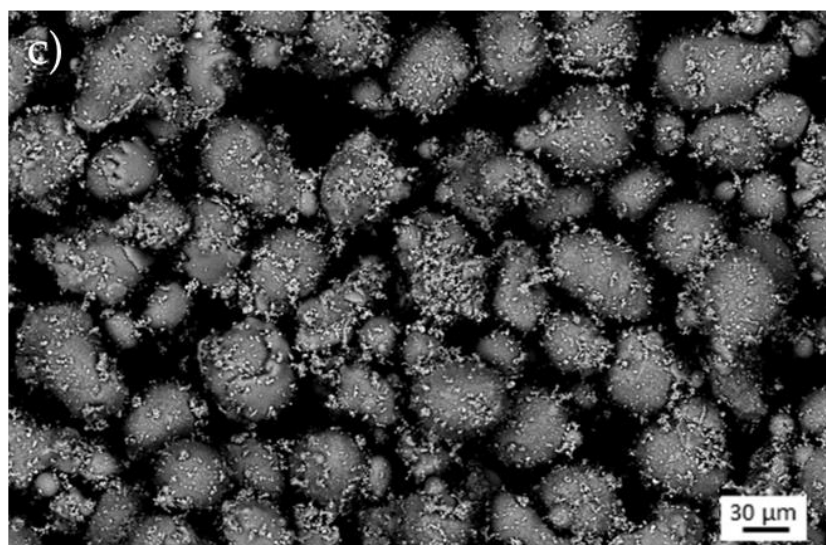
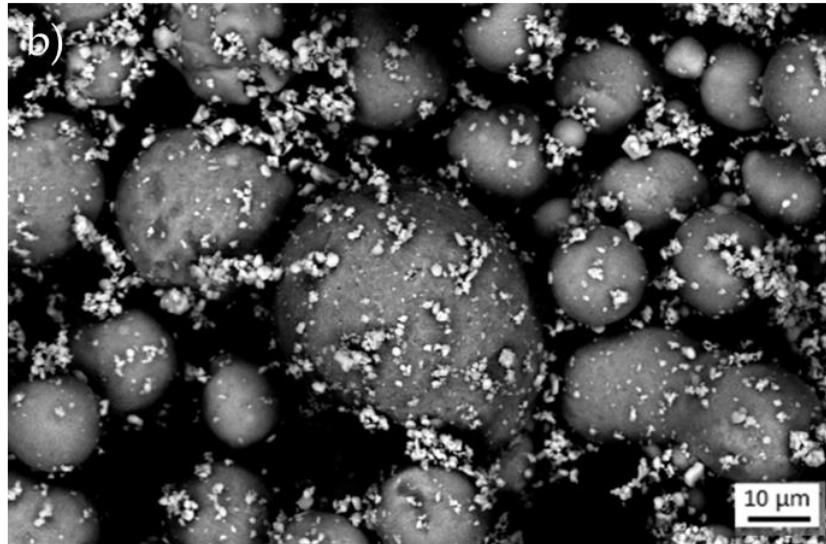
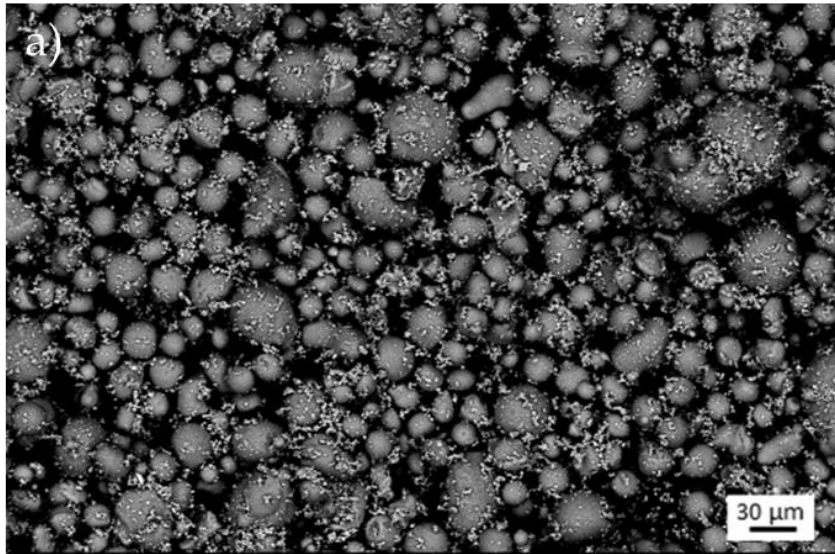


Figure 30: SEM images of the plasma deposition powder feedstock before (a, b) and after (c, d) the sieving process.



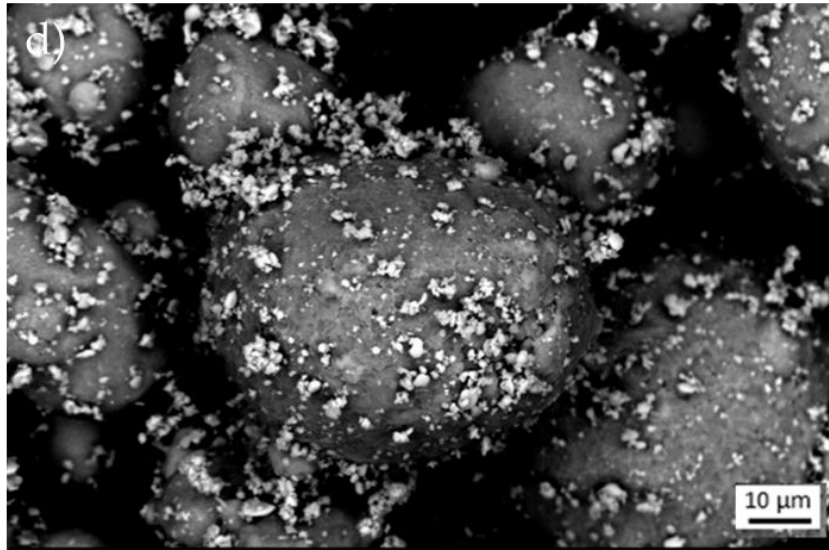


Figure 31: SEM images of the high energy mixing powder feedstock before (a, b) and after (c, d) the sieving process.

Results achieved by ImageJ analyses on SEM pictures are showed in Table 13.

	TiB ₂ (wt%) plasma deposition	TiB ₂ (wt%) high energy mechanical mixing
Before sieving	6.3 ± 0.5	6.0 ± 0.7
After sieving	6.9 ± 0.8	6.8 ± 1.0

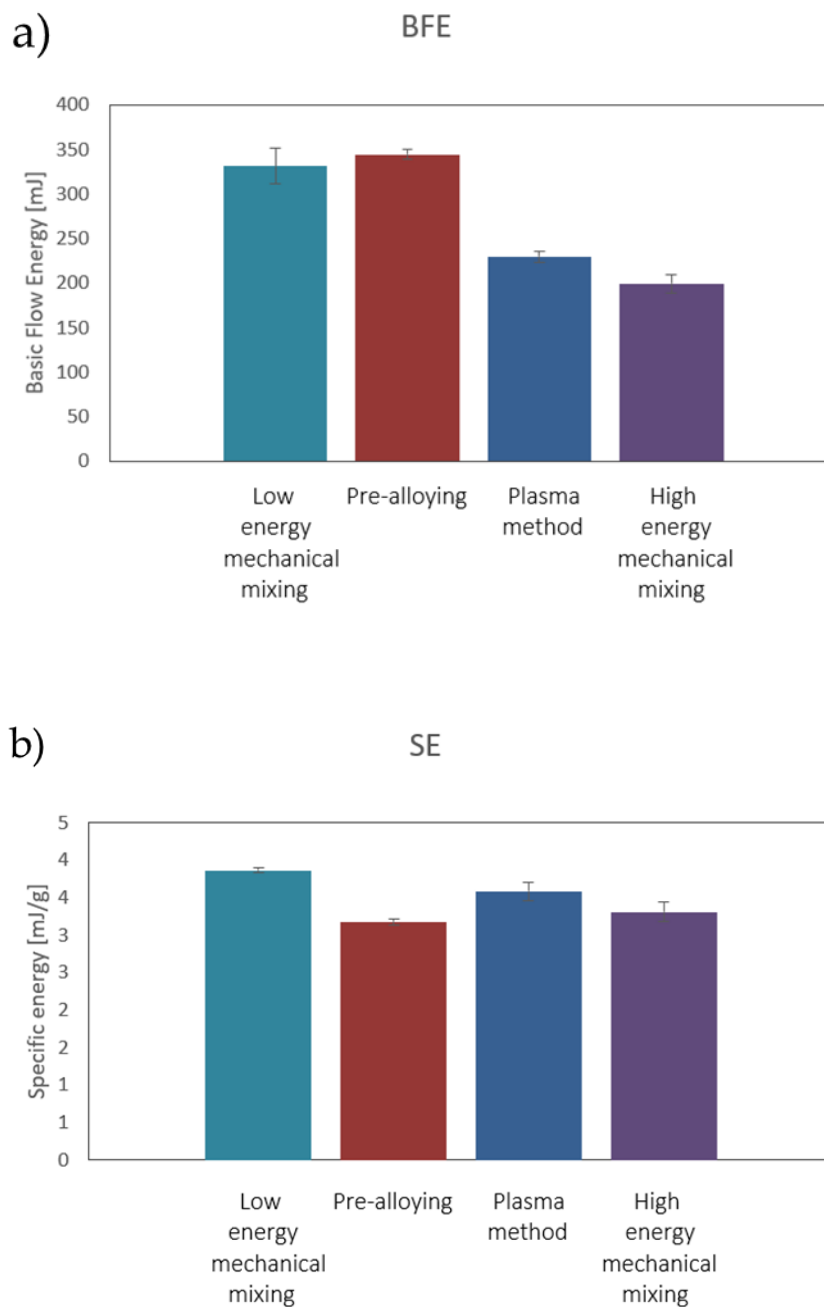
Table 13: Concentrations of TiB₂ obtained by image analyses of SEM pictures of plasma deposition and high energy mixing batches.

From a first visual inspection of the SEM pictures and from the results previously showed in Table 13, it is possible to assert that the sieving process does not affect significantly the amount of particles attached to the powder surface for the plasma deposition and the high energy mixed feedstocks. As a result, they can be reused without the need to re-process the powder by plasma deposition or mechanical mixing, respectively. On the other hand, low energy mixing feedstock should be re-mixed to ensure a homogeneous dispersion of the reinforcement particles after sieving.

4.1.3. Powder flowability tests

A good powder flowability is fundamental to avoid any problems during the powder spreading phase of LPBF procedure, like the formation of powder clusters or an incomplete powder spreading that can lead to an incomplete bulk product formation.

As a result, flowability analyses were performed on the four feedstocks and three different indexes – e.g., basic flowability energy (BFE), specific energy (SE) and conditioned bulk density (CBD) – were collected. To ensure a good flowability of the feedstock, BFE and SE indexes should be minimized, while CBD index should be the highest possible [37]–[39]. The measured values (BFE, SE, and CBD) for the four feedstocks are showed in Figure 32.



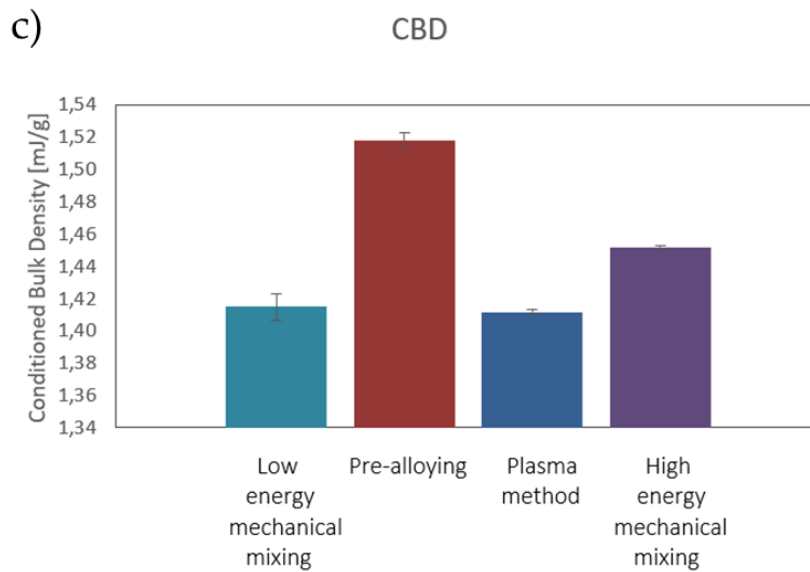


Figure 32: flowability indexes, respectively BFE (a), SE (b), CBD (c).

Considering SE and CBD indexes, the pre-alloyed powder appears to be the feedstock with better flow properties, immediately followed by the high energy mechanical mixed powder. However, pre-alloyed powder showed the highest BFE index, that means a poor flowability. A possible explanation is that there is an extensive flowing zone around the blade in which shearing occurs. This is due to the low compressibility of the powder and the high transmissibility of forces from particle to particle. Regarding the effect of external TiB_2 , the presence of tiny spherical particles on the surface of larger metallic particles is likely to increase the friction coefficient, generating a resisting force opposed to the sliding and shearing of adjacent particles. As a consequence, the BFE index was lower for powder feedstocks produced with high energy mechanical mixing and plasma deposition.

To conclude, according to the BFE, SE and CBD results, the powder with the best flowability is the pre-alloyed one. Among the powder feedstocks with external TiB_2 particles, the high energy mechanical mixed one showed the best flow properties.

4.2. Bulk analysis

For each powder feedstock, nine cubes with dimensions of $8 \times 8 \times 8 \text{ mm}^3$ were printed with Renishaw AM250, each of them characterised by different parameters, in order to find the best scanning conditions to obtain the highest density. The printing parameters are reported in Table 3 and Table 4 of Section 3.2.1 - LPBF sample production.

4.2.1. Porosity

The amount of void volume in a solid substance is known as porosity and it is expressed as a percentage of the volume of voids with respect to the total volume of the component. High density, so a low porosity level, is a fundamental material requirement to exhibits better tensile properties since cavities can act as cracks nucleation sites. In Table 14 the porosity values are reported for each cubic sample of the four powder batches. Such values have been calculated using the software ImageJ on Light Optical Microscope images as the fraction between the sum of voids areas and the overall area of the sample section (as described in the section 3.2.2 – Optical microscope and ImageJ).

Sample	Porosity percentage (%)			
	Low energy mechanical mixing	High energy mechanical mixing	Plasma deposition	Pre-alloying
A	0.43 ± 0.14	0.23 ± 0.08	0.64 ± 0.19	0.66 ± 0.16
B	0.19 ± 0.04	0.48 ± 0.27	0.89 ± 0.14	0.55 ± 0.24
C	0.32 ± 0.07	0.50 ± 0.01	0.28 ± 0.16	0.39 ± 0.11
D	0.46 ± 0.09	0.12 ± 0.02	0.14 ± 0.05	0.51 ± 0.10
E	0.68 ± 0.28	0.30 ± 0.03	0.17 ± 0.11	0.55 ± 0.10
F	0.77 ± 0.28	0.96 ± 0.21	0.93 ± 0.49	0.54 ± 0.18
G	0.78 ± 0.11	0.68 ± 0.23	0.08 ± 0.03	0.34 ± 0.06
H	0.64 ± 0.18	0.16 ± 0.04	0.29 ± 0.08	0.36 ± 0.09
I	0.67 ± 0.16	0.11 ± 0.03	0.19 ± 0.04	1.03 ± 0.19

Table 14: Bulk samples porosity analysis.

Considering the values reported in Table 14, it is not possible to establish a solid relationship between printing parameters and porosity. The relative density levels are always higher than 99%; the maximum values were between 99.66 and 99.92 % for the four types of MMCs.

In the following figures, representative LOM images of the bulk samples are reported for each powder feedstock condition (Figure 33 to Figure 36). Samples were etched with Keller's reagent to reveal the typical fish-scale microstructure of LPBF processed materials [41].

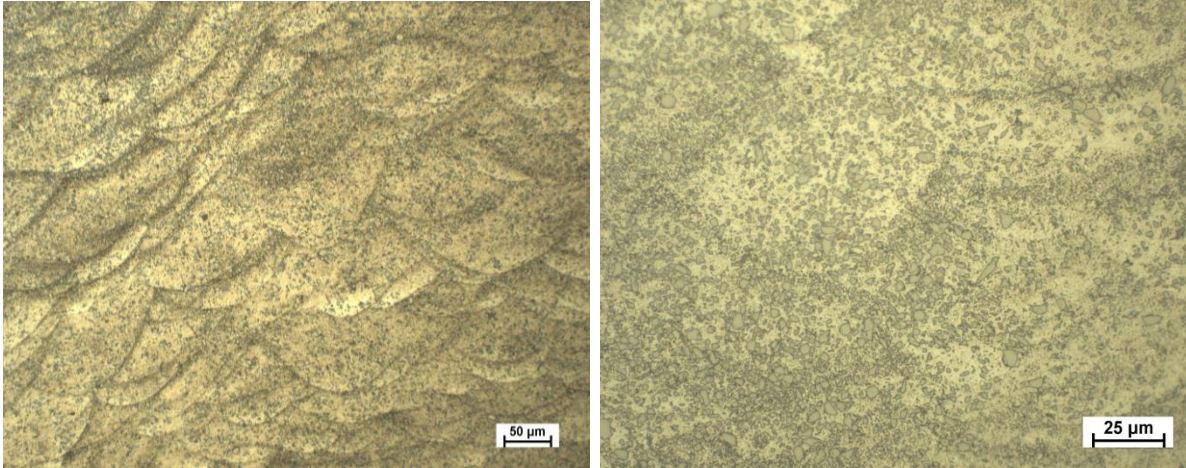


Figure 33: low energy mechanical mixing bulk samples.

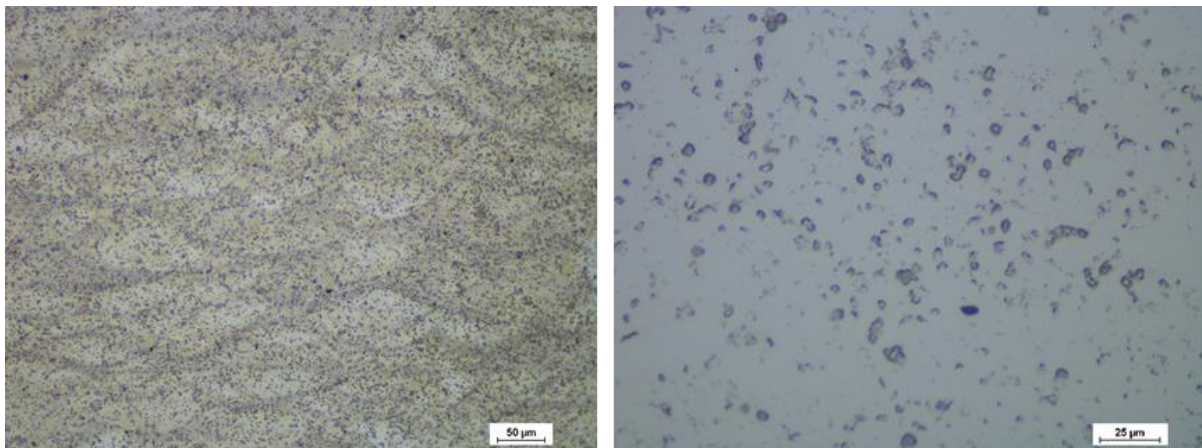


Figure 34: high energy mechanical mixing bulk samples.

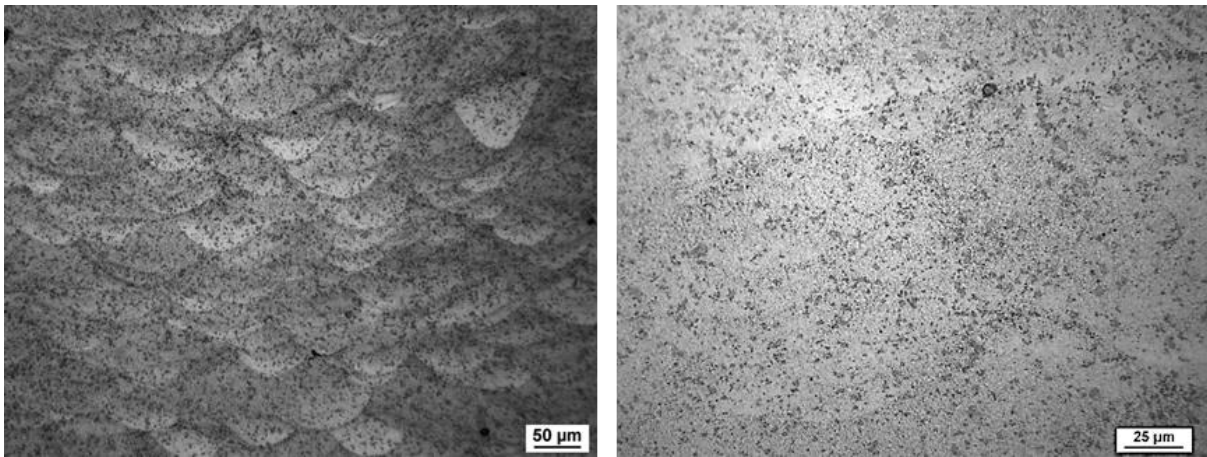


Figure 35: plasma deposition bulk samples.

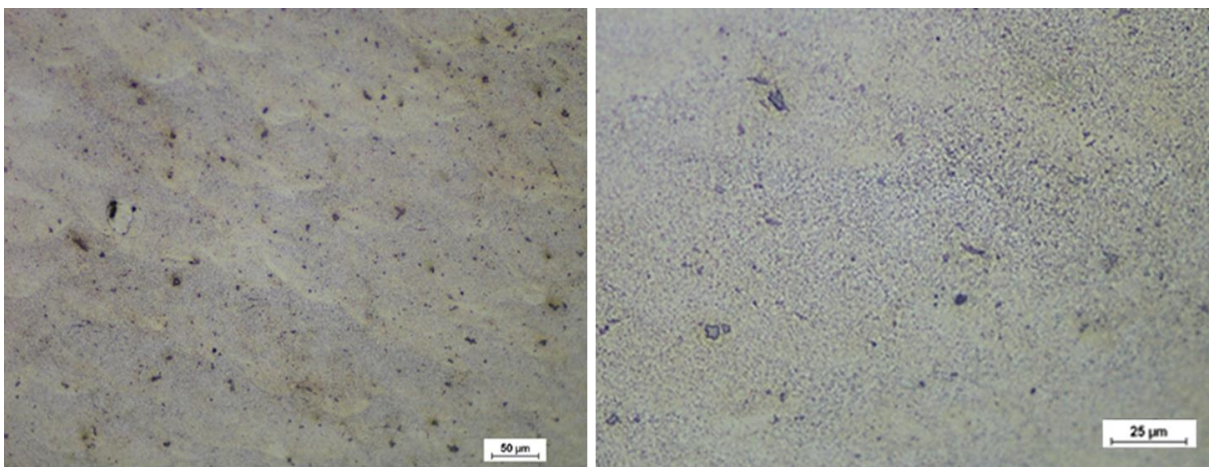


Figure 36: pre-alloying bulk samples.

In the picture it is possible to appreciate the low porosity levels and the homogeneous distribution of the TiB_2 particles. For this reason, it can be stated that the scanning parameters choice was correct in order to melt all the solid powder. A more detailed description of reinforcements distribution follows in the next section.

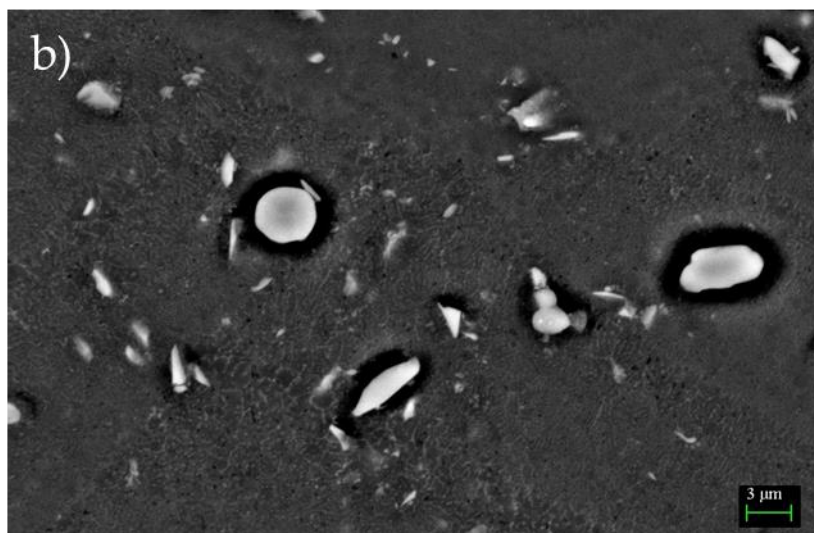
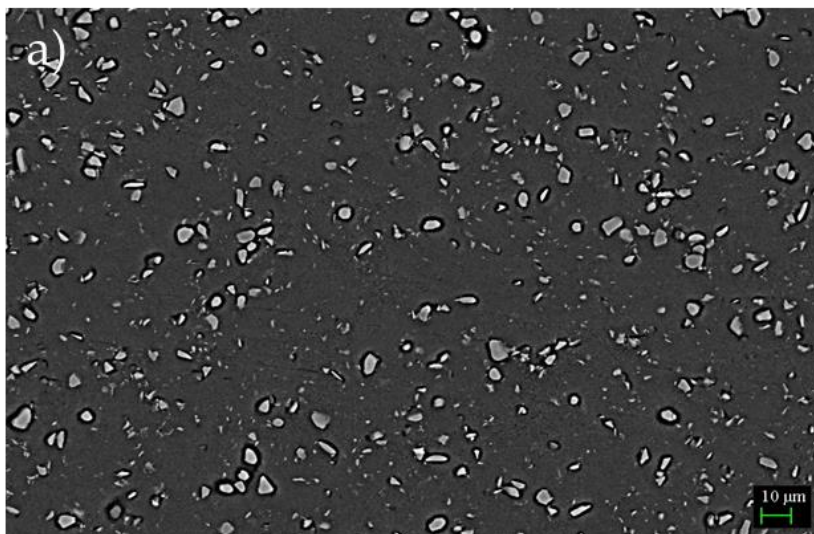
Furthermore, from the above reported LOM images, it is possible to see that the presence of the TiB_2 particles avoided the formation of hot cracks, which instead are generally present in LPBF printed standard Al 2618 alloy [42]. Solidification cracks are mainly formed during final stages of solidification, when the thermal shrinkage promotes the build-up of tensile stresses in the semi-solid alloy. As the alloy tensile strength is overcome, the nucleation and consequent propagation of cracks along grain boundaries occur. However, TiB_2 present in the melt pools acted as heterogeneous nucleation sites for α -Al grains. The resulting fine equiaxed grain structures were able to accommodate higher shrinkage stresses and to prevent crack formation [43].

4.2.2. TiB_2 distribution in bulk samples

A homogeneous reinforcement particle distribution is essential to obtain a final material with high and isotropic mechanical properties. In order to verify the spatial dispersion of borides and their quantity, analyses have been performed on bulk sample SEM images reported below. For each powder typologies, the percentage and average size of TiB_2 particles are calculated using ImageJ software.

Low energy mechanical mixing powder

In Figure 37 are reported the SEM images of bulk samples obtained from the low energy mechanical mixing powder batch.



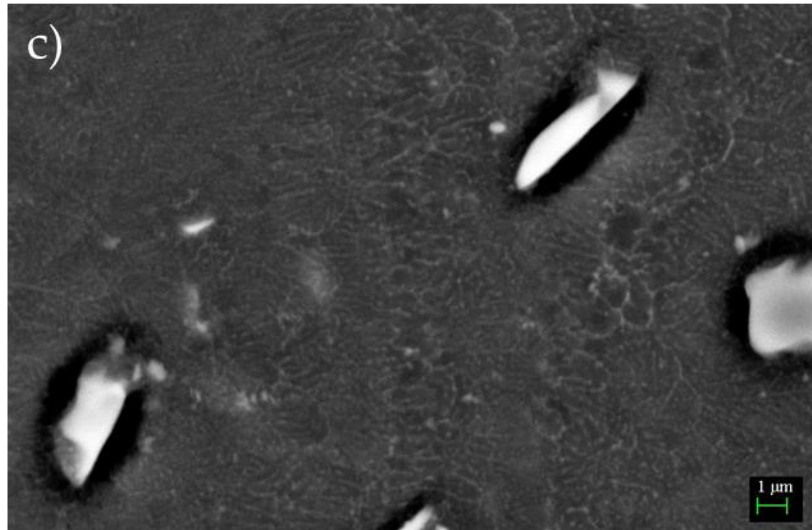


Figure 37: SEM photos of low energy mechanical mixing bulk sample (sample B).

TiB ₂ percentage [%]	7.1 ± 0.9
TiB ₂ average dimension [μm]	1.8 ± 0.3

Table 15: percentage and dimension of reinforcement in bulk sample.

In the images it is possible to observe the bright-contrast reinforcement particles among the Al 2618 matrix: they are homogeneously dispersed. The average dimensions of the borides in the bulk samples, reported in Table 15, are slightly smaller if compared to those of the original borides present in the powder batch. However, it is important to underline that the boride dimensions in bulk samples are measured when the samples are cut along a plane perpendicular to the scanning direction. As a result, the effective measures reported are an evaluation of the borides section, not the of whole particle. In addition, Table 15 shows that the reinforcements average percentage is $7.1 \pm 0.9\%$, which is in accordance with the requested TiB₂ concentration. However, also in this case, the borides content is an area fraction evaluated on sample section surface. Therefore, the results can be slightly different from the actual volume or weight TiB₂ concentration.

High energy mechanical mixing powder

Figure 38 shows the borides distribution in high energy mechanical mixing bulk samples. It is possible to appreciate how the reinforcement distribution is homogeneous without following a preferential texture.

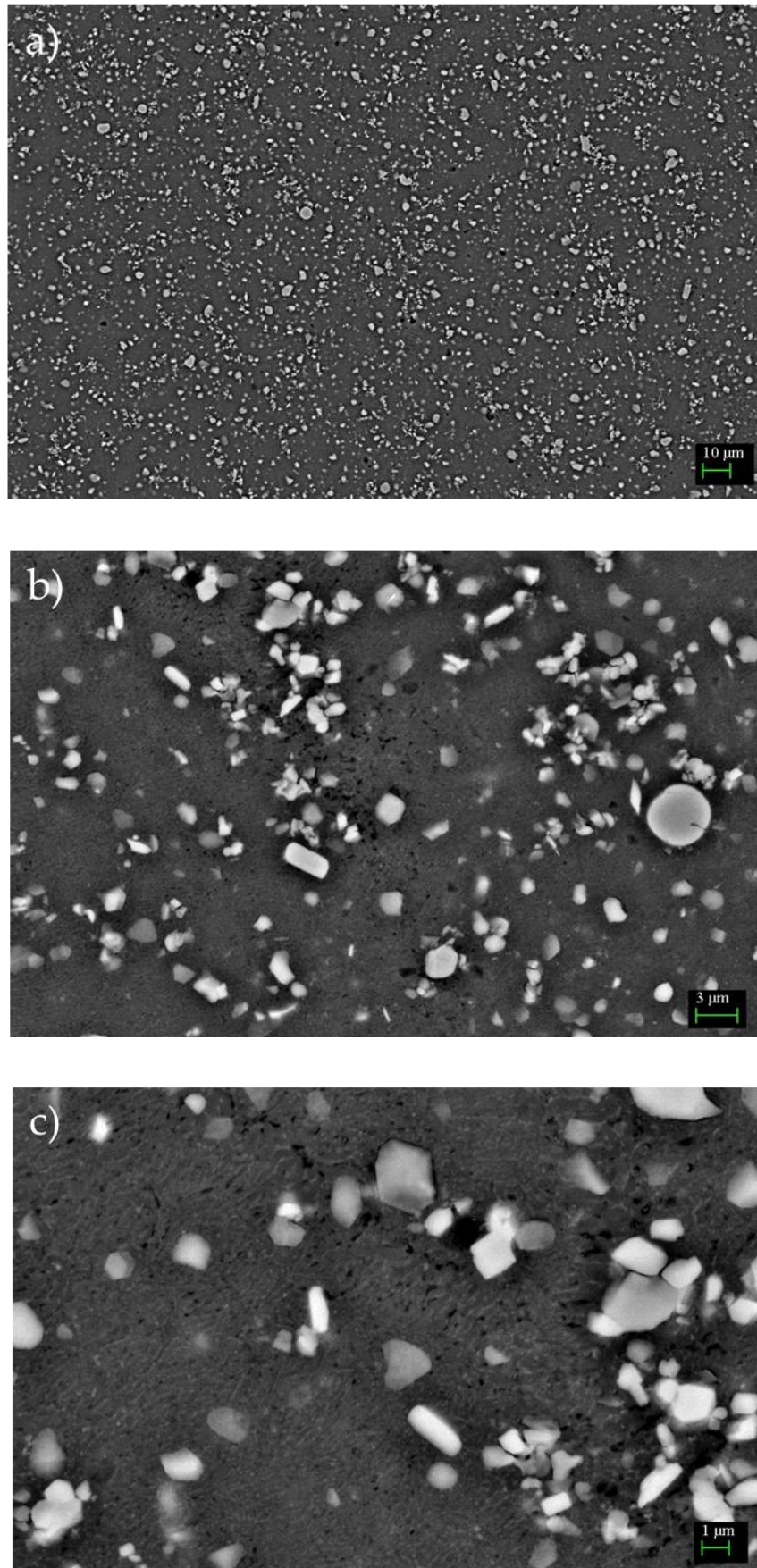


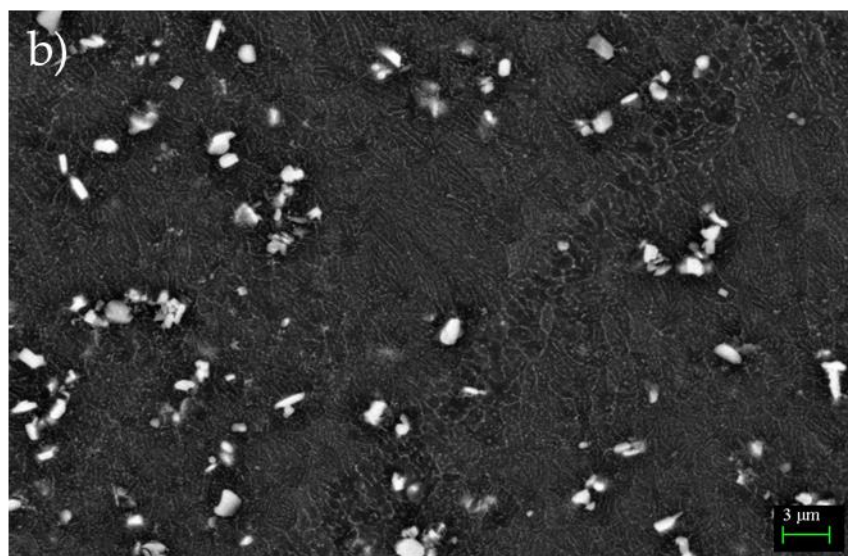
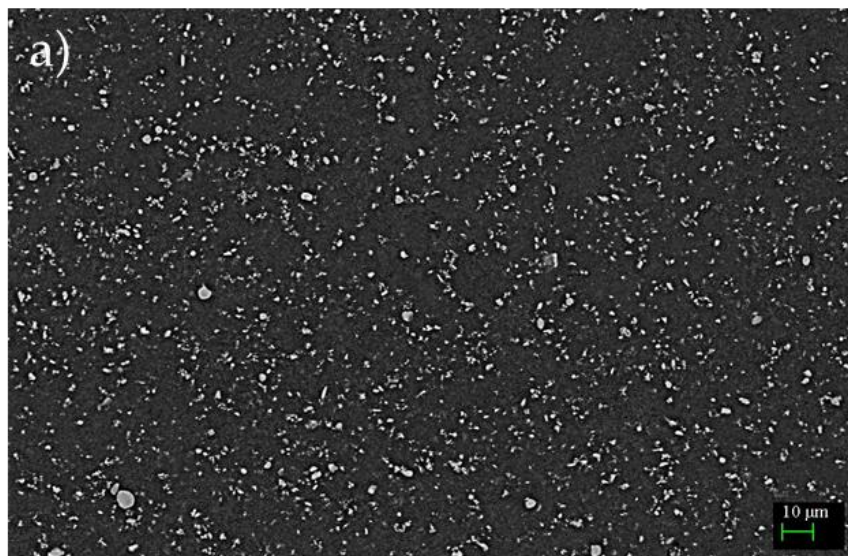
Figure 38: SEM photos of high energy mechanical mixing bulk sample (sample B).

TiB ₂ percentage [%]	6.8 ± 2.8
TiB ₂ average dimension [μm]	1.0 ± 0.1

Table 16: percentage and dimension of reinforcement in bulk sample.

Table 16 shows a reinforcement percentage quite similar to the previous feedstock case. Borides average dimensions, instead, are smaller than those of the low energy mixed samples, a result that is consistent with the dimensions of borides particles evaluated in the powder analysis (section 4.1.1 - SEM and chemical analysis).

Plasma assisted deposition powder



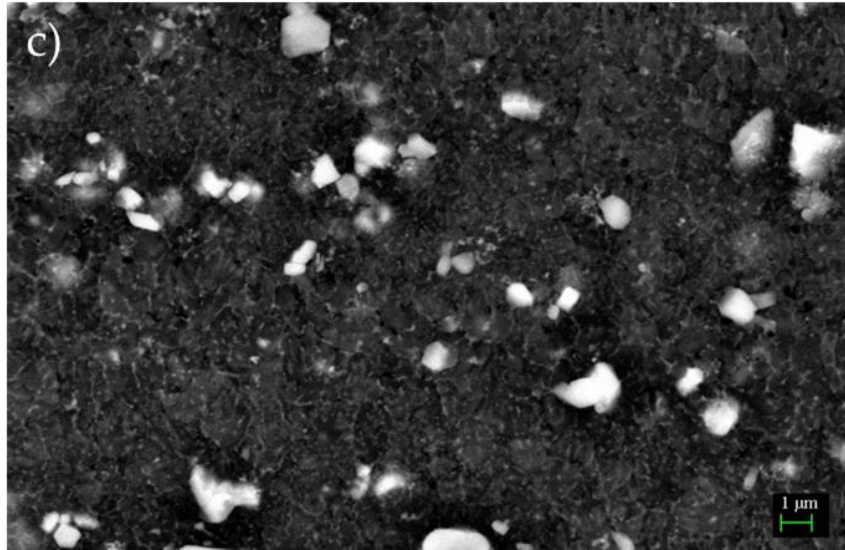


Figure 39: SEM photos of plasma deposition bulk sample (sample B).

TiB ₂ percentage [%]	5.9 ± 0.4
TiB ₂ average dimension [μm]	0.8 ± 0.02

Table 17: percentage and dimension of reinforcement in bulk sample.

Figure 39 and Table 17 show that for the samples obtained from the plasma assisted deposition feedstock there is a further reduction in reinforcements percentage and in their average dimension. Nevertheless, this feedstock was the only one with a satisfying TiB₂ concentration inside the powder batch. However, the considerations made regarding the two previous samples analysed are still valid. The borides percentage reported above is not an actual volume or weight concentration, but it is evaluated considering just a section of the bulk sample. For this reason, the values in the table must not be considered as an indication of the whole bulk material properties.

Pre-alloying powder

In Figure 400 SEM images of bulk samples obtained from the pre-alloyed powder are reported.

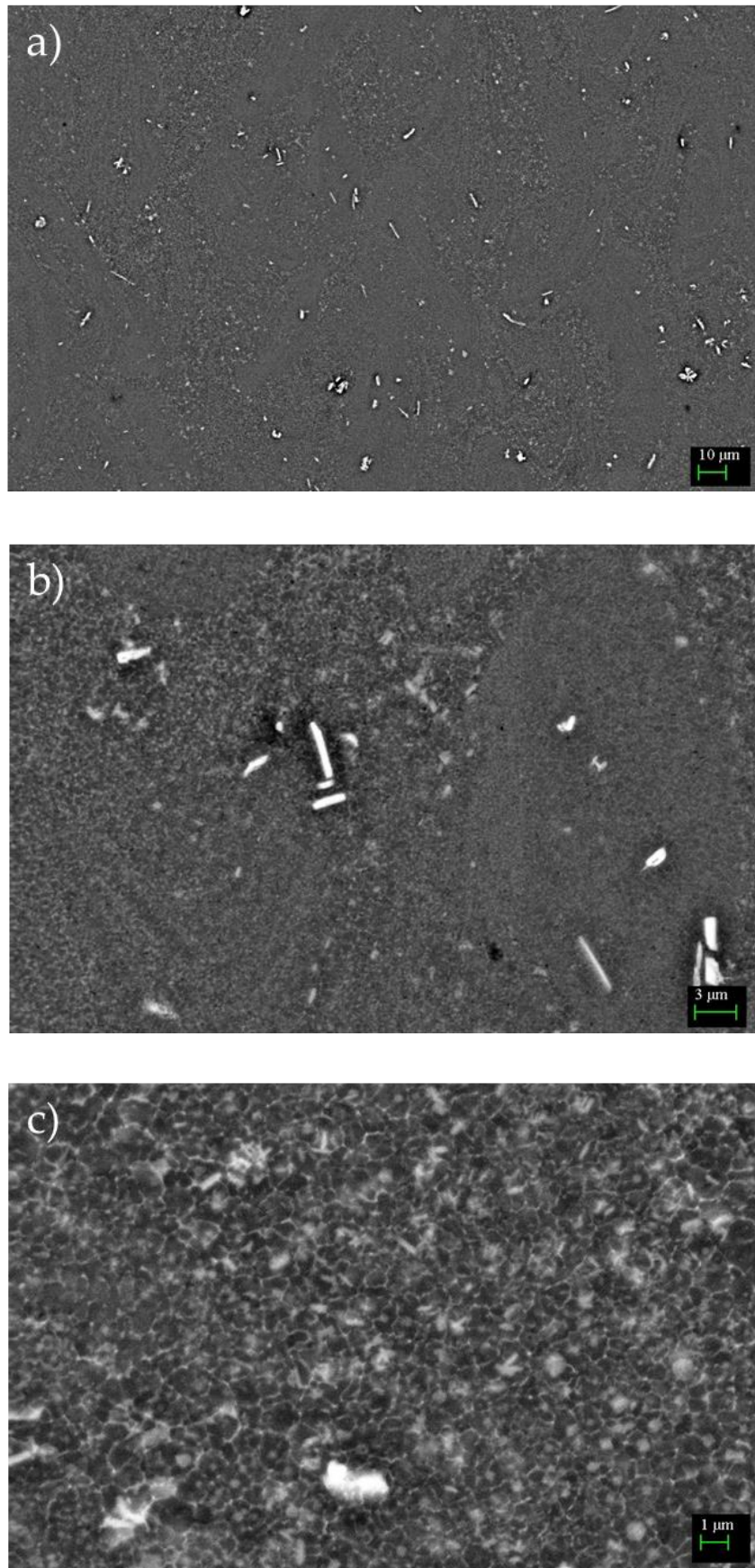


Figure 40: SEM photos of pre-alloyed bulk sample (sample B).

TiB ₂ percentage [%]	0.87 ± 0.17
TiB ₂ average dimension [μm]	0.36 ± 0.3

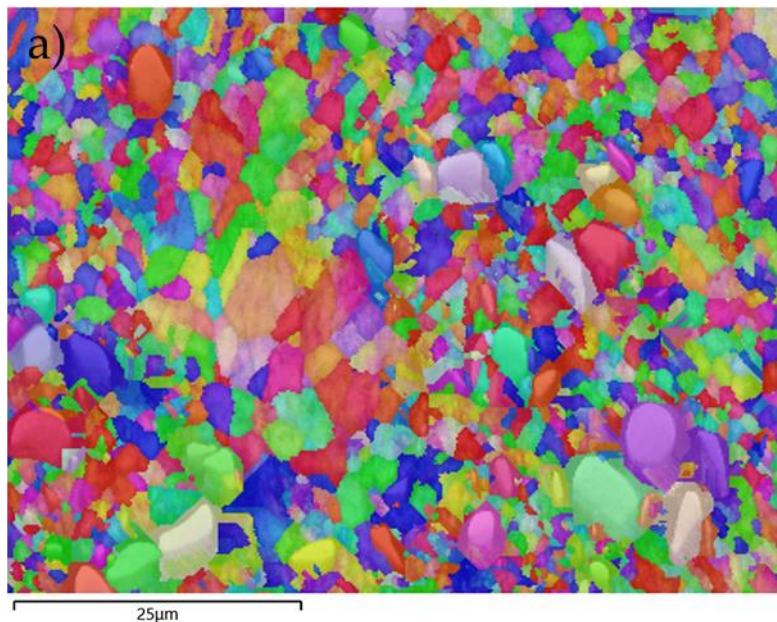
Table 18: percentage and dimension of reinforcement in bulk sample.

The TiB₂ percentage and dimension have been reported in Table 18. In this case, reinforcements particles are very small and rare if compared to previous samples, which makes difficult to detect the borides also at high magnification. Moreover, the target amount of Ti and B concentration in the feedstock was not achieved by the supplier, so not many borides had the possibility to form during the gas atomization process. However, submicrometric reinforcements are beneficial since they provide better strengthening effect than bigger particles.

4.2.3. Grain morphology

Electron Backscatter Diffraction maps (EBSD) and phase maps have been used to investigate on the grains structure of the bulk samples, in particular their size and orientation. Inverse Polar Figure (IPF) and Phase maps are reported from Figure 41 to Figure 44.

Low energy mechanical mixing powder



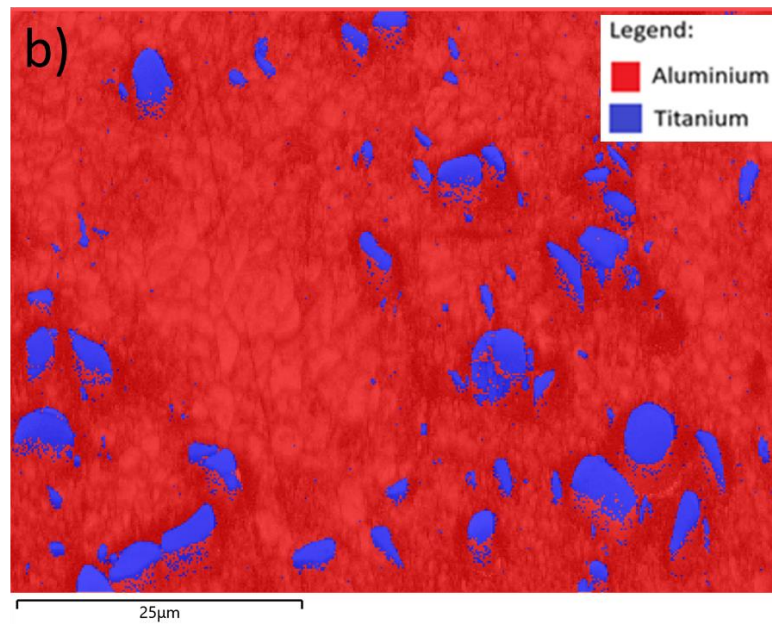


Figure 41: IPF map (a) and phase map (b) of low energy mixing sample (sample B).

Average grain area [μm^2]	2.3
Average grain diameter [μm]	1.5

Table 19: Average grain area and diameter in bulk sample.

From the IPF reported in Figure 41(a) it is possible to observe the different crystallographic orientation of each grain. In particular, each colour represents a certain orientation, clearly showing that no preferential grain orientation is present. TiB_2 particles were able to stimulate heterogeneous nucleation of the primary $\alpha\text{-Al}$ phase, leading to a fine equiaxed grain structure [43]. The resulting structure was able to accommodate higher shrinkage stresses generated during final stages of the solidification and to prevent crack nucleation and propagation along grain boundaries. The reinforcement dispersion acted as a hot cracks suppressor.

This type of powder led to the biggest average grain diameter, if compared with the other three powder feedstocks that are presented in the next sections.

In Figure 41(b) the phase map is reported. In particular, TiB_2 particles are represented in blue, while the Aluminium matrix is depicted in red. The phase map allows to evaluate the reinforcements size. In the case of low energy mechanical mixing feedstock, borides diameter in bulk sample has been discovered to be the highest within the four bulk samples analysed (as reported in section 4.2.2 – TiB_2 distribution in bulk samples).

High energy mechanical mixing powder

In Figure 42 the IPF map and the phase map of the bulk sample obtained from high energy mixing feedstock are reported.

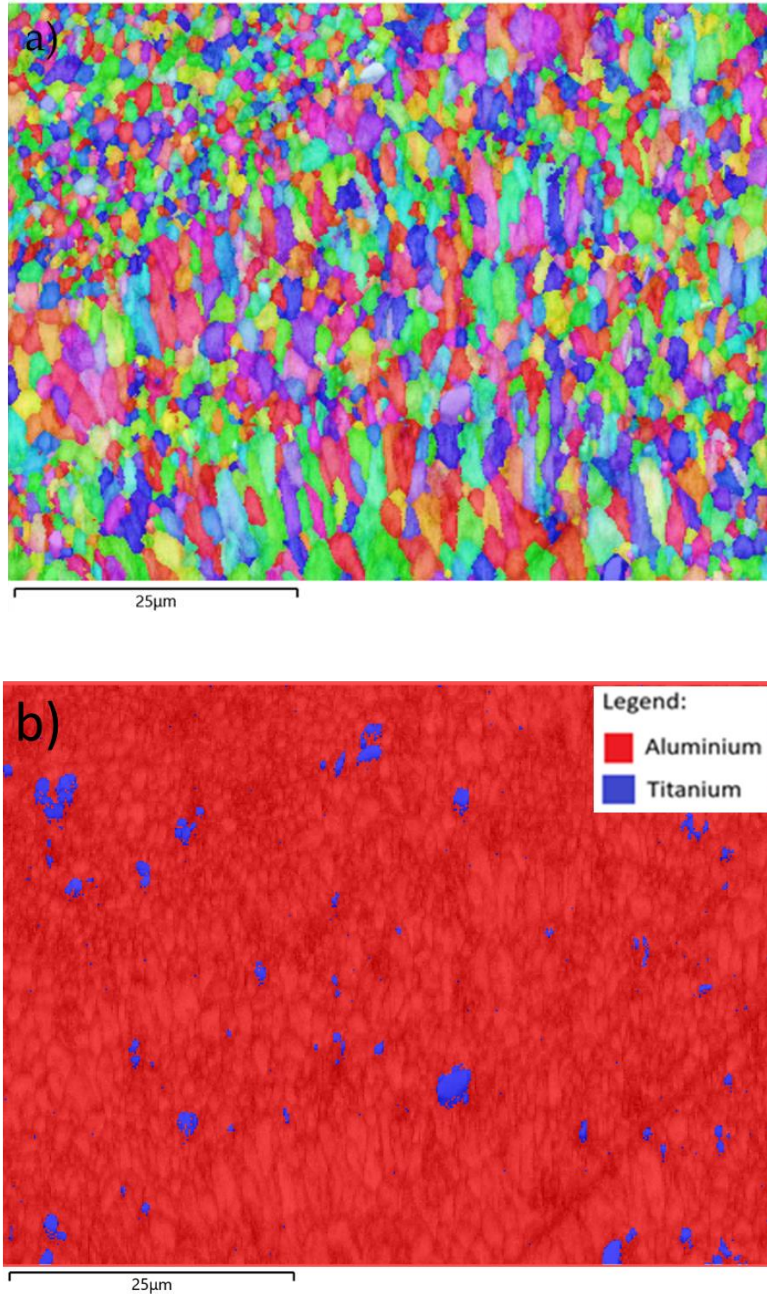


Figure 42: IPF map (a) and phase map (b) of high energy mixing sample (sample B).

Average grain area [μm^2]	1.6
Average grain diameter [μm]	1.3

Table 20: Average grain area and diameter in bulk sample.

Similar consideration can be made regarding IPF diagram and TiB_2 phase map with respect to the previous powder batch. The only differences are the average size of the grains, showed in Table 20, and of the reinforcement particles, which are smaller (1.3 vs 1.5 μm). Consistently, low and high mixing feedstock bulk samples have very similar borides contents, but in the latter case, the dimension of the reinforcement in the initial powder is smaller. As a result, a finer grain structure is obtained in the high energy mixed sample.

Plasma assisted deposition powder

Figure 43 shows the IPF map and the TiB_2 phase map of the bulk sample obtained from the plasma deposition powder feedstock.

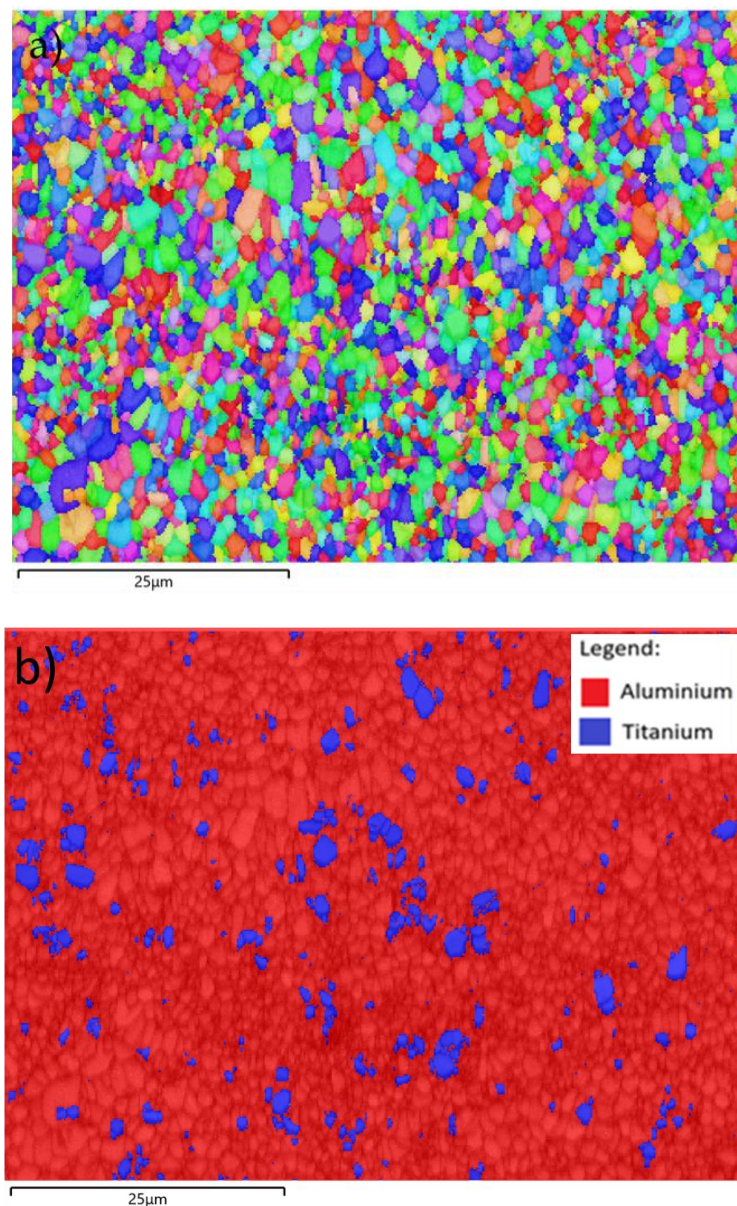


Figure 43: IPF map (a) and phase map (b) of plasma deposition sample (sample B).

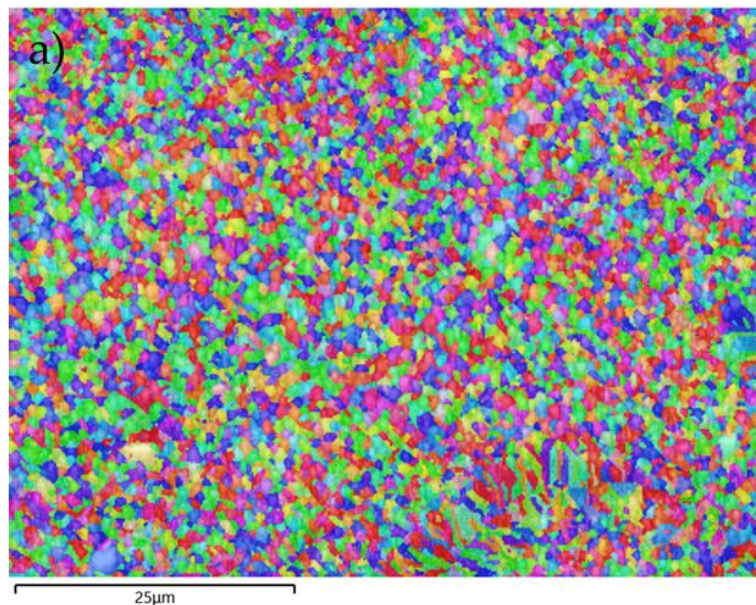
Average grain area [μm^2]	1.1
Average grain diameter [μm]	1.1

Table 21: Average grain area and diameter in bulk sample.

From Figure 43 it is possible to appreciate the random orientation of the grains and their equiaxiality. Grain size, as reported in Table 21, is lower with respect to the two previous feedstocks analysed. In particular, between the three powder batches characterised by external reinforcing particles (low and high energy mechanical mixed and plasma assisted deposition feedstocks) only the plasma deposited one was able to reach the TiB_2 target composition. For this reason, more borides were present in the melt pools of this powder. Since reinforcements act as heterogeneous nucleation sites during metal solidification, a finer grain microstructure was found in the bulk material.

Pre-alloyed powder

Figure 44 shows IPF map and phase map of the printed pre-alloyed powder.



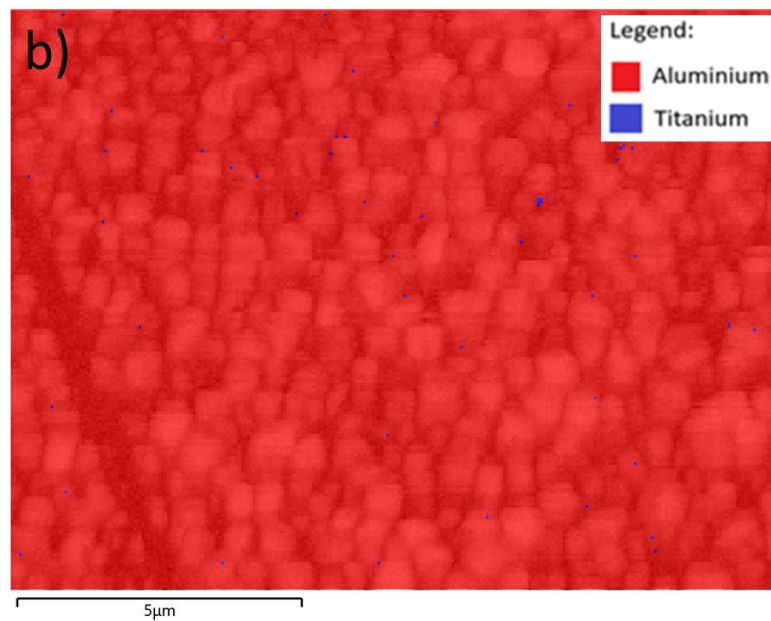


Figure 44: IPF map (a) and phase map (b) of pre-alloying sample (sample B).

Average grain area [μm^2]	0.6
Average grain diameter [μm]	0.8

Table 22: Average grain area and diameter in bulk sample.

Considering the pre-alloyed powder, the lowest TiB_2 content was achieved due to technical limits related to gas atomization process. In particular, high concentrations of B and Ti can lead to the formation of solid borides during the atomization process, that have the tendency to separate from the liquid. As a result, this sedimentation can determine also nozzle clogging.

However, as reported in Table 22, in the bulk sample the smallest grain size has been found if compared with the other three feedstocks analysed. This is a direct consequence of the sub-micrometric reinforcements present inside pre-alloyed powder particles. Indeed, gas-atomized batch showed the smallest TiB_2 average diameter between the four feedstocks considered, as reported in Table 11. Moreover, this type of powder is rich in Titanium, which has a double function: the first one is to react with Boron to form TiB_2 particles, the second is to enhance the formation of Al_3Ti intermetallic. This latter compound has the ability to refine α -Aluminium grains, since during the solidification of the alloy Al_3Ti particles are formed and they act as heterogeneous nucleation sites for new grains [43], [44]. Consequently, grains resulted refined.

4.2.4. Bulk hardness

Hardness tests have been performed on all the bulk samples obtained starting from the four powder feedstocks. The results of the tests are schematized in the Table 23.

Sample	Hardness (HV)			
	Low energy mechanical mixing	High energy mechanical mixing	Plasma deposition	Pre-alloying
A	135 ± 4	123 ± 4	118 ± 3	159 ± 6
B	140 ± 3	124 ± 3	118 ± 4	156 ± 2
C	136 ± 4	122 ± 5	118 ± 6	148 ± 7
D	147 ± 6	133 ± 3	125 ± 5	158 ± 5
E	135 ± 3	131 ± 3	123 ± 3	160 ± 6
F	133 ± 3	125 ± 3	127 ± 4	158 ± 6
G	140 ± 3	130 ± 4	126 ± 5	159 ± 3
H	134 ± 3	136 ± 4	126 ± 3	159 ± 4
I	134 ± 4	128 ± 4	128 ± 5	153 ± 4
Average	137 ± 4	128 ± 5	123 ± 4	157 ± 4

Table 23: bulk samples hardness measurements.

As seen in the case of sample porosity, also for what concern the hardness it is not possible to establish a solid relationship between printing parameters and hardness.

The presence of TiB₂ reinforcements plays a fundamental role in enhancing the mechanical properties of the composite material. In particular, all the average hardness values reported in Table 23 are higher if compared to the hardness of standard Al 2618 as-build samples (104.0 HV) obtained by Casati et. al [45].

Considering the mean values of each powder typology, it is clear that the pre-alloyed powder is the one that allows to achieve the highest hardness values, despite the lower concentration of TiB₂ phase. In this case the borides particles dimension is much

smaller compared to the other three powders. As a result, the strengthening effect given by those particles is more effective, leading to higher material hardness. In addition, the lowest grain dimension of the composite material was found in samples obtained from the pre-alloyed powder. This further increase the strength of the alloy and its hardness.

5 Conclusions

In this work, the possibility to obtain 2618-TiB₂ powder feedstocks with a high fraction of reinforcement produced by low energy mechanical mixing, high energy mechanical mixing, pre-alloying by gas atomization, and plasma assisted deposition was studied. Then, bulk samples were produced by LPBF process to investigate how the choice of the starting powder could affect the microstructure and the mechanical properties of the bulk materials.

The main results of the studies on powder feedstocks are reported in the following:

- 2618-TiB₂ powder feedstocks with a high fraction of reinforcement (6-7 wt%) were successfully produced by low energy mechanical mixing, high energy mechanical mixing and plasma assisted deposition. For the pre-alloyed powder batch, a maximum of ~3 wt% of TiB₂ was obtained.
- Considering the low energy mechanical mixed powder, it is possible to conclude that the three mixing strategies – 2, 4 and 8 hours – led to negligible differences between the resulting composite powder. Indeed, a homogeneous TiB₂ dispersion was achieved in all the three cases. For this reason, 2 hours of mixing can be considered sufficient.
- Dealing with the low energy mixing feedstock, the analyses performed before and after the sieving process pointed out that this powder batch needs to be re-mixed in order to be used for a subsequent LPBF process, since during the sieving a great part of TiB₂ reinforcements is removed from the Al powder surface. Different is the situation for the high energy mixing and the plasma deposition batches, where instead the reinforcements concentration was not affected by reduction. Lastly, the pre-alloyed powder was not affected by sieving since it does not present any external reinforcing particles.
- The addition of ex-situ ceramic particles can have a detrimental effect on flowability. However, all the investigated feedstocks were successfully printed by Renishaw AM 250 LPBF system. The pre-alloyed feedstock showed the best flowability, since the powder particles movement is not affected by external reinforcements. Instead, among the ex-situ reinforced feedstocks, the powder produced by high-energy mechanical mixing method is characterized by the best flowing behaviour.

The main results of the study on bulk samples are reported below:

- High level of density – >99% – was achieved with all the powder feedstocks. Although standard Al 2618 alloy shows a high hot cracking susceptibility, TiB₂ particles were able to avoid crack nucleation and propagation. Indeed, all the bulk samples obtained from the four MMC feedstocks showed a crack-free microstructure.
- A TiB₂ homogeneous dispersion has been observed in all the bulk samples analysed. The highest reinforcements concentration was found in low energy mixing bulk sample but, at the same time, borides average diameter was the highest. The lowest TiB₂ content was in the pre-alloyed sample, however, the detected size was the smallest.
- TiB₂ dispersion successfully refined the bulk material grains structure with respect to standard Al 2618 alloy. Sample produced with pre-alloyed powder showed the finest grain size distribution, while low energy mixing the coarsest. This means that the sub-micrometric reinforcements present in the gas-atomized powder were more effective in refining the microstructure than bigger borides preset in the other three feedstocks.
- Reinforcement particles present in MMC bulk samples were able to increase the hardness with respect to standard Al 2618 alloy. The highest bulk microhardness was achieved with pre-alloyed powder, though it contains the lowest amount of TiB₂. This occurred due to the small size of reinforcement particles and to the refined grain structure.

To conclude, the best overall performances are achieved with the pre-alloyed powder, but it does not satisfy the target in term of TiB₂ particles weight fraction. Among the ex-situ reinforced feedstocks, the powder produced with plasma deposition showed the worst flowability. The powder produced with low energy mechanical mixing led to the coarsest TiB₂ particles in printed samples and needs to be re-mixed after sieving. The feedstock showing the best compromise of properties is the powder produced with the high energy mechanical mixing method.

A possible solution to overcome the limitations in TiB₂ quantity of pre-alloying by gas atomization is to combine different powder functionalization methods. In this scenario, the surface of pre-alloyed powder can be decorated with ceramic particles with one of the ex-situ methods proposed in this work.

Bibliography

- [1] R. Casati and M. Vedani, "Metal Matrix Composites Reinforced by Nano-Particles—A Review," *Metals (Basel)*, vol. 4, no. 1, pp. 65–83, Mar. 2014, doi: 10.3390/met4010065.
- [2] T. W. Clyne and P. J. Withers, *An Introduction to Metal Matrix Composites*. Cambridge University Press, 1993. doi: 10.1017/CBO9780511623080.
- [3] S. P. Rawal, "Metal-matrix composites for space applications," *JOM*, vol. 53, no. 4, pp. 14–17, Apr. 2001, doi: 10.1007/s11837-001-0139-z.
- [4] L. Bhanuprakash, N. Manikandan, L. Varghese, and J. Joseph, "Study on aluminium metal matrix composites reinforced with SiC and granite powder," *Mater Today Proc*, Jul. 2023, doi: 10.1016/j.matpr.2023.06.246.
- [5] R. Casati, A. Fabrizi, G. Timelli, A. Tuissi, and M. Vedani, "Microstructural and Mechanical Properties of Al-Based Composites Reinforced with In-Situ and Ex-Situ Al₂O₃ Nanoparticles," *Adv Eng Mater*, vol. 18, no. 4, pp. 550–558, Apr. 2016, doi: 10.1002/adem.201500297.
- [6] R. Casati *et al.*, "Ex situ Al–Al₂O₃ ultrafine grained nanocomposites produced via powder metallurgy," *J Alloys Compd*, vol. 615, pp. S386–S388, Dec. 2014, doi: 10.1016/j.jallcom.2013.10.236.
- [7] M. Y. Khalid, R. Umer, and K. A. Khan, "Review of recent trends and developments in aluminium 7075 alloy and its metal matrix composites (MMCs) for aircraft applications," *Results in Engineering*, vol. 20, p. 101372, Dec. 2023, doi: 10.1016/j.rineng.2023.101372.
- [8] N. Bhadauria, P. Vashishtha, S. Mishra, and P. Bhardwaj, "Fabrication of aluminium MMCs & associated difficulties – A review," *Mater Today Proc*, vol. 64, pp. 1276–1282, 2022, doi: 10.1016/j.matpr.2022.04.102.
- [9] B. P. Sahoo, D. Das, and A. K. Chaubey, "Strengthening mechanisms and modelling of mechanical properties of submicron-TiB₂ particulate reinforced Al 7075 metal matrix composites," *Materials Science and Engineering: A*, vol. 825, p. 141873, Sep. 2021, doi: 10.1016/j.msea.2021.141873.
- [10] A. Sanaty-Zadeh, "Comparison between current models for the strength of particulate-reinforced metal matrix nanocomposites with emphasis on consideration of Hall–Petch effect," *Materials Science and Engineering: A*, vol. 531, pp. 112–118, Jan. 2012, doi: 10.1016/j.msea.2011.10.043.

- [11] Z. Zhang and D. L. Chen, "Contribution of Orowan strengthening effect in particulate-reinforced metal matrix nanocomposites," *Materials Science and Engineering: A*, vol. 483–484, pp. 148–152, Jun. 2008, doi: 10.1016/j.msea.2006.10.184.
- [12] Z. ZHANG and D. CHEN, "Consideration of Orowan strengthening effect in particulate-reinforced metal matrix nanocomposites: A model for predicting their yield strength," *Scr Mater*, vol. 54, no. 7, pp. 1321–1326, Apr. 2006, doi: 10.1016/j.scriptamat.2005.12.017.
- [13] S. Zhang, M. Ding, L. Wang, W. Ge, and W. Yan, "Laser powder bed fusion of diamond/N6 MMCs enabled by Ni-Ti coated diamond particles," *Mater Des*, vol. 217, p. 110635, May 2022, doi: 10.1016/J.MATDES.2022.110635.
- [14] R. Nandhakumar and K. Venkatesan, "A process parameters review on selective laser melting-based additive manufacturing of single and multi-material: Microstructure, physical properties, tribological, and surface roughness," *Mater Today Commun*, vol. 35, p. 105538, Jun. 2023, doi: 10.1016/j.mtcomm.2023.105538.
- [15] N. Limbasiya, A. Jain, H. Soni, V. Wankhede, G. Krolczyk, and P. Sahlot, "A comprehensive review on the effect of process parameters and post-process treatments on microstructure and mechanical properties of selective laser melting of AlSi10Mg," *Journal of Materials Research and Technology*, vol. 21, pp. 1141–1176, Nov. 2022, doi: 10.1016/J.JMRT.2022.09.092.
- [16] T. DebRoy *et al.*, "Additive manufacturing of metallic components – Process, structure and properties," *Prog Mater Sci*, vol. 92, pp. 112–224, Mar. 2018, doi: 10.1016/j.pmatsci.2017.10.001.
- [17] Y. Fang, M.-K. Kim, Y. Zhang, Z. Duan, Q. Yuan, and J. Suhr, "Particulate-reinforced iron-based metal matrix composites fabricated by selective laser melting: A systematic review," *J Manuf Process*, vol. 74, pp. 592–639, Feb. 2022, doi: 10.1016/j.jmapro.2021.12.018.
- [18] E. M. Sefene, "State-of-the-art of selective laser melting process: A comprehensive review," *J Manuf Syst*, vol. 63, pp. 250–274, Apr. 2022, doi: 10.1016/J.JMSY.2022.04.002.
- [19] Y. Huang *et al.*, "Keyhole fluctuation and pore formation mechanisms during laser powder bed fusion additive manufacturing," *Nat Commun*, vol. 13, no. 1, p. 1170, Mar. 2022, doi: 10.1038/s41467-022-28694-x.
- [20] H. Hyer *et al.*, "Understanding the Laser Powder Bed Fusion of AlSi10Mg Alloy," *Metallography, Microstructure, and Analysis*, vol. 9, no. 4, pp. 484–502, Aug. 2020, doi: 10.1007/s13632-020-00659-w.
- [21] M. Galetto, G. Genta, G. Maculotti, and E. Verna, "Defect Probability Estimation for Hardness-Optimised Parts by Selective Laser Melting," *International Journal*

- of Precision Engineering and Manufacturing*, vol. 21, no. 9, pp. 1739–1753, Sep. 2020, doi: 10.1007/s12541-020-00381-1.
- [22] F. Lv, L. Shen, H. Liang, D. Xie, C. Wang, and Z. Tian, “Mechanical properties of AlSi10Mg alloy fabricated by laser melting deposition and improvements via heat treatment,” *Optik (Stuttg)*, vol. 179, pp. 8–18, Feb. 2019, doi: 10.1016/j.ijleo.2018.10.112.
- [23] F. Belevi, R. Casati, M. Vedani, and J. Volpp, “Design and Characterization of Al–Mg–Si–Zr Alloys with Improved Laser Powder Bed Fusion Processability,” *Metallurgical and Materials Transactions A*, vol. 53, no. 1, pp. 331–343, Jan. 2022, doi: 10.1007/s11661-021-06531-y.
- [24] L. Liu, T. Minasyan, R. Ivanov, S. Aydinyan, and I. Hussainova, “Selective laser melting of TiB₂-Ti composite with high content of ceramic phase,” *Ceram Int*, vol. 46, no. 13, pp. 21128–21135, Sep. 2020, doi: 10.1016/j.ceramint.2020.05.189.
- [25] L. Liu, T. Minasyan, R. Ivanov, S. Aydinyan, and I. Hussainova, “Selective laser melting of TiB₂-Ti composite with high content of ceramic phase,” *Ceram Int*, vol. 46, no. 13, pp. 21128–21135, Sep. 2020, doi: 10.1016/j.ceramint.2020.05.189.
- [26] S. Yim, K. Aoyagi, K. Yanagihara, H. Bian, and A. Chiba, “Effect of mechanical ball milling on the electrical and powder bed properties of gas-atomized Ti–48Al–2Cr–2Nb and elucidation of the smoke mechanism in the powder bed fusion electron beam melting process,” *J Mater Sci Technol*, vol. 137, pp. 36–55, Feb. 2023, doi: 10.1016/j.jmst.2022.07.024.
- [27] C. F. Burmeister and A. Kwade, “Process engineering with planetary ball mills,” *Chem Soc Rev*, vol. 42, no. 18, p. 7660, 2013, doi: 10.1039/c3cs35455e.
- [28] R. Casati, J. Flocchi, A. Fabrizi, N. Lecis, F. Bonollo, and M. Vedani, “Effect of ball milling on the ageing response of Al2618 composites reinforced with SiC and oxide nanoparticles,” *J Alloys Compd*, vol. 693, pp. 909–920, Feb. 2017, doi: 10.1016/j.jallcom.2016.09.265.
- [29] J. H. Martin, B. D. Yahata, J. M. Hundley, J. A. Mayer, T. A. Schaedler, and T. M. Pollock, “3D printing of high-strength aluminium alloys,” *Nature*, vol. 549, no. 7672, pp. 365–369, Sep. 2017, doi: 10.1038/nature23894.
- [30] H. Torbati-Sarraf, S. A. Torbati-Sarraf, N. Chawla, and A. Poursaeed, “A comparative study of corrosion behavior of an additively manufactured Al-6061 RAM2 with extruded Al-6061 T6,” *Corros Sci*, vol. 174, p. 108838, Sep. 2020, doi: 10.1016/j.corsci.2020.108838.
- [31] T. Horn *et al.*, “Laser powder bed fusion additive manufacturing of oxide dispersion strengthened steel using gas atomized reaction synthesis powder,” *Mater Des*, vol. 216, p. 110574, Apr. 2022, doi: 10.1016/j.matdes.2022.110574.

- [32] Y. Cao, H. L. Wei, T. Yang, T. T. Liu, and W. H. Liao, "Printability assessment with porosity and solidification cracking susceptibilities for a high strength aluminum alloy during laser powder bed fusion," *Addit Manuf*, vol. 46, p. 102103, Oct. 2021, doi: 10.1016/J.ADDMA.2021.102103.
- [33] W. Stopyra, K. Gruber, I. Smolina, T. Kurzynowski, and B. Kuźnicka, "Laser powder bed fusion of AA7075 alloy: Influence of process parameters on porosity and hot cracking," *Addit Manuf*, vol. 35, p. 101270, Oct. 2020, doi: 10.1016/J.ADDMA.2020.101270.
- [34] C. M. Bailey, J. A. Morrow, E. M. Stallbaumer-Cyr, C. Weeks, M. M. Derby, and S. M. Thompson, "Effects of Build Angle on Additively Manufactured Aluminum Alloy Surface Roughness and Wettability," *J Manuf Sci Eng*, vol. 144, no. 8, Aug. 2022, doi: 10.1115/1.4053608.
- [35] G. Li *et al.*, "Investigation into the effect of energy density on densification, surface roughness and loss of alloying elements of 7075 aluminium alloy processed by laser powder bed fusion," *Opt Laser Technol*, vol. 147, p. 107621, Mar. 2022, doi: 10.1016/J.OPTLASTEC.2021.107621.
- [36] C. Galleguillos, A. Periñán, J. Santaolaya, S. González, and F. Lasagni, "Computed Tomography and Digital Radiography for Additive Manufacturing process Quality Assurance and parameters definition," 2019. [Online]. Available: <http://www.ndt.net/?id=25066>
- [37] S. E. Brika, M. Letenneur, C. A. Dion, and V. Brailovski, "Influence of particle morphology and size distribution on the powder flowability and laser powder bed fusion manufacturability of Ti-6Al-4V alloy," *Addit Manuf*, vol. 31, p. 100929, Jan. 2020, doi: 10.1016/J.ADDMA.2019.100929.
- [38] R. Freeman, "Measuring the flow properties of consolidated, conditioned and aerated powders — A comparative study using a powder rheometer and a rotational shear cell," *Powder Technol*, vol. 174, no. 1–2, pp. 25–33, May 2007, doi: 10.1016/J.POWTEC.2006.10.016.
- [39] M. Leturia, M. Benali, S. Lagarde, I. Ronga, and K. Saleh, "Characterization of flow properties of cohesive powders: A comparative study of traditional and new testing methods," *Powder Technol*, vol. 253, pp. 406–423, Feb. 2014, doi: 10.1016/J.POWTEC.2013.11.045.
- [40] E. Kmiecik, B. Tomaszewska, K. Wątor, and M. Bodzek, "Selected problems with boron determination in water treatment processes. Part I: comparison of the reference methods for ICP-MS and ICP-OES determinations," *Environmental Science and Pollution Research*, vol. 23, no. 12, pp. 11658–11667, Jun. 2016, doi: 10.1007/s11356-016-6328-7.
- [41] J. Wang, R. Zhu, Y. Liu, and L. Zhang, "Understanding melt pool characteristics in laser powder bed fusion: An overview of single- and multi-track melt pools

- for process optimization," *Advanced Powder Materials*, vol. 2, no. 4, p. 100137, Oct. 2023, doi: 10.1016/j.apmate.2023.100137.
- [42] D. Koutny *et al.*, "Influence of Scanning Strategies on Processing of Aluminum Alloy EN AW 2618 Using Selective Laser Melting," *Materials*, vol. 11, no. 2, p. 298, Feb. 2018, doi: 10.3390/ma11020298.
- [43] F. Belevi, R. Casati, F. Larini, M. Riccio, and M. Vedani, "Investigation on two Ti-B-reinforced Al alloys for Laser Powder Bed Fusion," *Materials Science and Engineering: A*, vol. 808, p. 140944, Mar. 2021, doi: 10.1016/j.msea.2021.140944.
- [44] Z. Chen and K. Yan, "Grain refinement of commercially pure aluminum with addition of Ti and Zr elements based on crystallography orientation," *Sci Rep*, vol. 10, no. 1, p. 16591, Oct. 2020, doi: 10.1038/s41598-020-73799-2.
- [45] R. Casati, J. N. Lemke, A. Z. Alarcon, and M. Vedani, "Aging Behavior of High-Strength Al Alloy 2618 Produced by Selective Laser Melting," *Metallurgical and Materials Transactions A*, vol. 48, no. 2, pp. 575–579, Feb. 2017, doi: 10.1007/s11661-016-3883-y.

List of Figures

Figure 1: Orowan loop formation around TiB ₂ particles [9].....	4
Figure 2: Effect of strengthening contributions and total resulting strengthening increment for a 2 wt.% Al ₂ O ₃ reinforced Al matrix composite, calculated using the modified Clyne model [1].	8
Figure 3: Strengthening mechanism contributions as a function of volume fraction for the particle sizes 30 nm and 1 μm [10].	9
Figure 4: the schematic diagram of the LPBF process [17].....	11
Figure 5: graphical representation of LPBF parameters [18].	12
Figure 6: Common scanning strategies [18].	13
Figure 7: Relative density at varying laser power, hatch space and layer thickness [20].	14
Figure 8: AlSi ₁₀ Mg LPBF produced samples hardness at varying laser power, scan speed and hatch space [21].....	15
Figure 9: Effect of varying speed on UTS and Elongation of AlSi ₁₀ Mg [22].....	18
Figure 10: a schematic representation of the five routes to produce powder for MMC by LPBF.....	19
Figure 11: Representation of the gas atomization process.	21
Figure 12: Renishaw AM250 printer (a) and RBV system (b).	29
Figure 13: Illustration of the difference between hatch distance and point distance [36].	29
Figure 14: Representative image of cubic samples.	30
Figure 15: a) an 8-bit colour image taken from the optical microscope; b) the same image after the threshold is set; c) final analysis: the material in the example image has an overall porosity equal to 0.71% and an average pore size of 81.285μm.	31
Figure 16: FT4 powder rheometer (a) and blade allowed movements (b).....	32
Figure 17: low energy mechanical mixed powder batch SEM analysis.	34
Figure 18: Particle size distribution of low energy mixed feedstock.....	36
Figure 19: SEM images of low energy mechanical mixed powder mixed for 2, 4 and 8 hours.....	37
Figure 20: SEM image of high energy mechanical mixed powder batch.....	38
Figure 21: Particle size distribution of high energy mixed feedstock.....	40

Figure 22: SEM image of plasma deposition powder.	40
Figure 23: Particle size distribution of plasma deposition feedstock.	42
Figure 24: SEM image of pre-alloyed powder.	42
Figure 25: Particle size distribution of gas atomized feedstock.....	43
Figure 26: SEM image of a section of a pre-alloyed powder particle.	44
Figure 27: procedure of the graphical extrapolation used to evaluate TiB ₂ dimensions.	47
Figure 28: SEM images of the 2618+TiB ₂ low energy mechanical mixing powder feedstock before (a, b) and after (c, d) sieving.....	49
Figure 29: XRD pattern of 8h mixed powder before (a) and after sieving (b).	50
Figure 30: SEM images of the plasma deposition powder feedstock before (a, b) and after (c, d) the sieving process.	52
Figure 31: SEM images of the high energy mixing powder feedstock before (a, b) and after (c, d) the sieving process.	54
Figure 32: flowability indexes, respectively BFE (a), SE (b), CBD (c).	56
Figure 33: low energy mechanical mixing bulk samples.....	58
Figure 34: high energy mechanical mixing bulk samples.	58
Figure 35: plasma deposition bulk samples.	59
Figure 36: pre-alloying bulk samples.	59
Figure 37: SEM photos of low energy mechanical mixing bulk sample (sample B)...	61
Figure 38: SEM photos of high energy mechanical mixing bulk sample (sample B)..	62
Figure 39: SEM photos of plasma deposition bulk sample (sample B).	64
Figure 40: SEM photos of pre-alloyed bulk sample (sample B).....	65
Figure 41: IPF map (a) and phase map (b) of low energy mixing sample (sample B). 67	
Figure 42: IPF map (a) and phase map (b) of high energy mixing sample (sample B).	68
Figure 43: IPF map (a) and phase map (b) of plasma deposition sample (sample B). 69	
Figure 44: IPF map (a) and phase map (b) of pre-alloying sample (sample B).	71

List of Tables

Table 1: Aluminium 2618 alloy composition.....	26
Table 2: feedstocks chemical compositions and acceptance limit.	27
Table 3: fixed printing parameters.....	29
Table 4: varying printing parameters.....	30
Table 5: EDS analysis composition of selected areas – low energy mechanical mixing powder.	35
Table 6: Acceptance limit composition and experimental ICP-OES composition of the four feedstocks.....	37
Table 7: EDS analysis composition of selected spots – high energy mechanical mixing powder.....	39
Table 8: EDS analysis composition of selected area and spot – plasma deposition powder.....	41
Table 9: EDS analysis composition of selected area and spot – pre-alloyed powder..	43
Table 10: EDS analysis of selected area and spot – section of the pre-alloyed powder.	45
Table 11: Aluminium powder and reinforcements comparison.	46
Table 12: Concentrations of TiB ₂ obtained from XRD patterns and by image analysis of the SEM picture.	51
Table 13: Concentrations of TiB ₂ obtained by image analyses of SEM pictures of plasma deposition and high energy mixing batches.	54
Table 14: Bulk samples porosity analysis.	57
Table 15: percentage and dimension of reinforcement in bulk sample.....	61
Table 16: percentage and dimension of reinforcement in bulk sample.....	63
Table 17: percentage and dimension of reinforcement in bulk sample.....	64
Table 18: percentage and dimension of reinforcement in bulk sample.....	66
Table 19: Average grain area and diameter in bulk sample.	67
Table 20: Average grain area and diameter in bulk sample.	68
Table 21: Average grain area and diameter in bulk sample.	70
Table 22: Average grain area and diameter in bulk sample.	71
Table 23: bulk samples hardness measurements.....	72

